Title
Predictive Model of the Degradation of Cable Insulation Subject to Heat and Radiation

Author
Chang, Yuan-Shang

Publication Date
2017

Peer reviewed|Thesis/dissertation

UNIVERSITY OF CALIFORNIA
Los Angeles

Predictive Model of the Degradation of Cable Insulation Subject to Heat and Radiation

A dissertation submitted in partial satisfaction of the
requirements for the degree Doctor of Philosophy
in Materials Science and Engineering

by

Yuan-Shang Chang

2017

ABSTRACT OF THE DISSERTATION

Predictive Model of the Degradation of Cable Insulation
Subject to Heat and Radiation

by

Yuan-Shang Chang
Doctor of Philosophy in Materials Science and Engineering
University of California, Los Angeles, 2017
Professor Ali Mosleh, Chair

Degradation of cable insulation subject to heat and radiation is modeled by physics-based chemical, mechanical, and electrical approaches. Experimental data of cross-linked polyethylene (XLPE), ethylene propylene rubber (EPR), and silicone rubber (SIR) are incorporated to validate the models.

Chemical approaches divide aging kinetics into reaction- and diffusion-controlled mechanisms rendering homogeneous and heterogeneous cross-sections, respectively. The degradation profile of a cross-section serves as the base of Dichotomy Model. The model dichotomizes one bulk material into virtually degraded and non-degraded parts. The quotient of the two parts is determined by a diffusion theory in diffusion-controlled cases or by an exponential distribution in reaction-controlled scenarios to predict the lifespan of the cable

insulation. Besides the degradation of the insulation, the migration and decomposition of the antioxidant in the insulation are also modeled by a reaction-diffusion theory representing the uphill diffusion of the antioxidant. The uphill diffusion is driven by the unevenly-distributed activity coefficient linearly proportional to oxygen concentration with a negative slope.

Both mechanical and electrical approaches are derived from Dichotomy Model. The degradation of mechanical performance is focused on elongation at break (EAB) while that of electrical property is quantified by resistance. EAB and resistance as functions of time are deterministically developed. Incubation time is a parameter of the function representing the time period when the changes of the physical properties are negligible. Drop-off rate is the other parameter describing the trends of the properties. The values of the two parameters follow the trends of temperature and dose rates, which makes the functions predictable in different aging conditions. Unlike the state of the art, this model can accommodate the shape change of the curves of EAB and resistance along a time axis.

By Bayesian parameter estimation, the deterministic function has been converted into a probabilistic equation. This method can represent the thresholds of the EAB and resistance in field application with uncertainty denoting the reliability of cable insulation by expected lifespan in the form of probability. The approach is the first in the area.

The dissertation of Yuan-Shang Chang is approved.

Henry J. Burton

Jenn-Ming Yang

Qibing Pei

Ali Mosleh, Committee Chair

University of California, Los Angeles

2017

Dedication

To my parents, wife, and daughter

Table of Contents

List of Tables

List of Figures

Abbreviations

A	Area
ANSI	American National Standards Institute
CDF	Cumulative Distribution Function
D	Diffusivity
DED	Superposition of Dose to Equivalent Damage Data
EAB	Elongation at Break
EPR	Ethylene Propylene Rubber
EPRI	Electric Power Research Institute
FR	Flame Retardant
FTIR	Fourier Transform Infrared Spectroscopy
Gy	Gray
h	Hour
HDPE	High Density Polyethylene
I	Current
IAEA	International Atomic Energy Agency
IEEE	Institute of Electrical and Electronics Engineers
k	Boltzmann constant
l	Length
L	Thickness
LDPE	Low Density Polyethylene
N_0	Avogadro constant
NPP	Nuclear Power Plant
OI	Oxidation Index
PDF	Probability Distribution Function
R	Ideal Gas Constant
R	Resistance
SIR	Silicone Rubber
T	Temperature
t	time
TDD	Superposition of Time Dependent Data
UHMWPE	Ultra High Molecular Weight Polyethylene
V_d	Virtual degradation ratio
XLPE	Cross-Linked Polyethylene
α	Elongation factor
β	Empirical factor of EAB

δ	Normalized EAB
ΔG	Activation energy
θ	Parameter(s) of a model
μ	Average
ν	Drop-off rate
ν	Reaction rate
ρ	Density
ρ	Resistivity
σ	Standard deviation
τ_0	Incubation time

Acknowledgements

I would like to express my gratitude to many people helping me in accomplishing this dissertation.

To my parents, Chang, Lin, Liu, and Chou; thank you for your support. Your love is the most important thing leading me in my life. When I am lost, what you told me always helps me overcome difficulties and adversities. To my wife, Liu; you take care of my life, the family, and our lovely daughter.

To my advisor, Professor Ali Mosleh; you are my mentor giving me invaluable knowledge, experience, and encouragement. With these positive influences, I can conduct the research and conclude this dissertation. To Professor Jenn-Ming Yang; you are my mentor having been constantly assisting me since the first day I entered UCLA. To my committee members, Professor Henry Burton and Qibing Pei; your advice is invaluable. Your thoughts fortify the content, structure, and logic of this dissertation.

This research is a part of the project entitled Physics-Based Probabilistic Model of the Effects of Ionizing Radiation on Polymeric Insulators of Electric Cables used in Nuclear Power Plants, supported by the U. S. Department of Energy's Consolidated Innovative Nuclear Research program.

Vita

2014 - 2017	Research Assistant Department of Materials Science and Engineering University of California, Los Angeles Los Angeles, California, USA

Chapter 1: Introduction

1.1 Motivation

How long can a nuclear reactor last? This is the title of an article published by Scientific American on November 20th, 2009; the subheading is even more intriguing: industry experts argue old reactors could last another 50 years, or more [1, 2]. In the viewpoint of materials science and engineering, during 100 years, objects change as time elapses. The composition and distribution of the elements in any material are dynamic. How to maintain or replace the aging components in nuclear power plants (NPPs) to maintain their performance and, most important of all, the safety of these facilities for such a long time will be challenging. The makeup of the components in an NPP can be conventionally categorized into four basic groups: metals, ceramics, polymers, and composites [3]; the fourth can be considered as the combination of the former three. Among these, materials containing polymers may be most susceptible to degradation due to external energies such as heat and radiation, which are ubiquitous in NPPs. Cables are essential parts in any power plants; they transmit power and signals. The insulation layers of cables are often made from polymers whose degradation can be affected by the synergistic effects caused by heat and radiation. Besides nuclear reaction, radiation can also come from the sun. Therefore, approaches or standards that can define and estimate the life of cable insulations subject to heat and radiation are significant for power

plants operation and safety concern. However, predictive models addressing the degradation of cable insulation have not been fully developed.

1.2 Background

The oldest commercial NPP in the United States started operation in 1969 [1]. The total electricity generated in 1971 was 1.6E9 MWh and at that time nuclear provided only about 2.36% of total generated electricity. From 1971 to 2005, the total electricity had steadily increased 250% to 4.1E9 MWh, and maintained at this level to 2015. The nuclear power share had been increased about 850% to the ratio of 20% by 1992, and kept at that level until 2015 [4]. Both trends are shown in Figure 1.1. Besides the United States, many other countries depend on nuclear energy; Figure 1.2 illustrates the nations whose atomic shares of electricity in 2015 were higher than 18%. These statistics indicate that electricity generated from nuclear fuel continues playing a significant role worldwide.

Cables are necessary components in a power plant. Figure 1.3 schematically illustrates the structures of three common types of cables. Conductors are for transmitting power and signals. Besides providing grounding, shields can also prevent the interference from the electromagnetic waves induced by currents, for example. Both conductors and shields are made of metals. On the other hand, insulation and jackets are made from polymers which can

be prone to the degradation resulting from the heat and radiation.

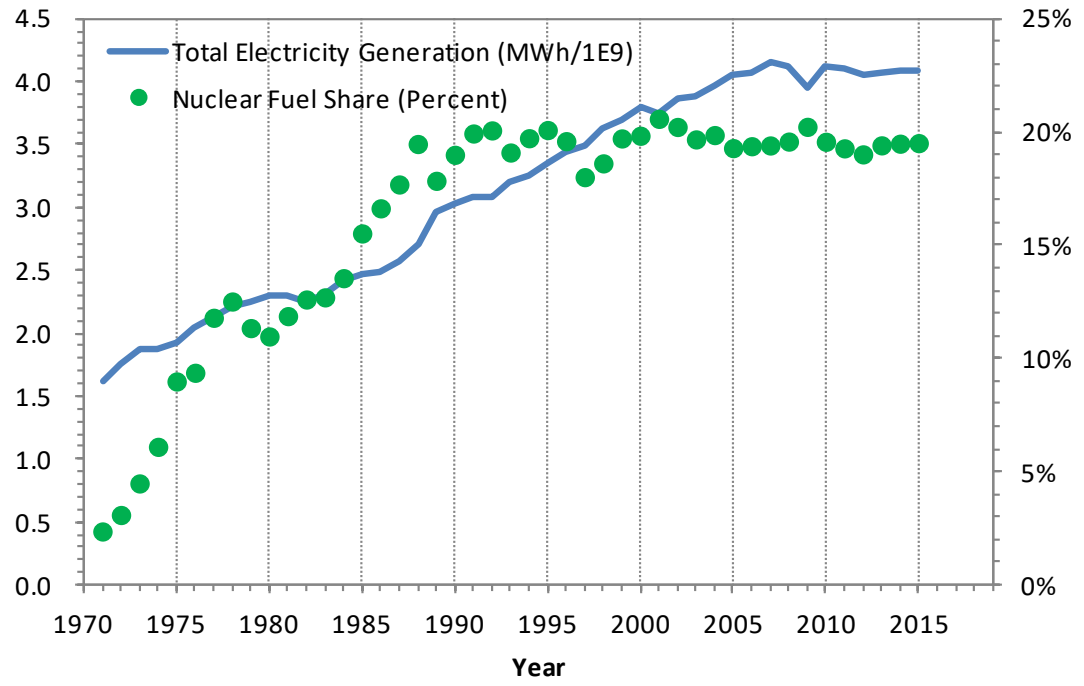

Figure 1.1 Relation between total and nuclear power share of generated electricity [4]

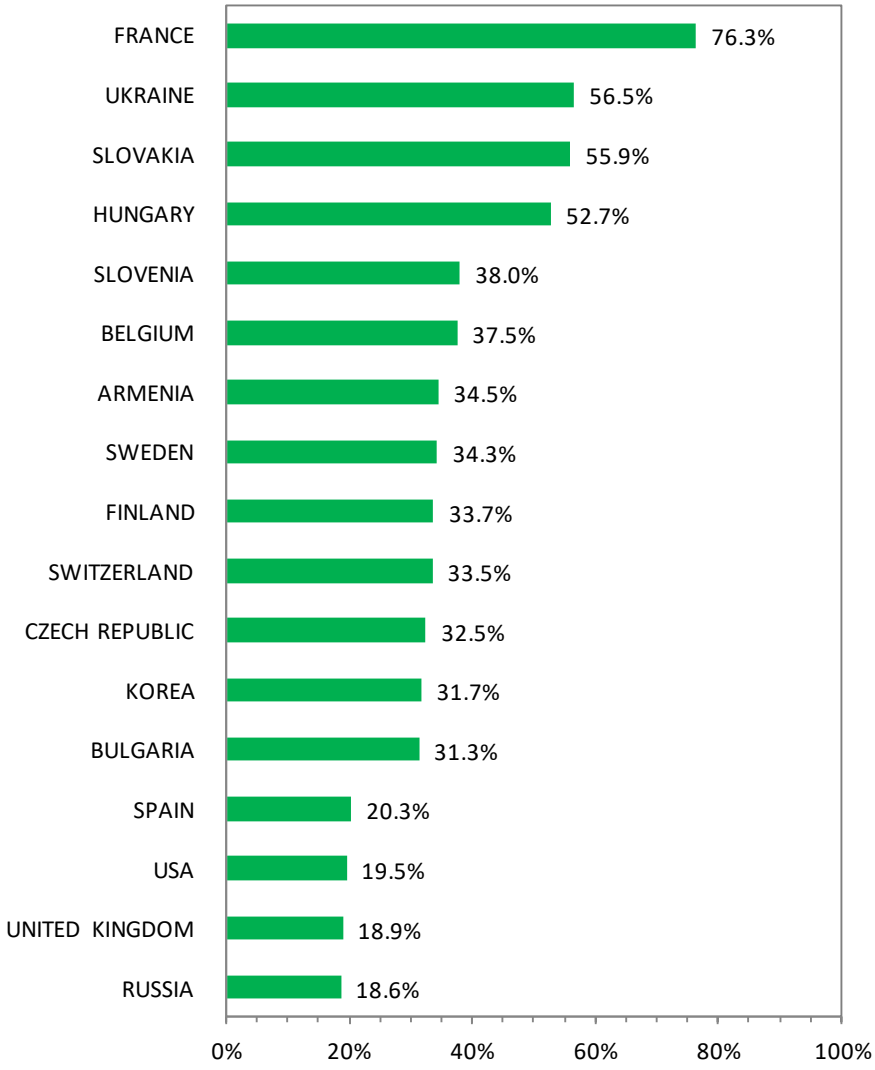

Figure 1.2 Nuclear share of electricity in various countries [5]

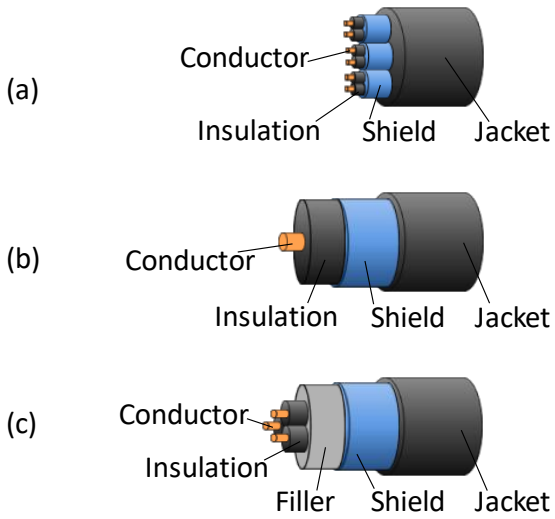

Figure 1.3 Schematic structures of three common types of cables: (a) a twisted pair shielded instrumentation cable. (b) a co-axial instrumentation cable. (c) a multi-conductor shielded control cable. [6]

This research is mainly concerned with the degradation of cable insulation. Table 1.1 lists three major materials which are used to manufacture the insulation layers: XLPE, EPR, and SIR. The percentages of the NPP units which have the insulation layers of the given materials are shown in Figure 1.4.

After identifying the types and percentages of the materials mainly used to make cable insulation Table 1.2 lists the locations at which the degradation of the insulation layers should be most likely of concern due to temperature and radiation. According to the table, the temperature range is approximately from room temperature to the boiling point of water; the range of the dose rates is about from 0.01 to 0.7 Gy/hour.

Table 1.1 Primary insulation materials [7]

Material*	Material Type	Insulation Use	Jacket Use
XLPE	Plastic	Common	Limited
EPR	Rubber	Common	Not suitable
SIR	Rubber	Common	Not suitable

*****XLPE: cross-linked polyethylene. EPR: ethylene propylene rubber. SIR: silicone rubber

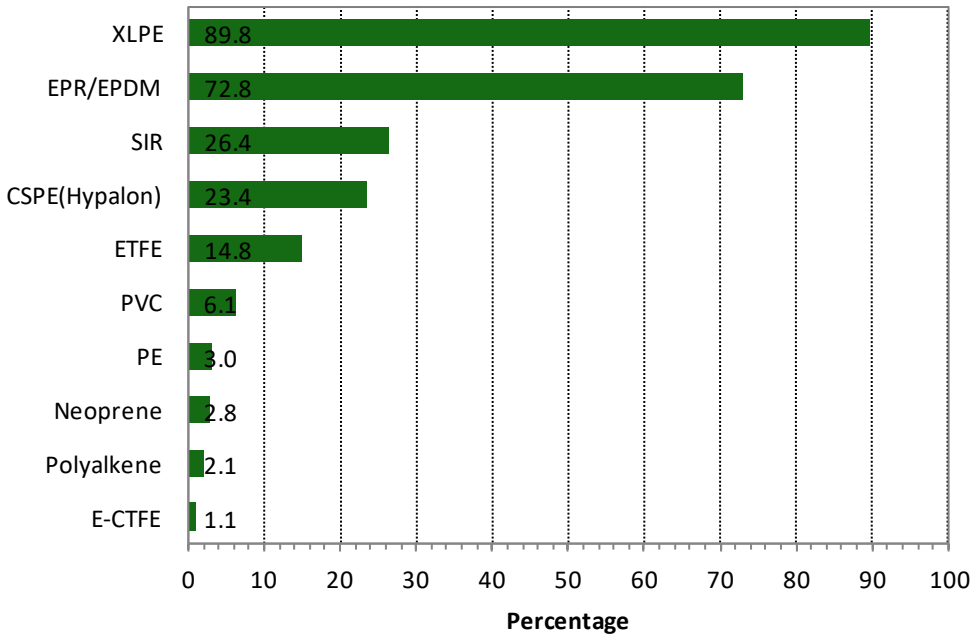

Figure 1.4 Percentage of NPPs with the types of the insulation of in-containment cables [8]

Table 1.2 Typical hot spot areas in NPPs [6]

Reactor Type	Hot Spot Location	Temperature (℃)	Radiation Dose Rate (Gy/hour)
PWR	Stream generator box	47-48, max 100	0.1
	Primary loop	50	0.7
BWR	Drywell neck region	100±5	0.5
	Primary steam relief valve region	70±5	0.01
	Power range monitor region	80±5	0.24
CANDU	Feeder cabinet and reactor vault	41-60	0.6-2.1
	Boiler areas	30-60	0.008-0.2

Table 1.3 Rating temperature of XLPE [9-12], EPR [13-16], and SIR [17-19]

Insulation Material	**Rating temperature(℃)**
XLPE	90
EPR	105
SIR	250

Since the molecular structures and compositions of XLPE, EPR, and SIR are different, their field application temperatures at the normal situation, also termed rating temperatures, are different. Each value is listed in Table 1.3. XLPE and EPR are sometimes rated at the same temperature: about 90℃, while SIR is more suitable for the applications at a higher temperature.

Corresponding to voltage levels, the cables in an NPP can be roughly categorized into

three classes: low voltage cables, medium voltage cables, and coaxial cables. Over 90% of them are low voltage cables [20]. The Institute of Electrical and Electronics Engineers (IEEE) [21] and Electric Power Research Institute (EPRI) [22] define the voltages below 1000V as low voltage. American National Standards Institute (ANSI) classifies system voltages at 600V or below to be “low voltage [23].” The detailed classifications of system voltages are listed in Table 1.4. The materials for the insulation layers suitable for the application of each voltage categories are listed in Table 1.5.

Table 1.4 System voltage classification [23]

Classification	**Lower Limit (V)**	**Higher Limit (V)**
Low voltage	-	600
Medium voltage	600	69k
High voltage	69k	230k
Extra high voltage	230k	1,100k
Ultra high voltage	1,100k	-

Table 1.5 Insulation materials corresponding to voltage levels used in NPPs [24]

Classifications of Cables	**Insulation Material**
High voltage cable	XLPE
Low voltage cable	XLPE EPR SIR

1.3 Significance

The total length of the cables installed in an NPP can be over 2,000 kilometers [20]. These cables are subject to heat and radiation, which makes the necessity of the replacement of the cables become an issue due to the degradation of the insulation layers. After all, the cost of the replacement is at least 10 times higher than that of installation [25].

In application, an insulation layer must have at least two characteristics: high resistivity to isolate electricity and adequate ductility to absorb mechanical forces. However, research indicates resistivity decreases due to degradation; one research even reported that XLPE insulation can lose resistivity several thousand times when it is aging [26]. On the other hand, as for the ductility, the EAB measured by a tensile test can decrease from more than 500% to less than 20% when an XLPE specimen is exposed to heat or radiation [20]. Hence, International Atomic Energy Agency (IAEA) suggested in a technical report that EAB at 0.5 may be defined as the end of the life of cable insulation in the view of ductility [27].

Either the diminishing of the resistivity or the reducing of the ductility can result in short circuit and cause tremendous financial loss to a power plant, not to mention the possibility of jeopardizing the integrity of a generator and threatening the safety of nearby residents, whose values are inestimable. Therefore, the replacement of aging cables should be assessed due to

the high cost of the work [25]. Plans and cautions must be comprehensively taken in advance.

To sum up, a model that can be used to precisely predict the condition of the “health” of an on-site insulation layer shall be helpful to power plants in scheduling a regular check at a proper frequency. In addition, if this model is developed, it can also be served as a guideline for the future design of a new power plant.

1.4 Objective

The objective of this dissertation is to develop deterministic and probabilistic models to quantify the degradation of cable insulation subject to heat and radiation (γ-ray emitted from ^{60}Co). The definitions of the degradation are based on chemical, mechanical, and electrical properties which are the oxide and antioxidant distribution, elongation at break, and electrical resistance, respectively. The materials of the cable insulation are XLPE, EPR, and SIR.

Chapter 2: An Assessment of the State of the Art

2.1 Overview of the Materials

Three most widely-used materials for cable insulation are XLPE, EPR, and SIR [8]. The main properties of these materials are discussed in this section. Additionally, the antioxidants that are commercially added in XLPE are also discussed. The antioxidants can prevent XLPE matrix from degradation which is mainly caused by the oxidation reaction induced by oxygen and moisture [28, 29].

2.1.1 XLPE

The molecular structure of polyethylene is illustrated in Figure 2.1. The chains of polyethylene before cross-linking are schematically represented in Figure 2.2. After the chains of the polyethylene are cross-linked, each chain becomes a part of the three-dimensional networks as shown in Figure 2.3. The molecular structure forming the network is shown in Figure 2.4 where the straight lines between two main chains indicate the bonds of the cross-link. The degree of cross-linking is usually between 65% and 89% according to ASTM F876 - 15a [30].

For Low-Density Polyethylene (LDPE), the n value in Figure 2.1 ranges from 1,000 to 10,000; the n value of High-Density Polyethylene (HDPE) ranges from 10,000 to 100,000.

For Ultra High Molecular Weight Polyethylene (UHMWPE), the n value is larger than 100,000. Most of the XLPE applied to wires and cable application is based on LDPE, which is focused in this dissertation.

For the XLPE applied to cable insulation, the normal application temperature, emergency temperature, and short circuit temperature provided by one cable manufacturer are 90℃, 130℃, and 250℃, respectively [31]. In the entire lifespan of XLPE insulation, 1,500 hours is the limit when this insulation is cumulatively working at this emergency temperature [32].

Mechanical properties are often used to quantify the degree of the aging of a material. EAB, or ductility, is considered for cable insulation. The EAB of a fresh XLPE insulation can range from 300% to 500%, while that of a degraded one can be lower than 20% [20].

Besides the mechanical property, the electrical insulating ability is also an important factor in the estimation an aging progress. Studies revealed that the resistivity of a new XLPE insulating layer is about 7×10^{14} Ω-cm. After aging at 150℃ for 500 hours, the resistivity can drop 1,000 times to 3×10^{11} Ω-cm [26].

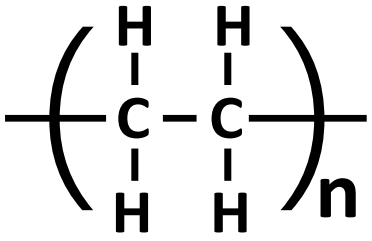

Figure 2.1 The repeat structure of the chain of polyethylene

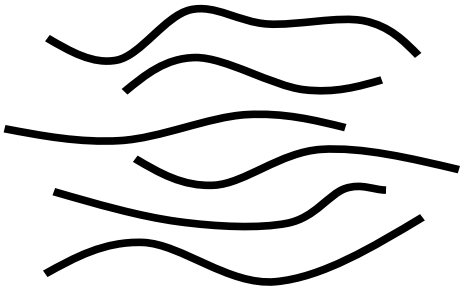

Figure 2.2 Schematic illustration of the main chains of polyethylene before cross-linking

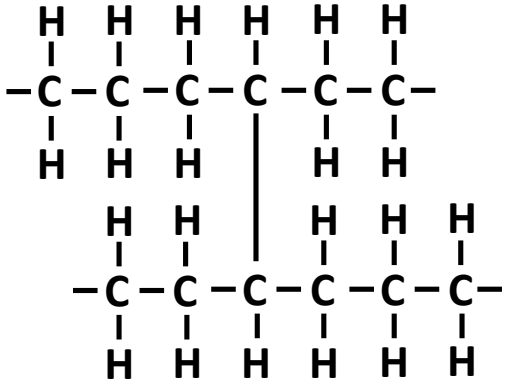

Figure 2.3 Schematic illustration of the cross-link of polyethylene

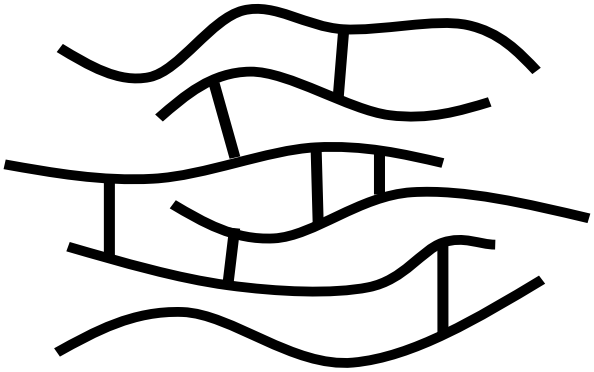

Figure 2.4 Schematic illustration of the chains of polyethylene after cross-linking

2.1.2 Antioxidant in XLPE

The additives are always doped into an XLPE insulation layer to prevent the XLPE matrix from degradation. These additives are termed antioxidants. Antioxidant may compete with the reactions caused by the formation of the free radicals generated by heat and radiation. Therefore, antioxidants can hinder the subsequent reactions initiated by the free radicals by reacting with the free radical first. This mechanism makes antioxidants work like a patch, stopping the bleeding from a wound as an analogy of a free radical site. However, this antioxidant cannot deter the decrease of the molecular weight of matrix polymers.

Another mechanism rendered by different types of antioxidants can slow down polymer degradation as well. An antioxidant is considered to being able to delocalize thermal energy, which can lower the formation probability of free radicals in a matrix. Unlike the first

mechanism mentioned in the previous paragraph, this antioxidant can alter degradation reaction beforehand. As a result, it can prevent the decrease of the molecular weight of a polymer matrix [33]. One of the second types of the antioxidants is discussed in this dissertation. Its molecular structure is shown in Figure 2.5, which is a commercially adopted antioxidant named Nocrac 300 [28, 33].

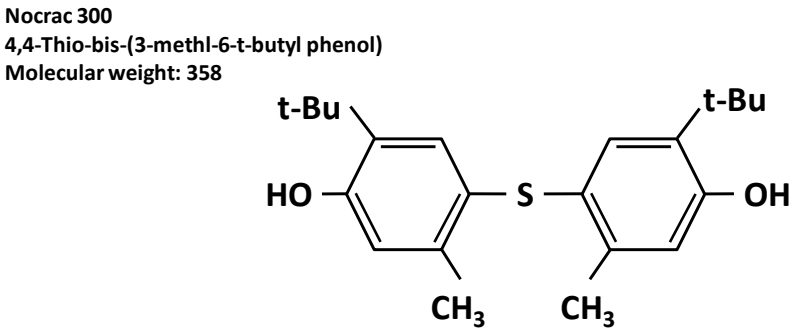

Figure 2.5 The molecular structure of an antioxidant named Nocrac 300

Antioxidants can diffuse out of a polymer matrix after they were doped in polymers, and can also decompose due to external energy such as heat. The loss of antioxidants can result in the acceleration of degradation. However, less quantitative models are developed in the state of the art to calculate the diffusion and decomposition behavior of antioxidants. Nevertheless, one paper used Fourier-transform infrared spectroscopy (FTIR) to perform thorough characterization on the concentration of the antioxidant distributing from the surface to the

core on the cross-section of a bulk XLPE [34]. In the paper [34], the measured concentration of the antioxidant during the thermal ageing is lower at the center and higher at the surface although the antioxidant diffuses outward. In other words, the antioxidant diffuses from low to high concentration. No explanation has been given by the authors [34]. This dissertation has developed a physics-based model to justify this unexplained diffusion phenomenon.

2.1.3 EPR

The molecular structure of EPR is illustrated in Figure 2.6. In field application, the weight percentage of ethylene ranges from 45% to 80%. The molecular weight of EPR is usually between 80,000 and 250,000.

There are two units repeating along one main chain of EPR. Each of the two colors in Figure 2.7 indicates one of the repeating units in Figure 2.6. Different sequencing arrangements made by the two repeating units along one polymer chain are possible; they can be random, alternating, or block copolymers, which are illustrated in Figure 2.7. For the EPR applied to cable insulation, the arrangement forms a random copolymer.

For the EPR applied to cable insulation, the normal application temperature, emergency temperature, and short circuit temperature provided by one cable manufacturer are 105℃, 140℃, and 250℃, respectively [14-16]. No maximum time is suggested by the manufacturer

when it is constantly exposed to the emergency temperature. This dissertation developed a method to obtain this maximum threshold by a physics-based model.

A fresh EPR possesses certain mechanical properties such as lower Young's modulus and high ductility compared to inorganic materials. When an external force elongates an EPR specimen, input energy can align the polymer chains, which decrease the entropy. As the external force is removed, entropy spontaneously increase, which makes the specimen retract. At the same time, the Gibbs free energy of the polymer decreases and heat is released from the specimen. The process discussed above renders the high EAB of EPR in a tensile test.

Among various mechanical properties, for example, EAB is a good indicator that can quantify the degree of the aging of EPR. The EAB of a fresh EPR insulation can range from 400% to 500%, while a degraded one can be lower than 10% [20]. This big difference suggests that the molecular structure before and after aging should be significantly varied.

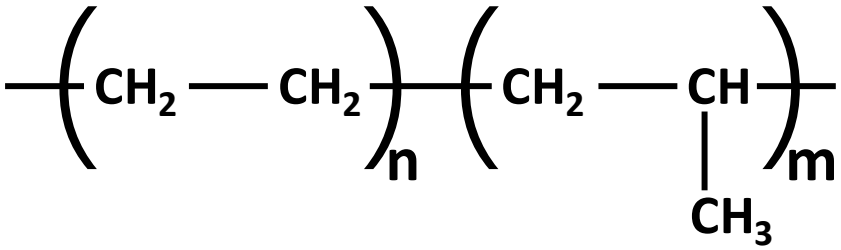

Figure 2.6 The repeat structure of ethylene-propylene rubber

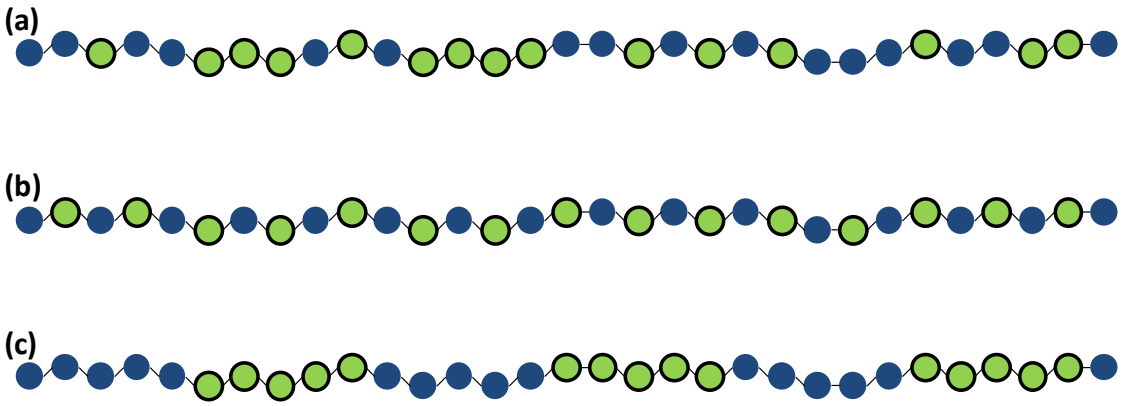

Figure 2.7 Schematic representation of (a) random, (b) alternating, and (c) block copolymers

2.1.4 SIR

The molecular structure of SIR is illustrated in Figure 2.8; the value of the n in the figure can range from 5,000 to 10,000, which means the molecular weight is usually between 370,000 and 740,000 [35, 36]. SIR is often applied to gasket, seals, cable insulation, and hot gas and liquid conduits [37]. Generally, for the field application of cable insulation, the

molecular weight of SIR is greater than 500,000 [38].

Among XLPE, EPR, and SIR insulation, the cables made from SIR can stand the highest temperature; this is the result of the Si-O bonds in the polymer chain. Unlike the C-C bond in polyethylene or polypropylene whose bonding energy is about 355 kJ/mol, the bonding energy of Si-O is about 443 kJ/mol [39-41]. Therefore, SIR cables are suitable for the application at a higher temperature, which can be close to 250℃ [17-19].

EAB can also be used to quantify the degree of the degradation of SIR insulation. Due to the nature of the Si-O bond providing high flexibility when the polymer chain is twisted or elongated [42], the EAB of a fresh SIR sample can reach 550%, while the EAB of the samples subject to heat or radiation can be lower than 10% [20].

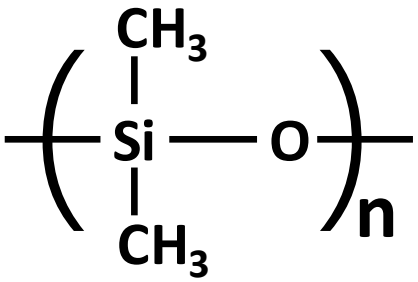

Figure 2.8 The repeat structure of silicone rubber

The values of the rating, emergency, and short circuit temperatures of XLPE, EPR, and

SIR can be a guideline for the initial conditions in accelerated aging experiments. There is also some acceptable duration suggested by the manufacturers and researchers for each material when it is exposed to certain temperature levels for a period of time. However, few physics-based models are built to demonstrate the relation between aging temperature, radiation dose, and the degree of the degradation of these polymer insulations. Furthermore, the rate of decomposition and diffusion of an antioxidant are not quantitatively estimated in the state of the art. Therefore, this research aims to develop equations to represent these phenomena.

2.2 Degradation Mechanisms

2.2.1 FTIR Characterization

The chemical reactions in polymer degradation subject to heat and radiation are often characterized by Fourier Transform Infrared Spectroscopy (FTIR) [43-45]. FTIR can both qualitatively and quantitatively analyze the chemical property of a polymer sample [46-54]. Therefore, some experimental data used to validate the proposed model in this dissertation is measured by this characterization equipment. In this section, a basic introduction to FTIR is presented.

When electromagnetic waves pass a molecule, they can interact with the chemical

bonding. The bonding structures in different molecules are not equal, which varies the transmission, reflection, and absorption patterns of the incident electromagnetic wave at different wavelengths. Besides infrared, FTIR can be equipped with visible and UV light sources providing wide ranges of analyses [55]. To simplify the concept of one measurement process, one can imagine when an infrared ray at a specific wavelength is irradiated on a sample, the intensity of the reflection or transmission is recorded by a detector. Similarly, other wavelengths are applied to the sample for detecting corresponding transmission and reflection intensity.

Because the major components of an FTIR machine include an interferometer, a beam splitter, and a computer that can perform Fourier transform, signals composed of multiple wavelengths can be processed at the same time. Hence, it is named FTIR. Therefore, in reality, multiple wavelengths are simultaneously irradiated on a sample to save the time of one measurement [55].

2.2.2 Chemical Reaction

Based on literature review, this section discusses the forming progress and measuring methods of cross-linking, chain scission, and oxidation in XLPE, EPR, and SIR, which are degraded due to heat and radiation. Relative chemical reactions are introduced. Moreover, the

absorption peaks of FTIR signals corresponding to these reaction species are elaborated.

2.2.2.1 XLPE Degradation

Polymer degradation subject to heat and radiation can be attributed to the reconstruction of molecular bonds such as cross-linking or chain scission [56-58]. The former increases molecular weight, while the latter works oppositely. These two reactions occur simultaneously in XLPE degradation [56, 59].

When exposed to radiation such as γ-ray emitted from ^{60}Co, XLPE can significantly cross-link [56]. Gel fraction (Eq. 2.1) and swelling ratio (Eq. 2.2) are two methods which are able to measure the degree of the cross-linking in polymers.

$$\text{Gel fraction} = \frac{W}{W_0} \qquad \text{Eq. 2.1}$$

$$\text{Swelling ratio} = 1 + \frac{W_s - W}{W} \times \frac{\rho}{\rho_0} \qquad \text{Eq. 2.2}$$

W is the dried insoluble part after extraction; W_0 is the initial weight of a sample; W_s is an insoluble swollen part; ρ is the density of the solvent; ρ_0 is the density of polymer [60]. Radiation can increase the concentration of free radicals and the probability of cross-linking reaction; therefore, gel ratio increases. Meanwhile, the space between cross-linking decreases,

which results in the decrease of swelling ratio. In other words, the increase of gel fraction indicates the increase of cross-linking, while the decrease of swelling ratio indicates the decrease of the space between cross-linking.

As XLPE is heated or irradiated, the chain scission from carbon-hydrogen bonds can produce alkyl radicals. These free radicals react with one another forming cross-linking, or react with oxygen forming peroxy radicals. Alkyl radicals and peroxy radicals in polyethylene can form esters, ketones, hydroperoxides, and new free radicals; the new free radicals may react with oxygen forming peroxy radicals and starting a chain reaction as shown in Eq. 2.3 and Eq. 2.4.

$$ROO^{\bullet} + RH \rightarrow ROOH + R^{\bullet} \quad \text{Eq. 2.3}$$

$$R^{\bullet} + O_2 \rightarrow ROO^{\bullet} \quad \text{Eq. 2.4}$$

Hydroperoxides may further rearrange themselves to form ketones, or decompose to form new free radicals inducing other reactions as shown in Eq. 2.5 and Eq. 2.6 [56].

$$ROOH \rightarrow RO^{\bullet} + {}^{\bullet}OH \rightarrow \text{ketone} + H_2O \quad \text{Eq. 2.5}$$

$$ROOH \rightarrow RO^{\bullet} + {}^{\bullet}OH \rightarrow ROH \text{ or } H_2O + R^{\bullet} \quad \text{Eq. 2.6}$$

FTIR is extensively used to quantify the product of the degradation reaction subject to heat and radiation in polyethylene and XLPE [43, 44]. The products reported by previous studies include carboxylic acid, ketone, ester, and aldehyde [57, 58]. Table 2.1 shows the position of the wavenumbers of some species in the FTIR spectrums of XLPE degradation. For a long time, it has been believed that ketones are the major oxidation products [61]. However, a recent research indicates that carboxylic acid is the major product according to the analyses based on the FTIR spectrums; anhydride and ester are secondary products converted from a carboxylic acid by thermal energy [57]. Relative reactions are represented from Eq. 2.7 to Eq. 2.10 [57].

Table 2.1 Wavenumber of oxidation products

Product	Wavenumber (cm^{-1})
Carboxylic acid	1713 [57]
Ketone	1735 [58]
Ester	1738 [57]
Aldehyde	1720 - 1740 [62]
Carboxylic groups	1200-1300 [34]
Carboxylic anhydride	1779 [57]
Methylene	725, 1460, 2850, 2925 [57]

$$P \text{ (polymer)} \rightarrow R^{\bullet} \text{ (polymer radical)} + H \qquad \text{Eq. 2.7}$$

$R^{\bullet} + 4\ O_2 \rightarrow 2R\text{-}COOH$ (carboxylic acid) $+ CO_2 + H_2O$ Eq. 2.8

$RCOOH + R'OH \rightarrow R\text{-}CO\text{-}OR'$ (ester) $+ H_2O$ Eq. 2.9

$RCOOH \rightarrow R\text{-}CO\text{-}O\text{-}CO\text{-}R$ (anhydride) $+ H_2O$ Eq. 2.10

2.2.2.2 EPR Degradation

The degradation of EPR subject to heat and radiation can be analyzed by FTIR. For fresh EPR, there are absorption peaks at 1690 and 1730 cm^{-1} and the intensities of these peaks change when EPR is exposed to heat and radiation; on the other hand, the absorption peaks of the oxidation product in EPR are at 1760 - 1770 cm^{-1} [63]. Studies pointed out that C=O in EPR can absorb IR at 1720 cm^{-1}; the intensity is a function of radiation dose and dose rate [64, 65]. Research also indicates that the absorption band centered at 1730 cm^{-1} is caused by the formation of the carbonyl group, which is a convenient evidence of the oxidation reaction in both XLPE and EPR [66]. For quantification, the absorption band centered at 1720 cm^{-1} can be normalized by the absorption peak at 1740 or 1150 cm^{-1} [67]; the absorption band centered at 1730 cm^{-1} can be normalized by the absorption peak at 720 or 1155 cm^{-1} [66].

2.2.2.3 SIR Degradation

Studies have indicated that the degradation of SIR subject to heat and radiation is significantly different from those of XLPE and EPR [68-71]. Before degradation, the cross-linking between the main chains is illustrated in Figure 2.9. R is the representation of C_nH_{2n}. R versus Si by number ratio is about 0.01, for example. When heat or radiation is applied, the Si-CH_3 in the main chain can form Si-$CH_2^{\bullet}$ radicals and induce subsequent reactions. For example, in oxygen sufficient environment, oxidation reaction can cross-link two silicon atoms that were not bonded, which is shown in Figure 2.10. In addition to the occurrence of cross-linking, heat and radiation can also introduce the decomposition of the original cross-link shown in Figure 2.11 [71].

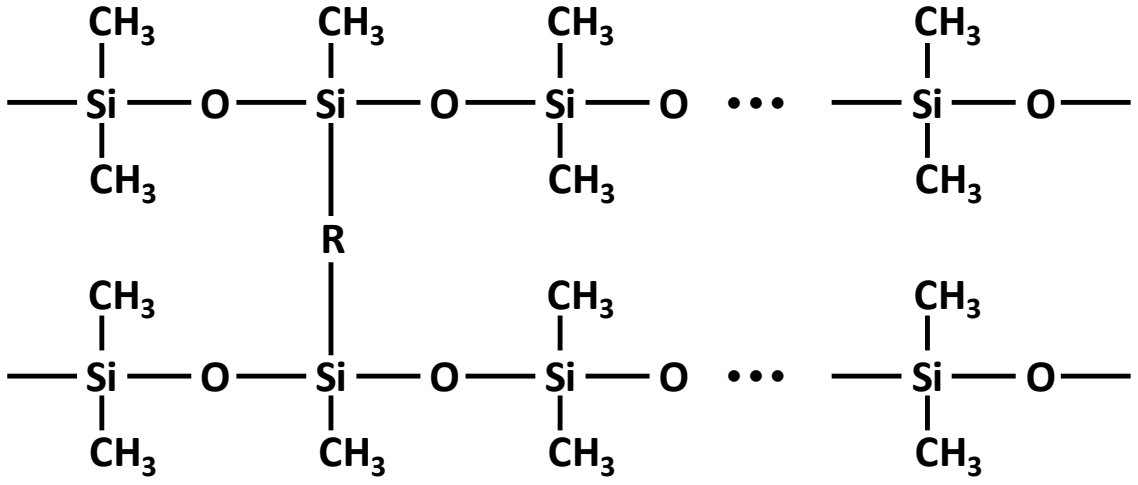

Figure 2.9 Illustration of the cross-linking of SIR before degradation

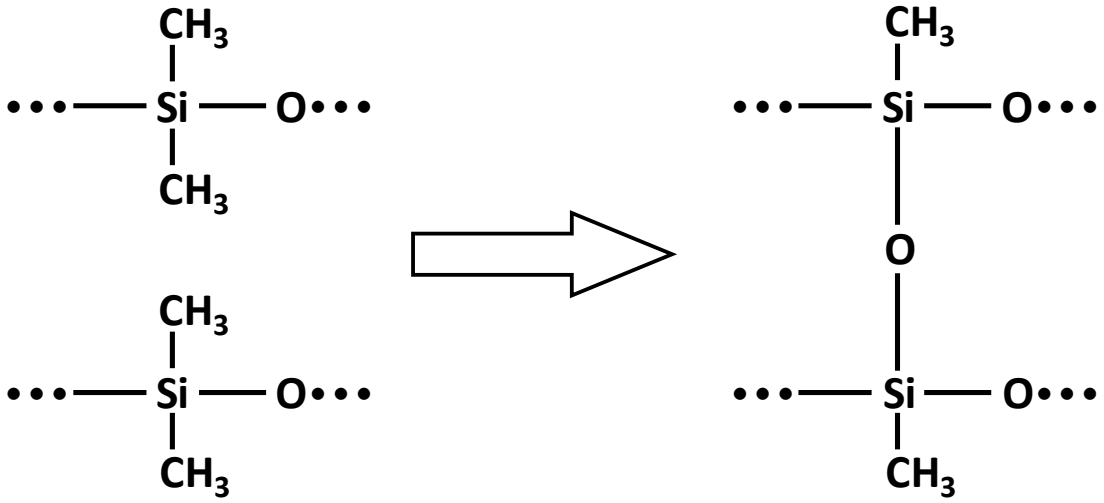

Figure 2.10 Crossing-linking forms during oxidation reaction in SIR

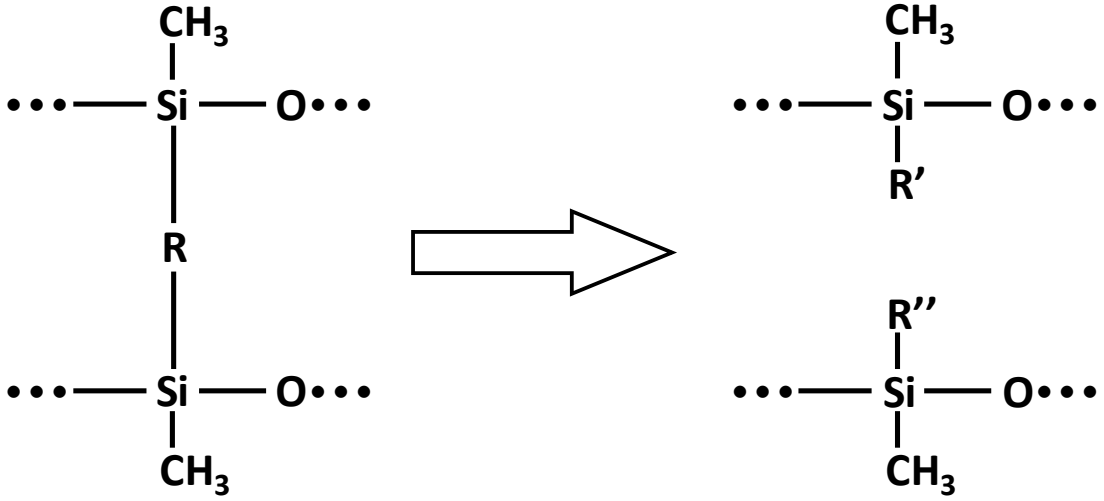

Figure 2.11 The decomposition of the original cross-linking between two main chains in SIR during thermal or radiation aging

The FTIR spectrum of an SIR shows the absorption peaks: CH_3 at 2960 and 2870 cm^{-1},

$Si\text{-}(CH_3)_2$ at 1259 cm^{-1}, and Si-O-Si at 1065 cm^{-1} [71]. However, this research pointed out that the degradation of SIR samples cannot be followed up by the FTIR signals which are usually applied to the analysis of the chemical reaction in XLPE, EPR, and the antioxidant subject to heat and radiation; the reason of this unavailability is not detailed in the paper [28, 33, 71].

According to the discussion above, it is worth noting that the chemical reactions due to heat and radiation in XLPE, EPR, and SIR cannot be easily and individually considered. Radiation factors such as dose rate and accumulated dose, degradation environment such as ambient temperature and oxygen concentration, and even the recipe of a polymer such as the type of antioxidant can tremendously affect degradation rate. Owing to the complexity, this dissertation invented a method to bypass all these difficulties and developed a physics-based model which can intuitively estimate the aging rate of XLPE, EPR, and SIR.

2.2.3 Degradation Kinetics

In the degradation kinetics of cable insulation subject to heat and radiation, an aging progress can be viewed as the combination of the three aspects, which are:

a. The amount of the products of the reactions in a finite system

b. The distribution of the product from a sample surface to the core

c. The evolution of a. and b. when time elapses

How to model a. b. and c. by physics-based methods requires the understanding of the degradation kinetics. Polymer degradation is the result of chemical reactions when time elapses. Degradation kinetics may be basically divided into two categories: reaction control and diffusion control.

In order to initiate a chemical reaction, multiple steps may be required. For example, first, sufficient reactants must diffuse from a free surface to the reaction interface. Second, at the reaction surface, enough energy is required to overcome an energy barrier.

Reaction control means that the bottleneck, or the slowest reaction step, is at the interface of a chemical reaction. In other words, the supply of the reactant, or the first step, is faster than the consumption of the reactant at an interface. Take oxidation reaction for instance, when it is reaction control, homogeneous oxide concentration along a sample cross-section can be represented by Figure 2.12 (a). In this condition, a sample degrades as a whole. The insignificant difference of oxide concentration from the surface to the core is illustrated in Figure 2.13 (a) [72, 73]. This phenomenon observed on a cross-section is named homogeneous oxidation.

On the other hand, in diffusion control, the bottleneck for a reaction is determined by the transportation speed of reactants. When oxidation occurs inside a sample, oxygen molecules

must travel from the surface toward the core of a sample by diffusion mechanism. If diffusion is slower than the chemical reaction at a reaction interface, the process is termed diffusion control whose oxide concentration and schematic illustration are shown in Figure 2.12 (b) and Figure 2.13 (b), respectively [72, 73]. In other words, the concentrations of oxide and oxygen molecules along the cross-section of a sample shall be unevenly distributed, or often termed heterogeneous degradation.

Two of the goals of this research are to develop physics-based models to represent the reaction- and diffusion-control degradation of cable insulation, and to connect the models to material properties such as mechanical and electrical properties in order to define and determine the remaining life of cable insulation.

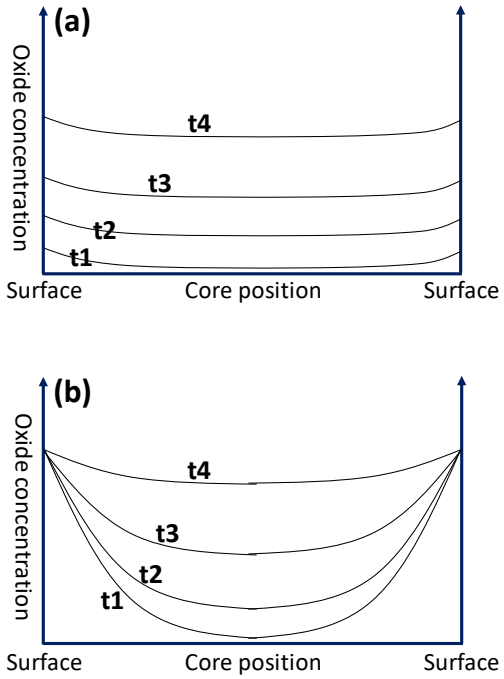

Figure 2.12 Oxide distribution of homogeneous and heterogeneous degradation

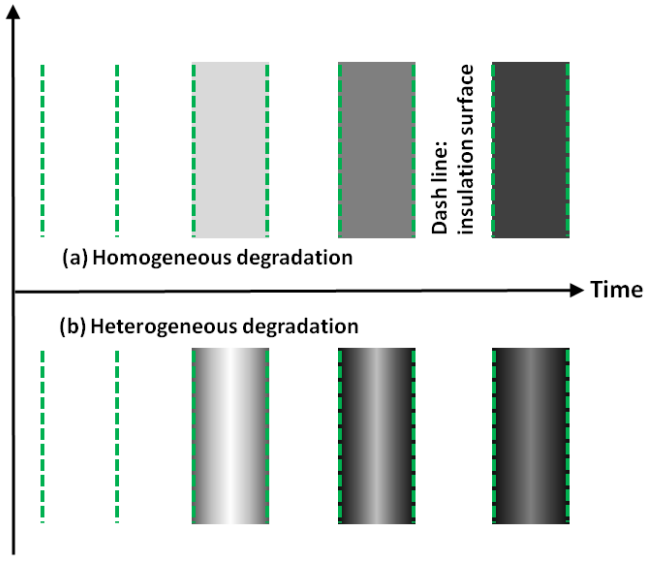

Figure 2.13 Schematic representation of oxide distribution, the darker part means higher oxide concentration

2.2.4 Effect of Antioxidant

Antioxidants are added in cable insulation to prevent the polymer from degradation [28, 33, 34] which is mainly attributed to oxidation reactions [58]. For oxidation to occur under the surface of cable insulation, oxygen molecules need to migrate from a free surface toward the core of the polymer. This migration takes many steps (long distance) and seems more difficult than the reaction at polymer/oxygen interface where the reaction only takes one step (short distance) to happen. Therefore, intuitively, diffusion control should dominate; in other words, it is common to have diffusion control resulting in heterogeneous oxidation as shown in Figure 2.12 (b) and Figure 2.13 (b) [74]. However, studies have reported that antioxidant at sufficient concentration in a polymer can significantly decrease the probability of the occurrence of the oxidation reaction, which renders reaction control and homogeneous oxidation as shown in Figure 2.12 (a) and Figure 2.13 (a) [33, 34]. It is worth noting that antioxidant may diffuse out of a polymer and also decompose in the polymer due to external energy such as heat and radiation, which leads to the deficient of antioxidant whose concentration was originally high enough. A qualitative research had been conducted to study the loss of antioxidant in the literature review [34].

2.3 Definition of Degradation

The definition of the degradation of cable insulation can be based on the deterioration of the performance of the polymer as a function of time when heat and radiation are applied. The performance of cable insulation is usually focused on two aspects:

a. Mechanical properties

b. Electrical property

Both properties are corresponding to the chemical properties resulting from the chemical reactions in the polymers.

2.3.1 Chemical Property

In the studies of polymer degradation, oxidation index (OI) measured by FTIR is the most widely-used indicator that can quantify the degree of aging when chemical properties are considered [34, 54]. OI increases during the aging of an insulation layer. In the degradation of polyethylene, OI can be determined by Eq. 2.11 [54, 75] or Eq. 2.12 [34].

$$OI_a = \frac{A_{a1}}{A_{a2}} \quad \text{Eq. 2.11}$$

$$OI_b = \frac{A_{b1}}{A_{b2}} \quad \text{Eq. 2.12}$$

In the first equation, A_{a1} is the triangular area under the peak of the reaction product of interest such as carbonyl species; A_{a2} is the triangular area under a reference peak, which is for normalization. In the second equation, Ab_1 is the height of the absorption peak; A_{b2} is the thickness of a sample in a transmission measurement, which is also for normalization. The concept of both equations is to connect the absorption intensity of FTIR and the amount of the product rendered by chemical reactions.

2.3.2 Mechanical Property

The mechanical property used to define the degree of the degradation of cable insulation is ductility. Ductility decreases during the degradation. When cables are subject to mechanical force, enough ductility can prevent the insulation layer from breaking or peeling off which can cause a short circuit. Therefore, IAEA suggests 0.5 be the lowest acceptable value for the ductility of cable insulation. In relative research, ductility is usually represented by EAB defined by Eq. 2.13 [3, 20, 24]. EAB measurements show good repeatability, which is one of the reasons makes EAB become a widely-accepted criterion for quantifying the degree of the aging of cable insulation in the filed applications [76].

$$EAB = \frac{l_f - l_0}{l_0} \qquad \text{Eq. 2.13}$$

l_f is the length of a sample at fracture in a tensile test. l_0 is the original length of the sample.

2.3.3 Electrical Property

Resistivity is used as an indicator to quantify the degree of degradation when cable insulation is exposed to heat and radiation. Studies indicate that resistivity decreases when aging occurs [26, 77-79]. Resistance is measured by I-V curves; usually about 100 - 1,000 voltage is applied. I-V curves can determine resistance by Eq. 2.14 and then resistivity is calculated by Eq. 2.15.

$$v = I \times R \qquad \text{Eq. 2.14}$$

v is voltage; I is current; R is resistance.

$$\rho = R \times \frac{A}{l} \qquad \text{Eq. 2.15}$$

ρ is resistivity; A is the area of the cross-section of a sample; l is the length of a sample.

2.4 State of the Art in Model Development

A theoretical model that can calculate the remaining life of cable insulation

corresponding to the degree of chemical reaction has not been developed to date. Similarly, we have not found a method that can predict the resistivity as a function of time in the literature review. However, two empirical models which are able to plot the EAB as a function of time have been proposed. They are Superposition of Time Dependent Data model (TDD) and Superposition of Dose to Equivalent Damage Data model (DED) [20, 80]. In order to obtain the values of the parameters in these two models, the first step is to conduct several accelerated aging experiments at different temperature and dose rate. In the second step, activation energy can be estimated by the accelerated aging experiments at different temperatures. These two steps and the two models are sequentially discussed in this section.

2.4.1 Accelerated Aging Experiment

Discernible or significant degradation of cable insulation in the conditions of field applications may take several years or even decades to be noticeable. In order to measure the degree of aging in limited time, accelerated conditions are developed. Arrhenius equation (Eq. 2.16) is the fundamental concept used in the models derived from accelerated aging experiments.

$$\nu = \nu_0 \times \exp\left(\frac{-\Delta G}{k\,T}\right) \qquad \text{Eq. 2.16}$$

where ν is the success rate of an event in a short period of time whose unit is [1/time]. ν_0 is a constant termed attempt frequency whose unit is [1/time]. ΔG is activation energy. k is Boltzmann constant. T is absolute temperature.

Basically, accelerated aging experiments are performed at a higher temperature at which the success rate of a reaction is higher so detectable reaction product can be observed sooner. By using Eq. 2.16, repeating the experiments at multiple temperatures (T), and measuring the corresponding reaction rates (ν), the ν_0 and ΔG can be determined. When ν_0 and ΔG are acquired, by plugging them back into Eq. 2.16, the reaction rates (ν) at a lower temperature, application temperature, for example, can be estimated. It is worth noting that in real experiment procedures, Eq. 2.16 is usually rewritten in logarithm form (Eq. 2.17), which can be plotted in Figure 2.14 with ln(ν) on the y-axis and (1/T) on the x-axis. By linear fitting the measured data, ΔG and ν_0 can be determined from the slope and intercept of the line.

$$\ln \nu = \frac{-\Delta G}{k} \left(\frac{1}{T}\right) + \ln \nu_0 \qquad \text{Eq. 2.17}$$

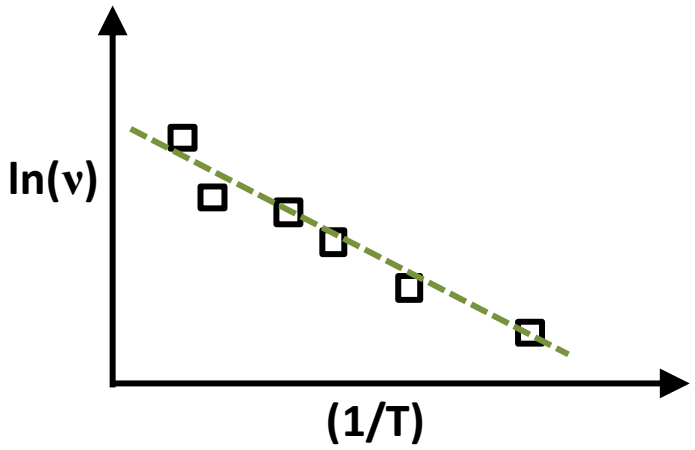

Figure 2.14 Determine the activation energy (ΔG) in Arrhenius equation by linear fitting where the slope is (-ΔG/k)

Though the foundation of accelerated aging experiments is based on the correlation between different temperatures via Arrhenius equation, in the literature review, other degradation factors such as accumulated dose and dose rate are also applied by this concept [80, 81]. By establishing the relation between radiation and temperature, Arrhenius equation has been applied empirically. In other words, Arrhenius equation is used to incorporate other degradation factors besides temperature [6, 20, 24, 80, 82]. Examples will be elaborated in the following paragraphs.

2.4.2 Activation Energy

Before discussing the empirical degradation models, this section gives an example of

how the activation energy of XLPE is determined in a literature review. The activation energy here is apparent activation energy representing the sum up of the overall effects in the degradation reactions in a polymer, which is different from the physicochemical activation energy [24].

The concept is to inverse the frequency term in Eq. 2.16 because the authors of the papers assumed the required degradation time can be represented by the inverse of the frequency, though this concept is not strictly physics-based [24, 80]. By this assumption, the degradation time can be represented by Eq. 2.18 and its logarithm form is Eq. 2.19, which is applicable to the curve-fitting method similar to Eq. 2.17 and Figure 2.14.

$$t = t_0 \times \exp\left(\frac{\Delta G}{k\,T}\right) \qquad \text{Eq. 2.18}$$

$$\ln t = \frac{\Delta G}{k}\left(\frac{1}{T}\right) + \ln t_0 \qquad \text{Eq. 2.19}$$

where t is the time required to reach a certain degree of degradation; t_0 is time constant.

The following example is excerpted from Fig. 2.1-1 of a report [24]; the XLPE was subject to thermal aging and no radiation was applied. At 100℃, it took 10,730 hours for the sample to reduce its EAB to 400%. At 110℃, it took 3,664 hours for the sample to reach the same EAB value. In order to apply Eq. 2.19, (1/T) on x-axis and ln(t) on y-axis are plotted.

(x_1,y_1) and (x_2,y_2) from the above data are equal to [1/(273+100), ln(10,730)] and [1/(273+110),ln(3,664)], respectively. The slope of the line connecting these two points is 15,350. For one mole polymer, the ΔG is equal to ($k \times N_0 \times 15{,}350 = 128$ kJ/mol) where N_0 is Avogadro constant.

The method used to determine activation discussed above hints that activation energy is independent of temperature. However, some studies suggest that activation energy decreases as temperature decreases, which can lead to the overestimation of the lifespan of cable insulation when Arrhenius equation with constant activation energy is directly applied [6, 20].

2.4.3 Superposition of Time Dependent Data (TDD)

The first empirical degradation model in literature review is Superposition of Time Dependent Data (TDD) model [6, 20, 24, 82] used to predict the degradation of cable insulation subject heat and radiation. It is extensively discussed in the studies [6, 20, 24, 80-83]. There are other names for this approach such as time-temperature superposition [80, 83] and time-temperature-dose rate superposition [81].

TDD model may be suitable only for the application in the environment with very low dose rate [20]. The central concept of TDD model is based on a shift factor, denoted “a” in Figure 2.15, establishing the relation between two curves, one of which is the master curve at

a reference temperature (T_{ref}) with zero radiation. In other words, the master curve is the base of the prediction. By multiplying a shift factor to a master curve, the EAB curve at a specific temperature and dose rate can be determined. The shift factor represented by Eq. 2.20 and Eq. 2.21 is a function of temperature and dose rate; k and x are empirical parameters; E is activation energy. For example, when point p in Figure 2.15 is multiplied by the shift factor $a(T,D)=a_1$, point q is determined. k and x can be determined by the following method.

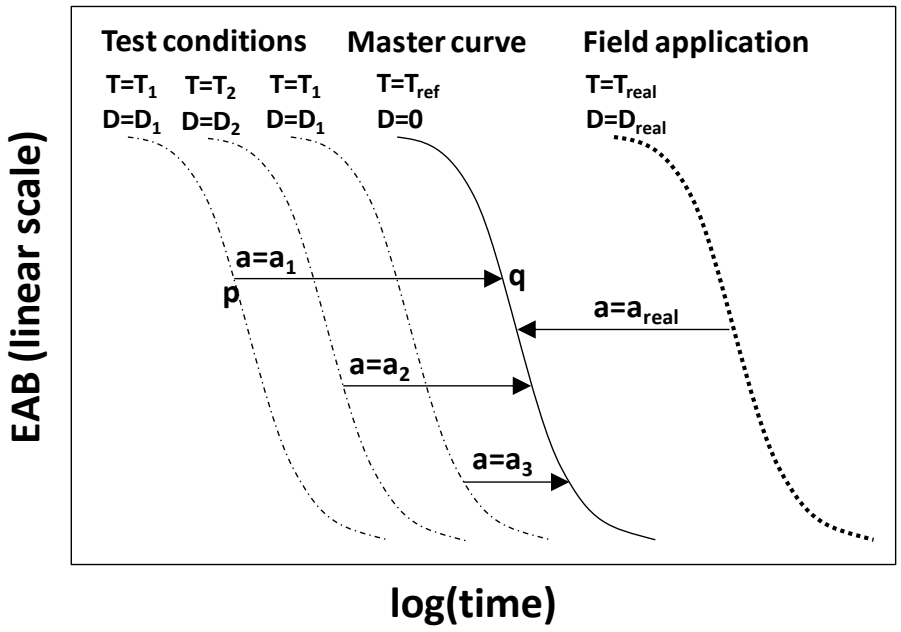

Figure 2.15 The illustration of Superposition of Time Dependent Data (TDD)

$$a = \exp\left[\frac{-E}{R}\left(\frac{1}{273+T}-\frac{1}{273+T_{ref}}\right)\right]\cdot \left\{1+k\,D^{x}\exp\left[\frac{E\,x}{R}\left(\frac{1}{273+T}-\frac{1}{273+T_{ref}}\right)\right]\right\} \quad \text{when } T \neq T_{ref} \qquad \text{Eq. 2.20}$$

$$a = 1 + k\,D^{x} \qquad \text{when } T = T_{ref} \qquad \text{Eq. 2.21}$$

a: Shift factor with no unit

E: Activation energy [kJ/mole], which can be determined by Eq. 2.18

R: Gas constant = 8.314 [J/mol・K]

T: Evaluation Temperature [℃]

T_{ref}: Reference temperature [℃]

D: Evaluation dose rate [Gy/time]

In order to determine parameters k and x, simplifying the notation in Eq. 2.20 by Eq. 2.22 facilitates the calculation.

$$A = \exp\left[\frac{-E}{R}\left(\frac{1}{273 + T} - \frac{1}{273 + T_{ref}}\right)\right] \qquad \text{Eq. 2.22}$$

Therefore, Eq. 2.20 can be represented by Eq. 2.23

$$a = A(1 + k\,D^{x}\ A^{-x}) \qquad \text{Eq. 2.23}$$

Eq. 2.24 is the rearrangement of Eq. 2.23.

$$\frac{a}{A} - 1 = k\left(\frac{D}{A}\right)^{x} \qquad \text{Eq. 2.24}$$

Express Eq. 2.24 into the form of logarithm, Eq. 2.25 is obtained.

$$\log\left(\frac{a}{A} - 1\right) = x \log\left(\frac{D}{A}\right) + \log(k) \qquad \text{Eq. 2.25}$$

Perform multiple sets of experiments at different temperatures and dose rates. Plot [log(D/A)] on the horizontal axis and corresponding [log(a/A-1)] on the vertical axis of a Cartesian coordinate. Run linear regression to obtain a straight line. The slope determines the value of the parameter x and the intersection determines the value of the log(k) [20].

2.4.4 Superposition of Dose to Equivalent Damage Data (DED)

The second empirical degradation model in literature review is Superposition of Dose to Equivalent Damage Data (DED) model. It is discussed in the studies [20, 24, 80, 82]. The schematic illustration and the empirical equation used in this model are shown in Figure 2.16 and Eq. 2.26, respectively. It should be noticed that the method used to determine the activation energy (E) in Eq. 2.26 is different from that used in TDD model. The E in DED

model is determined by trial and error [80], though it is possible to obtain an E value of DED model close to that determined by TDD model [82]. The procedures for performing DED model are as follows:

a. Only one value of the degree of the degradation is plotted in one DED plot. For example, all the data points in Figure 2.16 represent EAB = 100%.

b. The vertical axis in Figure 2.16 is Dose to Equivalent Damage (DED) whose value equals to [(time) × (dose rate)].

c. Perform multiple sets of experiments at different temperatures and dose rates. Obtain data points denoted by the hollow circles, squares, and rhombus in Figure 2.16, for example.

d. The points in hollow symbols are shifted to a reference temperature (T_{ref}) by Eq. 2.26. The activation energy (E) can be determined by trial and error [80] in order to form a smooth curve determined by the solid symbols at the left of Figure 2.16.

e. Finally, degradation time can be predicted at the reference temperature (T_{ref}) corresponding to different dose rates scaled by the horizontal axis of Figure 2.16.

When dose rate is very small, the effect of radiation becomes insignificant; thermal energy should dominate the whole degradation. For example, at a certain temperature, when dose rate is 0.002 Gy/hour, it takes 50,000 hours for EAB to decrease from 500% to 100%, which makes $DED_1 = 0.002 \times 50{,}000$. If dose rate is 0.001 at the same temperature, it should

take roughly the same duration of time (50,000 hours) to reach the same degree of degradation, which makes $DED_2 = 0.001 \times 50{,}000$. Therefore, DED_1 is linearly proportional to DED_2 as a function of dose rate when the dose rate is very small. This relation is illustrated by the dashed straight line denoted by T_{ref} in Figure 2.16.

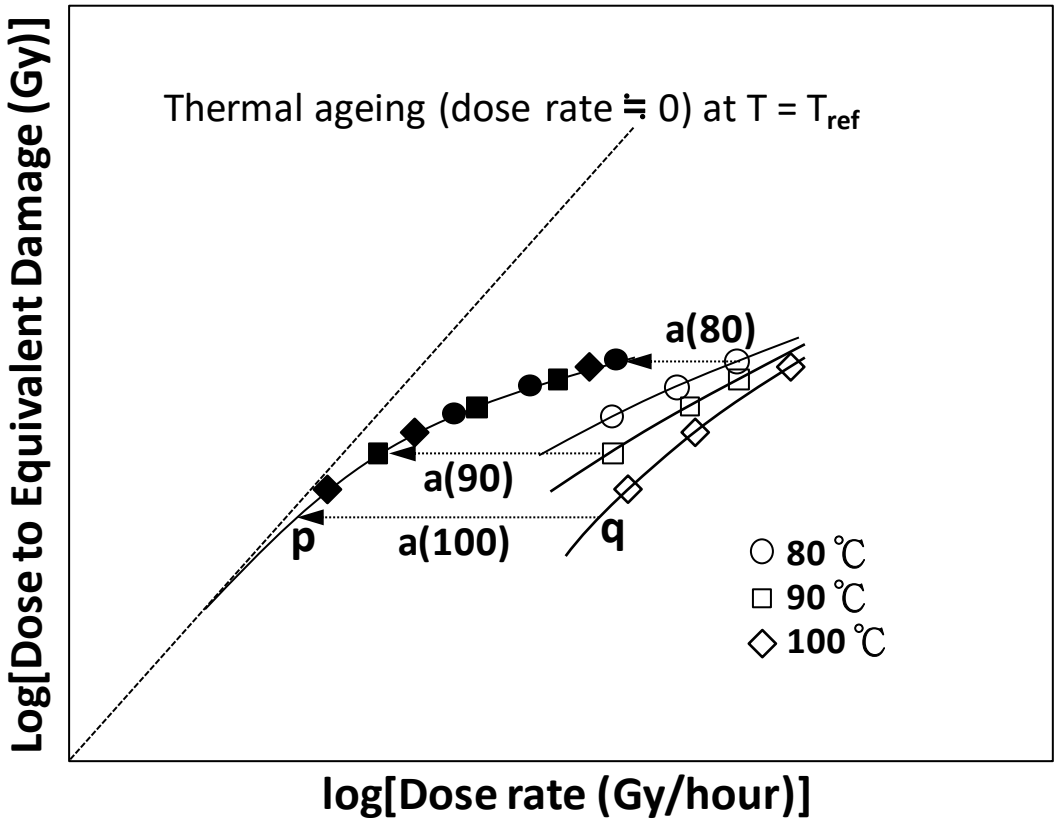

Figure 2.16 The illustration of Superposition of Dose to Equivalent Damage Data (DED)

$$a(T) = \exp\left[\frac{-E}{R}\left(\frac{1}{273+T} - \frac{1}{273+T_{ref}}\right)\right] \qquad \text{Eq. 2.26}$$

a: Shift factor with no unit

E: Activation energy [kJ/mole], which is determined by trial and error [80, 82]

R: Gas constant = 8.314 [J/mol・K]

T: Evaluation Temperature [℃]

T_{ref}: Reference temperature [℃]

Chapter 3: Mechanical Degradation

3.1 Degradation Mechanism

3.1.1 Diffusion Control

Research indicates that the degradation of cable insulation is mainly caused by the oxidation of the polymer [28, 33, 34, 63, 80]. In a polymer, if there is no or limited amount of antioxidant, the polymer has an insufficient capability to deter the oxidation at reaction interfaces [34], so the oxidation kinetics can be controlled by the speed of the movement of oxygen diffusing from a free surface to the core of the insulation. In other words, the oxidation is diffusion-controlled rather than reaction-controlled. In diffusion kinetics, the profile of oxygen concentration at the cross-section of a polymer must obey Eq. 3.1 and Eq. 3.2, which are Fick's 1st and 2nd laws, respectively [84, 85].

$$J = -D\frac{\partial \mathrm{c}}{\partial \mathrm{x}} \qquad \text{Eq. 3.1}$$

J: flux = [#/(area-time)]

D: oxygen diffusivity in a polymer = [length^2/time]

c: concentration = [#/volume]

x: the length from the surface to the core on a cross-section.

$$\frac{\partial c}{\partial t} = D\frac{\partial^2 c}{\partial x^2}$$ Eq. 3.2

t: time

The boundary conditions of these partial differential equations are:

a. At time t = 0 and 0 < x < L, the oxygen concentration c(x,t) is zero. L is the thickness of a sample.

b. $c(0,t) = c_0$ and $c(L,t) = c_0$

c. $c(x,\infty) = c_0$

Moreover, by two mathematic techniques: d and e, Eq. 3.3 is obtained.

d. Separation of variables to separate space and time

e. Fourier series

The profile of the oxygen concentration on a cross-section can be represented by Eq. 3.3 [84, 85]. x is the distance from a surface; t is aging time; c_0 is the oxygen concentration at the surface. L is sample thickness. τ_0 is the time point when the concentration of the oxide becomes discernible. Usually, τ_0 is zero. $(t-\tau_0) \geqq 0$. Diffusivity D depends on Arrhenius equation which can predict c(x,t) at different temperatures.

$c(x,t) = c_0 -$ Eq. 3.3

$$\frac{4\,c_0}{\pi}\sum_{j=0}^{n}\left\{\left[\frac{1}{2\mathrm{j}+1}\sin\frac{(2j+1)\pi x}{\mathrm{L}}\right]\left[\exp\left(-\left[\frac{(2\mathrm{j}+1)\pi}{\mathrm{L}}\right]^2\mathrm{D}\,(\mathrm{t}-\tau_0)\right)\right]\right\}$$

Since cable insulation is solid, the concentration of polymeric molecules is constant. When oxidation reaction is diffusion-controlled, the concentration of oxide shall be proportional to that of oxygen. Hence, Eq. 3.3 can also represent the concentration profile of oxide if c_0 is the oxide concentration at a sample surface. The oxidized ratio in insulation is the integral of Eq. 3.3 multiplied by a constant.

3.1.2 Reaction Control

In reaction-controlled degradation, virtual degradation ratio (V_d) can be obtained by the concept of exponential distribution, which is detailed in Appendix A. In other words, V_d is the same to the concept of Eq. a. 15. The meaning of ν corresponds to that of λ in Eq. a. 15 and Eq. a. 20. To be more specific, within a limited volume, ν part of the material is degraded during a short time interval. Therefore, the accumulated degraded part can be represented by the CDF of an exponential distribution, shown in Eq. 3.4 [86] where t is time.

$$\mathrm{V_d} = 1 - \exp(-\nu \times \mathrm{t}) \qquad \text{Eq. 3.4}$$

3.2 Modeling Elongation at Break

3.2.1 Trend of Elongation at Break

In related research [20, 80], experimental data of EAB is conventionally plotted against a logarithmic time axis as shown by the squares in Figure 3.1(a). In order to analyze the dynamic drop-off rate of the EAB as a function of time, a linear x-axis is plotted in Figure 3.1(b), which visually shows that the squares form a long tail with a gradually decreasing slope. Studies and experiments indicate that the entire EAB trend should be similar to an S-shaped curve similar to the "sketched line" in Figure 3.1(a) & (b) [20, 24].

Modeling an S-shaped curve may require parameters to define the curvatures of the concave section, convex section, and the inflection point. More parameters lead to more assumptions, which should not be pragmatic in field application. Besides, this research focuses on the long-term EAB where the dynamic curvature of EAB is convex with a gradually decreasing slope. In other words, the shape of the tail of the S curve is more important than that of the front in the application. Therefore, this study models the S curve by a combination of one horizontal section and one convex section, as shown by the dashed and dotted lines in Figure 3.1, which requires only two parameters. The first parameter is the length of incubation time (τ_0), which is denoted by the length of the line y = 0 in Figure 3.2.

The second parameter is drop-off rate (ν), which is represented by the length of the vertical line in Figure 3.2. Combining multiple discrete domains to approximate one continuous phenomenon is a common approach which has been used for a long time in many areas [87-89]. The length of the horizontal section in Figure 3.1 is incubation time (τ_0), which is the same to the section of y = 0 in Figure 3.2. The dynamic curvature of the dotted line in Figure 3.1 can be determined by a function of ν, which is the drop-off rate denoted by the length of the vertical line in Figure 3.2. Larger ν means that the dotted line in Figure 3.1 is steeper.

It is worth noting that the dash and dot lines in Figure 3.1 are plotted by δ=1 and equation Eq. 3.20 developed by this research with τ_0 = 2150 hours and ν = 6E-4 /hour. The modeling approach comprising these two parameters will be detailed in this section and the section on validation.

Experimental data [20, 80] usually shows that when aging temperature or dose rate increases, incubation time (τ_0) or the length of the dash lines decreases, as shown in Figure 3.3; in the same conditions, the dot lines in Figure 3.3 “usually” drop faster, which means ν is larger. Both trends indicate that higher inputted energy may result in higher reaction rate. The evolutions of τ_0 and ν corresponding to the change of aging temperature and dose rate are not random. The logic of this research is to find the trends of τ_0 and ν to determine EAB as a function of time.

It should be emphasized that the ν here is not measured by chemical reaction; it is characterized only by the drop-off rate of EAB. It is also worth noting that the increase of drop-off rate is not always resulted from the increase of dose rate. One exception is EPR [20].

To sum up the logic of this approach, an EAB function with a variable t (time), a parameter ν (drop-off rate), and a parameter τ_0 (incubation time) will be derived in this chapter to represent the dotted line in Figure 3.1. By fitting ν and τ_0 to experimental data plotted by the squares in Figure 3.1, the EAB as a function of time can be determined. The logic of this fitting approach is a method commonly used in many areas [88-91].

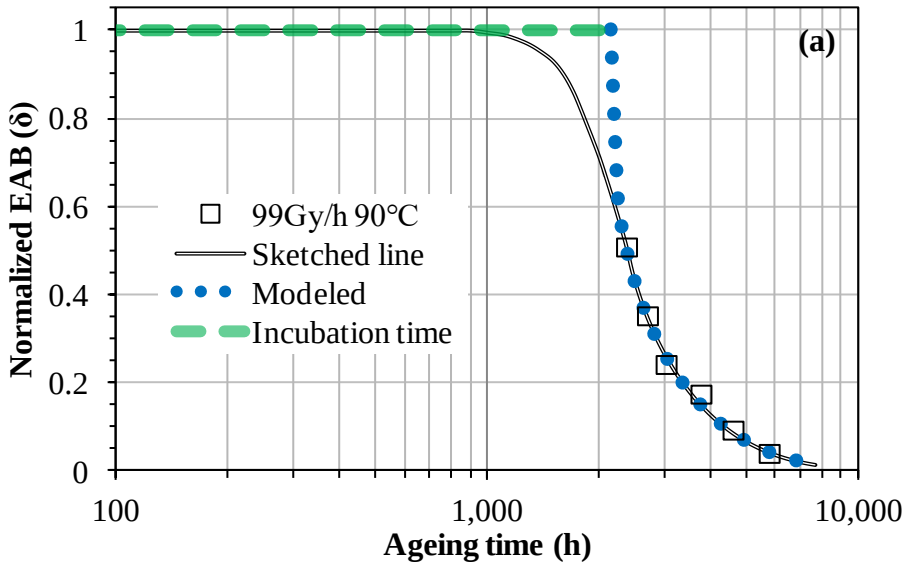

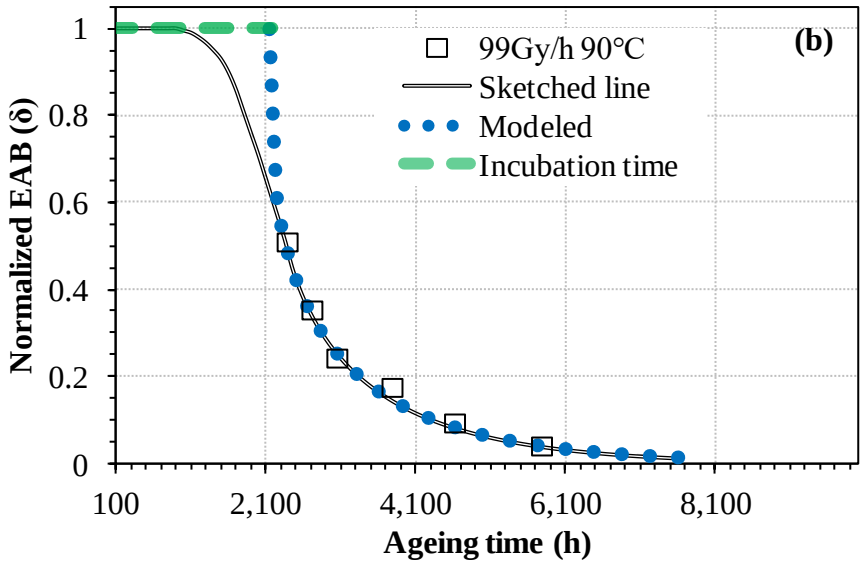

Figure 3.1 Normalized EAB of FR-EPR (company A) as a function of time represented by (a) logarithmic x-axis, and (b) linear x-axis. Squares are experimental data [20]. The dotted line is plotted according to Eq. 3.20. The x-axis of (a) and (b) are the same for comparison.

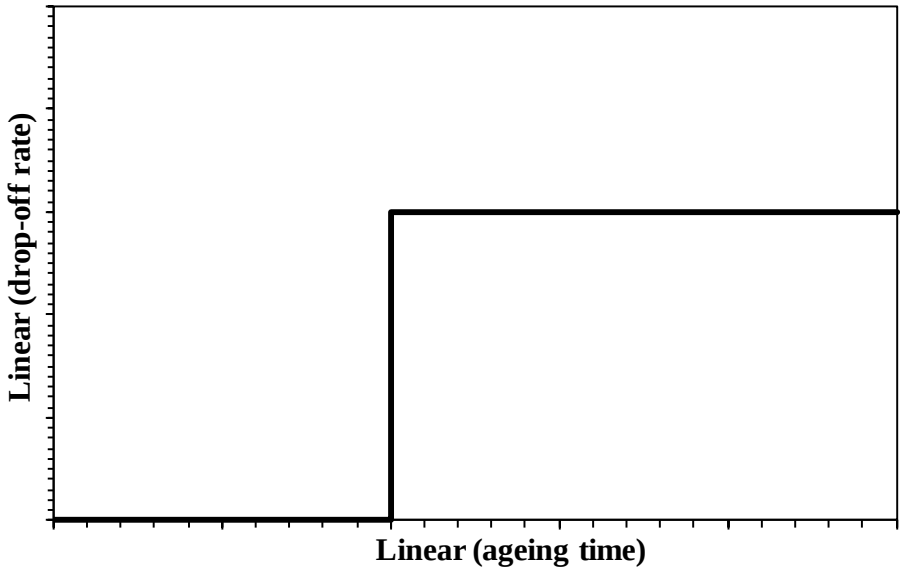

Figure 3.2 Modeled drop-off rate before and after incubation time.

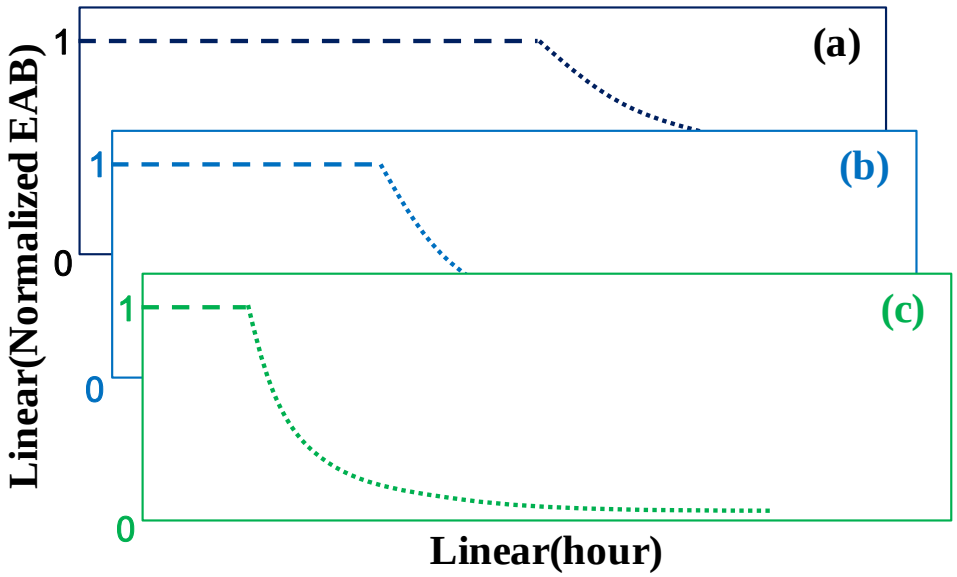

Figure 3.3 An example of the trends of incubation time (dash lines) and dynamic drop-off rate (dot lines) at (a) lower, (b) medium, and (c) higher aging temperature or dose rate

3.2.2 Dichotomy Model

The concept of this model is based on the virtual amount of the yield of a degradation reaction. This degradation reaction is modeled by EAB but not measured by any chemical approach [92-94].

For a tensile test, a specimen in any shape can be modeled by the combination of an infinite number of identical unit cubes shown in Figure 3.4(a). Each unit cube can be further divided into m equal subcubes, shown in Figure 3.4(b) & (c).

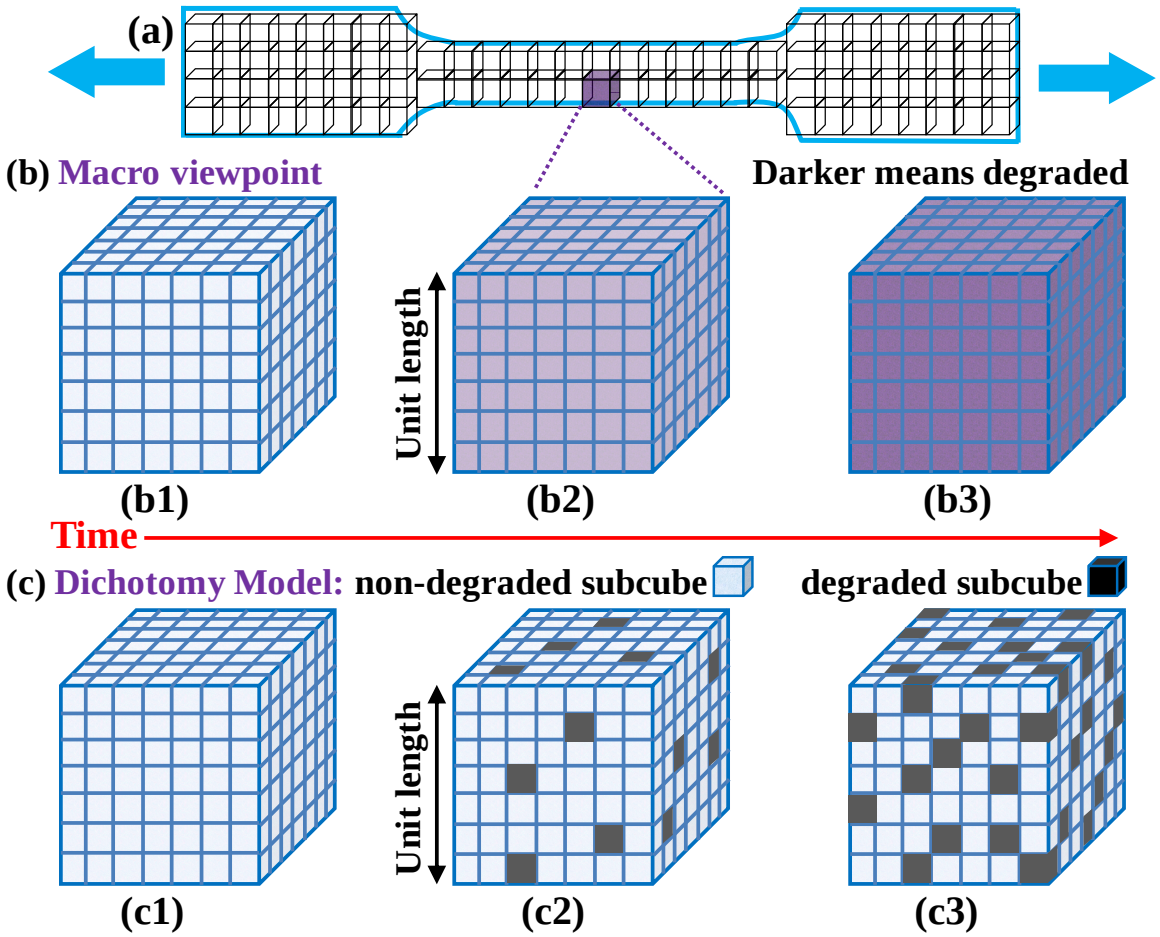

Figure 3.4 Illustration of Dichotomy Model

Antioxidant is added when cable insulation is manufactured. Sufficient antioxidant converts oxidation reaction from diffusion control to reaction control [34]. Diffusion control renders a heterogeneous cross-section while reaction control results in a uniform cross-section. Hence, this model assumes the degradation occurs uniformly. Another paper also reported that homogeneous oxidation exists [80].

In each unit cube, the volume ratio of the "virtually" degraded part is V_d. Among m

subcubes, there are n subcubes which are degraded, or m-n subcubes are not degraded. The side length (d) of one subcube can be represented by Eq. 3.5.

$$d = \left(\frac{V_d}{n}\right)^{(1/3)} \qquad \text{Eq. 3.5}$$

In a unit cube, along one line parallel to the elongation direction, there are k degraded subcubes. This number k is represented by Eq. 3.6 and shown in Figure 3.5 whose d denotes degraded subcubes while p means non-degraded polymer.

$$k = n^{(1/3)} \qquad \text{Eq. 3.6}$$

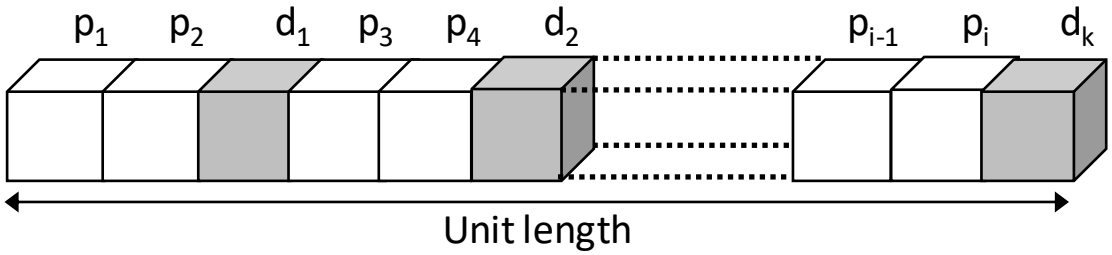

Figure 3.5 One of the rows along the elongation direction in a unit cube after aging but before a tensile test (colored cubes represent the degraded part)

a. The Elongation at Break before degradation (EAB_I) for a unit cube can be represented by

Eq. 3.7.

$$EAB_{\mathbf{I}} = \alpha \times 1 - 1 \qquad \text{Eq. 3.7}$$

where α is termed elongation factor, which is a real number not less than 1.

b. After aging, only the non-degraded parts, p_1, p_2, …p_i, maintain their elongation factor at the original value α, which mainly contributes to the elongation in a unit cube. The value of the elongation factor of the degraded part $\alpha_{\mathbf{d}}$ is assumed to be very close to one, which will be validated in the section on validation. The Elongation at Break after degradation ($EAB_{\mathbf{II}}$) for a unit cube can be represented by Eq. 3.8.

$$EAB_{\mathbf{II}} = \alpha (1 - \Sigma d_k) + \alpha_d (\Sigma d_k) - 1 \qquad \text{Eq. 3.8}$$

where $\Sigma d_{\mathbf{k}}$ can be calculated by Eq. 3.5 and Eq. 3.6, shown by Eq. 3.9.

$$\Sigma d_k = n^{(1/3)} \left(\frac{v_d}{n}\right)^{(1/3)} \qquad \text{Eq. 3.9}$$

Plug Eq. 3.9 into Eq. 3.8, Eq. 3.10 can be obtained.

$$EAB_{II} = \alpha\,[1 - V_d^{(1/3)}] + \alpha_d\, V_d^{(1/3)} - 1 \qquad \text{Eq. 3.10}$$

The ratio of EAB (δ) after and before aging can be obtained via dividing Eq. 3.10 by Eq. 3.7, which is shown by Eq. 3.11.

$$\frac{EAB_{II}}{EAB_I} = \delta = \frac{\alpha\left[1 - V_d^{\frac{1}{3}}\right] + \alpha_d\left[V_d^{\frac{1}{3}}\right] - 1}{\alpha \times 1 - 1} \qquad \text{Eq. 3.11}$$

Since α_d is very close to one, Eq. 3.11 can be simplified as a function of V_d, shown by Eq. 3.12.

$$\text{Normalized EAB} = \delta = \frac{EAB_{II}}{EAB_I} \cong 1 - (V_d)^{(1/3)} = f(V_d) \qquad \text{Eq. 3.12}$$

Eq. 3.12 is named δ-function since normalized EAB is symbolized δ in this research. This approach is named Dichotomy Model because virtually degraded and virtually fresh subcubes are modeled in Figure 3.5. It is worth noting that according to the mathematic derivation of this model, the size of the subcubes can be infinitely small, which can model a specimen in any shape such as a cylindrical cable insulation in field application. The following sections discuss how to determine V_d.

3.2.3 Dichotomy Model - Diffusion Control

The oxidation reaction itself can be represented by Eq. 3.13 and Eq. 3.14.

$$P + O_2 \rightarrow PO_2 \qquad \text{Eq. 3.13}$$

$$k = \frac{[PO_2]}{[P] \times [O_2]} \qquad \text{Eq. 3.14}$$

P, O_2, and PO_2 denote polymer, oxygen, and oxide, respectively. The bracket denotes the concentration of each species. k is the reaction rate constant [95].

Since the matrix is a solid polymer, the concentration [P] can be assumed constant. Hence, according to Eq. 3.14, $[PO_2]$ is linearly proportional to $[O_2]$. Therefore, it is proper to use Eq. 3.3 to represent both of the concentration trends of oxide and oxygen. Finally, the V_d in Eq. 3.12 can be determined by Eq. 3.15, which is based on the integration of Eq. 3.3.

$$V_d = \frac{\int_0^L c(x,t)\,dx}{c_0 \times L}$$
$$= 1 + \frac{4}{\pi^2} \sum_{j=0}^{n} \left(\frac{1}{(2j+1)^2} \left[\cos\left((2j+1)\pi\right) - 1 \right] \times \exp\left(- \left[\frac{(2j+1)\pi}{L} \right]^2 D\,t \right) \right) \qquad \text{Eq. 3.15}$$

Since V_d is obtained, the EAB ratio (δ) should be calculated by plugging Eq. 3.15 into Eq. 3.12. However, because the degraded part caused by diffusion kinetics is not uniformly

distributed along the radius direction of cable insulation, which does not completely conform to the concept of Dichotomy Model. Besides, oxidation reaction cannot represent all the degradation reactions in the polymer bulk. Therefore, one empirical factor β is required to modify Eq. 3.12. Finally, Eq. 3.16 is obtained.

$$\frac{EAB_{II}}{EAB_{I}} = \delta \approx \left(1 - \left\{\frac{\int_0^L c(x,t)dx}{c_0 \times L}\right\}^{\frac{1}{3}}\right)\beta \qquad \text{Eq. 3.16}$$

where β can be obtained by curve-fitting the EAB data from experiments.

3.2.4 Dichotomy Model - Reaction Control

For the horizontal segment plotted by the dashed line in Figure 3.1, the drop-off rate is negligible and assumed zero. As for the curve, the behavior of the drop off can be modeled by a function of drop-off rate ν. From Arrhenius equation, this drop-off rate ν can be represented by Eq. 3.17.

$$\nu = \nu_0 \exp\left(\frac{-\Delta G}{RT}\right) \qquad \text{Eq. 3.17}$$

or

$$\ln(\nu) = -\left(\frac{\Delta G}{R}\right)\left(\frac{1}{T}\right) + \ln(\nu_0) \qquad \text{Eq. 3.18}$$

ν_0: attempt frequency = [/time], which is assumed constant in this research

R: ideal gas constant = 8.314 J/mol-K

T: absolute temperature = [K]

ΔG: the energy barrier of the reaction = [J/mol], which could be assumed constant if the temperature range is small.

In reaction control, EAB ratio (δ) can be calculated by plugging Eq. 3.4 into Eq. 3.12, shown by Eq. 3.19.

$$\text{EAB ratio} = \frac{\text{EAB}_{\text{II}}}{\text{EAB}_{\text{I}}} = \delta \cong 1 - [1 - \exp(-\nu \times t)]^{1/3} \qquad \text{Eq. 3.19}$$

Due to the horizontal segment of the dashed line in Figure 3.1, t in Eq. 3.4 and Eq. 3.19 can be replaced by ($t-\tau_0$), shown by Eq. 3.20. This term ($t-\tau_0$) must be equal or larger than zero. The τ_0 stands for the length of the horizontal dash line in Figure 3.1. In other words, the drop off of the EAB begins after the end of τ_0. When there is no incubation time, τ_0 is zero. Eq. 3.19 and Eq. 3.20 are the same.

$$\text{EAB ratio} = \frac{\text{EAB}_{\text{II}}}{\text{EAB}_{\text{I}}} = \delta \cong 1 - \left[1 - e^{-\nu(t-\tau_0)}\right]^{1/3} \qquad \text{Eq. 3.20}$$

3.2.5 Validation - Diffusion Control

The discrete patterns in Figure 3.6 are the experimental data measured by FTIR representing relative oxide concentration at 135℃ for 0~400 hours [34]. The continuous lines are plotted according to Eq. 3.3 with c_0, τ_0, L, n, and D at 5, 0, 2mm, 100, and 2.4E-13m^2/s, respectively. Modeled curves fit experimental data well, which means Eq. 3.3 is valid.

The discrete pattern in Figure 3.7 is experimental data [34] which is compared with the modeled curves plotted according to Eq. 3.16. Before the empirical factor β is considered (β=1), the modeled curve fits the long-term experimental data better. This is because, for long-term aging, the oxidation profile becomes more uniform. As for the short-term δ, because the origin of Eq. 3.16 is based on uniform degradation, empirical factor β should be applied. β = 0.75 can fit both the short- and long-term experimental data.

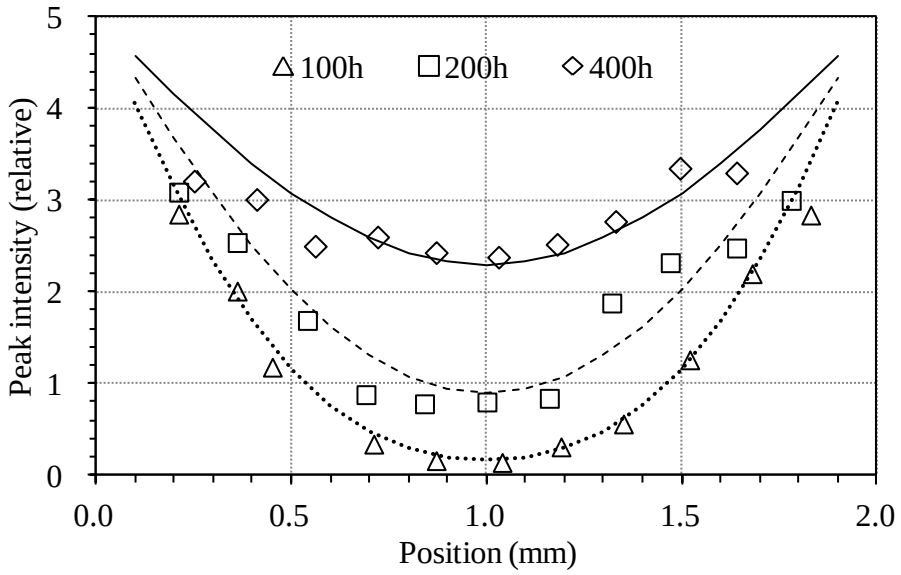

Figure 3.6 Experimental (discrete patterns) and modeled (continuous lines) oxidation profiles.

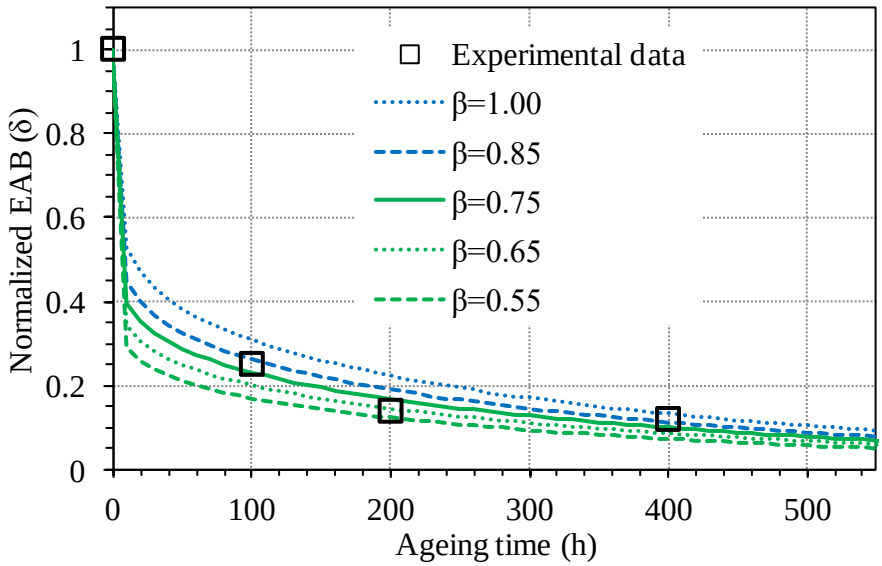

Figure 3.7 Experimental (discrete pattern) and modeled (continuous lines) EAB at 135℃.

3.2.6 Validation - Reaction Control

3.2.6.1 XLPE in Thermal Degradation

The experimental data is from the white core samples of the FR-XLPE made by company B discussed in a JNES report [20]. The EAB before aging is 558.6%. Eq. 3.20 with parameters listed in Table 3.1 is plotted by the continuous lines to model the experimental data plotted by the discrete patterns in Figure 3.8. The XLPE samples in Figure 3.8 are subjected to thermal aging with no radiation.

Table 3.1 Modeled parameters of FR-XLPE (thermal aging)

Dose rate (Gy/h)	Temperature(℃)	τ_0 (h)	$\nu \times 1E5$ (1/h)
0	100	21,000	7.5
0	110	11,000	13
0	120	5,800	33

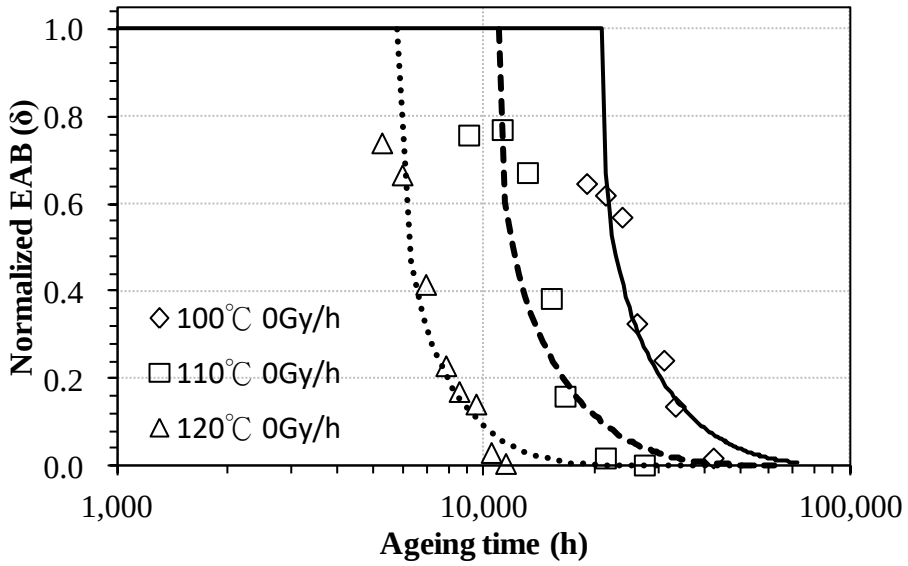

Figure 3.8 Normalized EAB of FR-XLPE vs. aging time (thermal)

The modeled drop-off rates at different aging temperatures in Figure 3.8 are plotted in Figure 3.9. The same data points are further plotted in the form of Eq. 3.18 and shown by the discrete pattern in Figure 3.10. After linear fitting is applied, the slope is (-10.841). Corresponding to Eq. 3.18, the ΔG can be calculated by (-slope × R), which is 10.841*8.314 ≈ 90 KJ/mol.

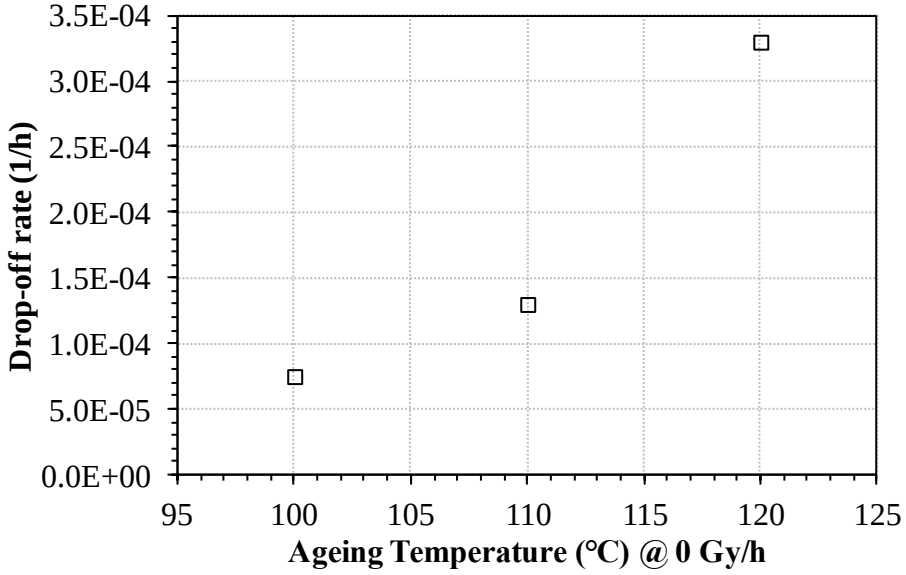

Figure 3.9 Drop-off rate vs. aging temperature of FR-XLPE (thermal)

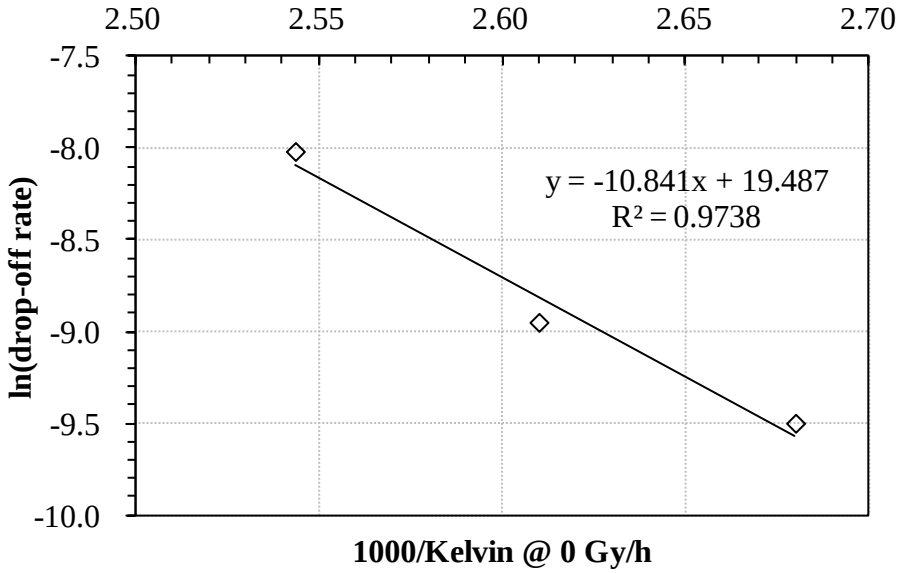

Figure 3.10 Arrhenius plot of FR-XLPE in thermal aging

The incubation time in Figure 3.8 is the length of the horizontal segment determined by the

intersection of δ = 1 and Eq. 3.20. Each value at its aging temperature is illustrated in Figure 3.11.

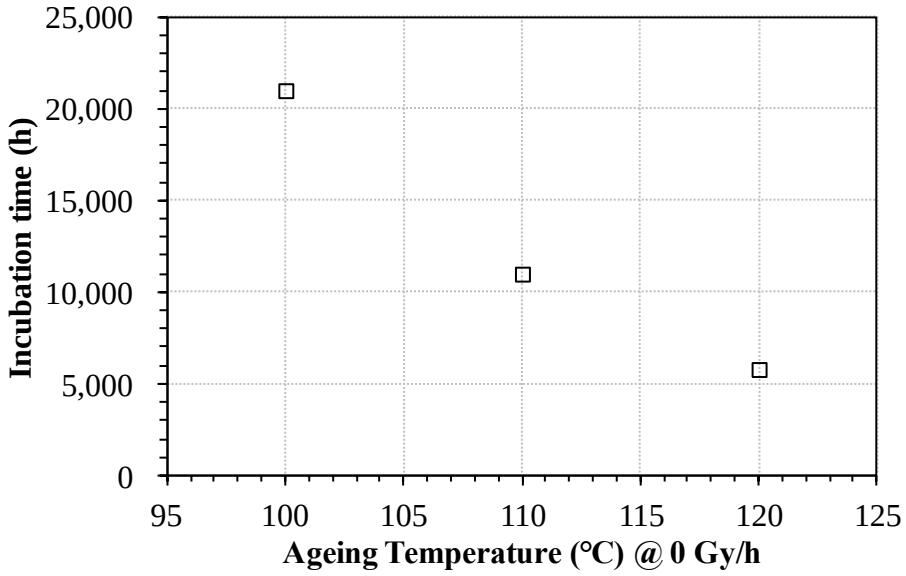

Figure 3.11 Modeled incubation time vs. aging temperature in thermal aging (FR-XLPE)

3.2.6.2 XLPE in Radiation Degradation

When the same XLPE samples are exposed to heat and radiation simultaneously, Eq. 3.20 with parameters listed in Table 3.2 is plotted by the continuous lines to model the experimental data plotted by the discrete patterns in Figure 3.12. Set 1 and set 2 in Figure 3.12 are exactly the same except their x-axes. The linear x-axis can more intuitively express the trends of the drop-off rates corresponding to the change of aging temperature and dose rate. The logarithmic x-axis is plotted for the comparison of this research to the figures in the

report [20] providing the experimental data.

Table 3.2 Modeled parameters of FR-XLPE (simultaneous aging)

Dose rate (Gy/h)	Temperature(℃)	τ_0 (h)	ν×1E5 (1/h)
3	80	18,500	6.8
3	90	12,500	9
3	100	10,500	15.8
17	80	6,700	13
17	90	5,700	22
17	100	4,900	36
98	80	2,200	26
98	90	2,100	40
98	100	1,900	68

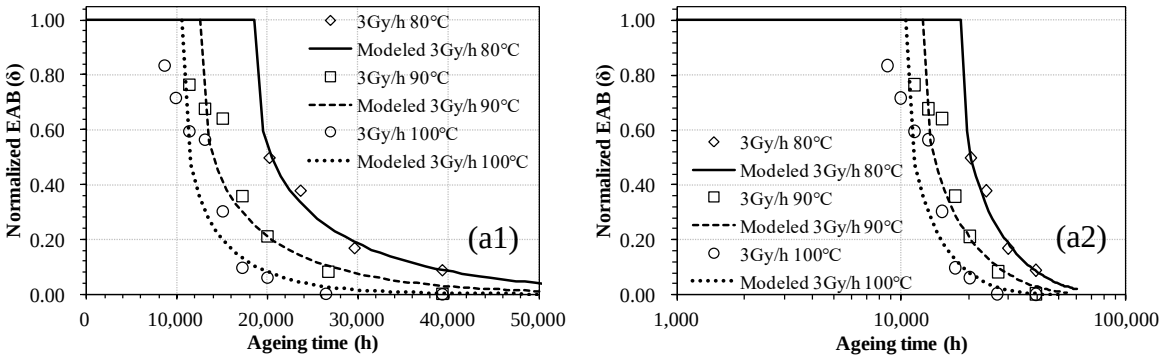

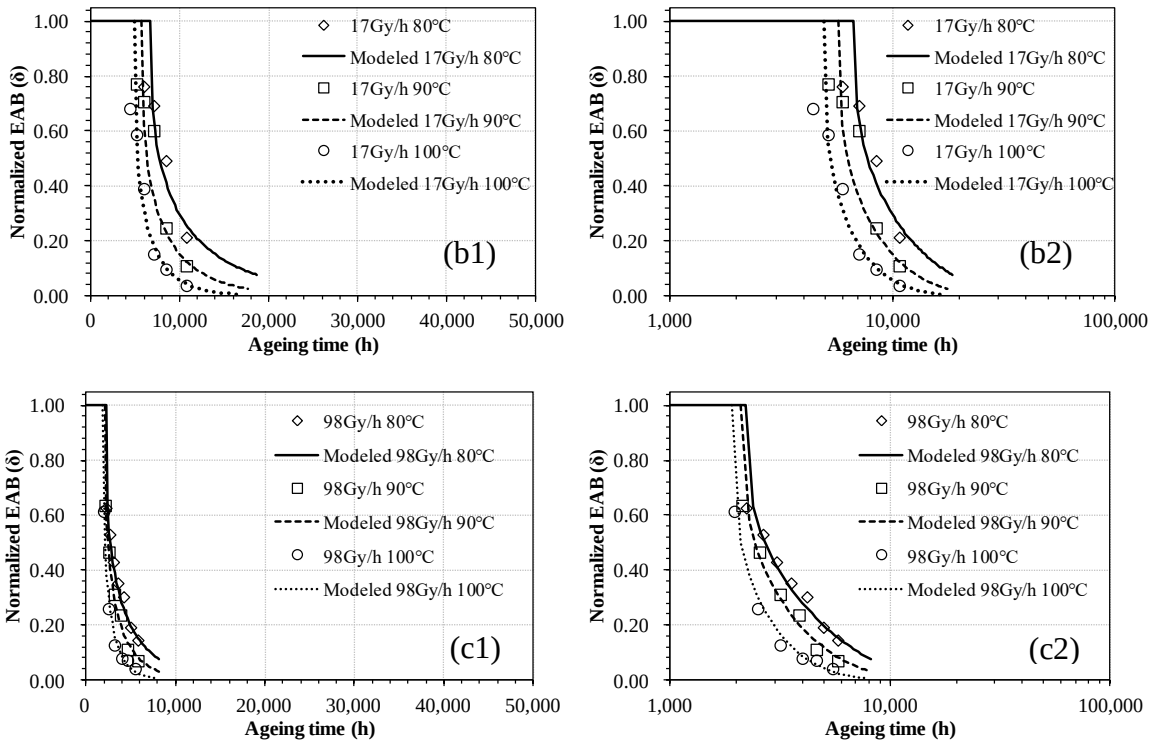

Figure 3.12 Normalized EAB of FR-XLPE vs. aging time with radiation

The relations among the drop-off rate, incubation time, aging temperature, and dose rate are plotted in Figure 3.13, Figure 3.14, Figure 3.15, and Figure 3.16. When all the data points along their x-axis directions are connected by straight lines, Figure 3.17 and Figure 3.18 can be plotted.

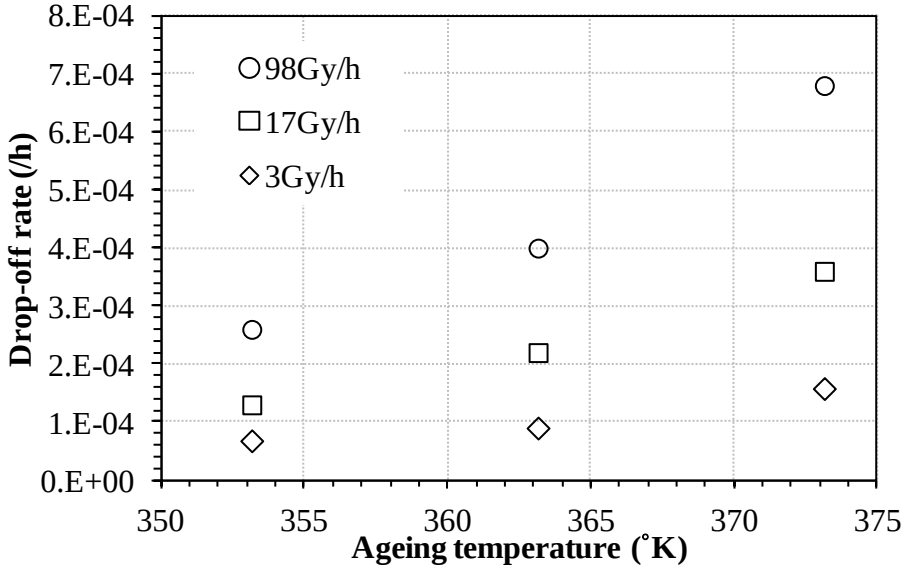

Figure 3.13 Modeled drop-off rate vs. aging temperature (FR-XLPE)

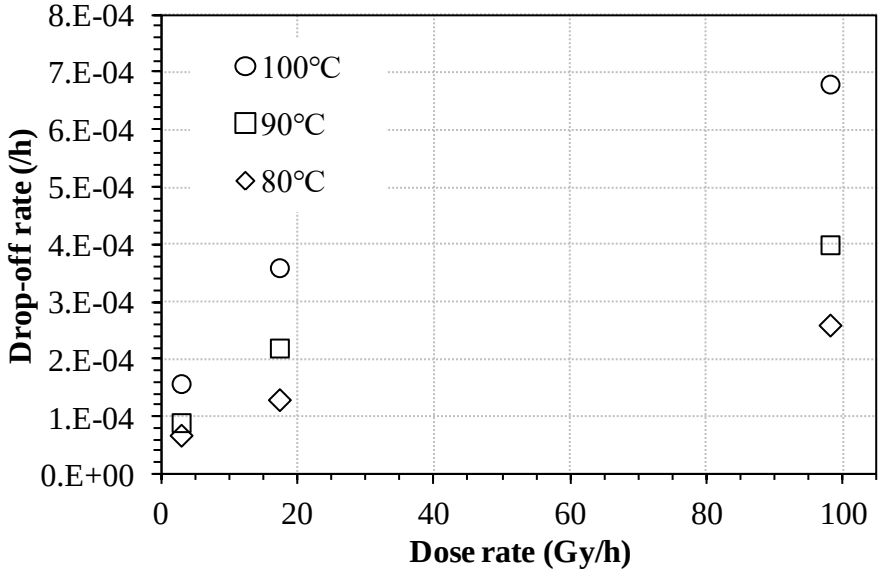

Figure 3.14 Modeled drop-off rate vs. dose rate (FR-XLPE)

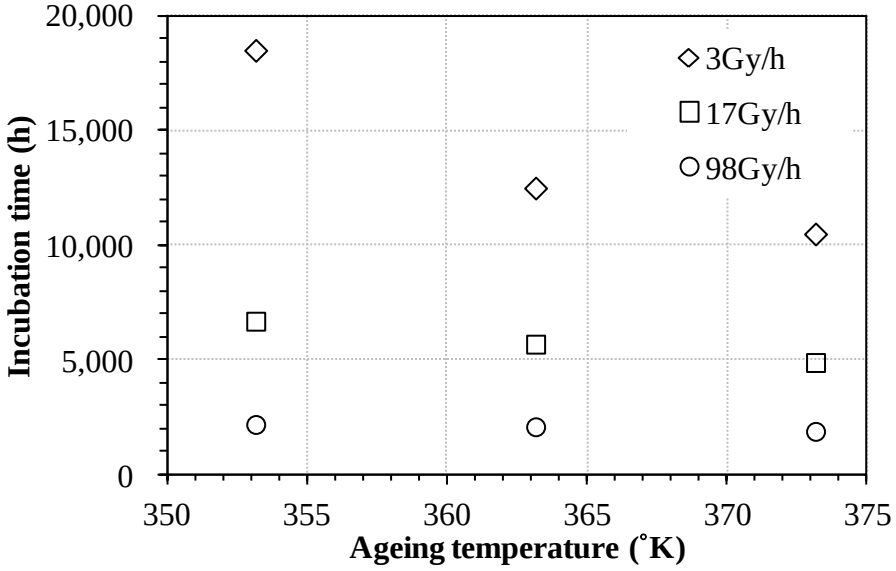

Figure 3.15 Modeled incubation time vs. aging temperature (FR-XLPE)

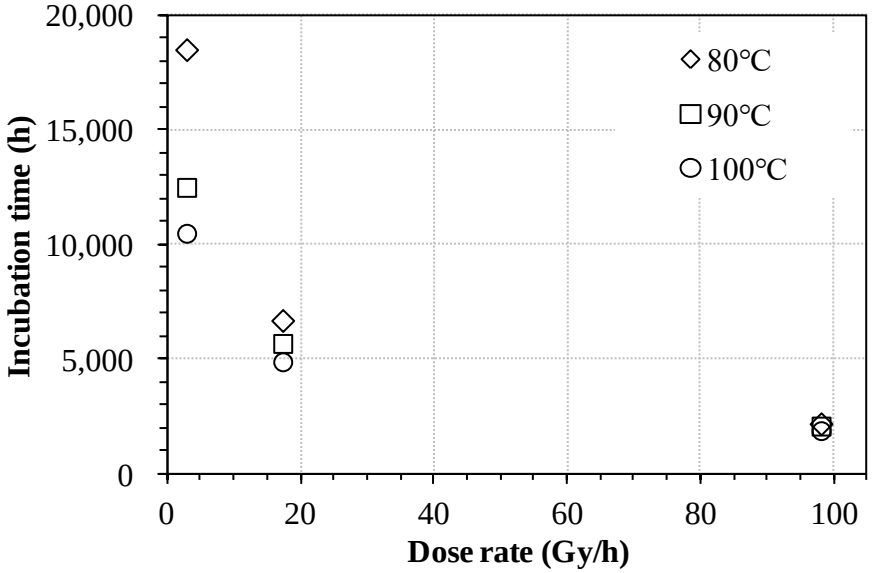

Figure 3.16 Modeled incubation time vs. dose rate (FR-XLPE)

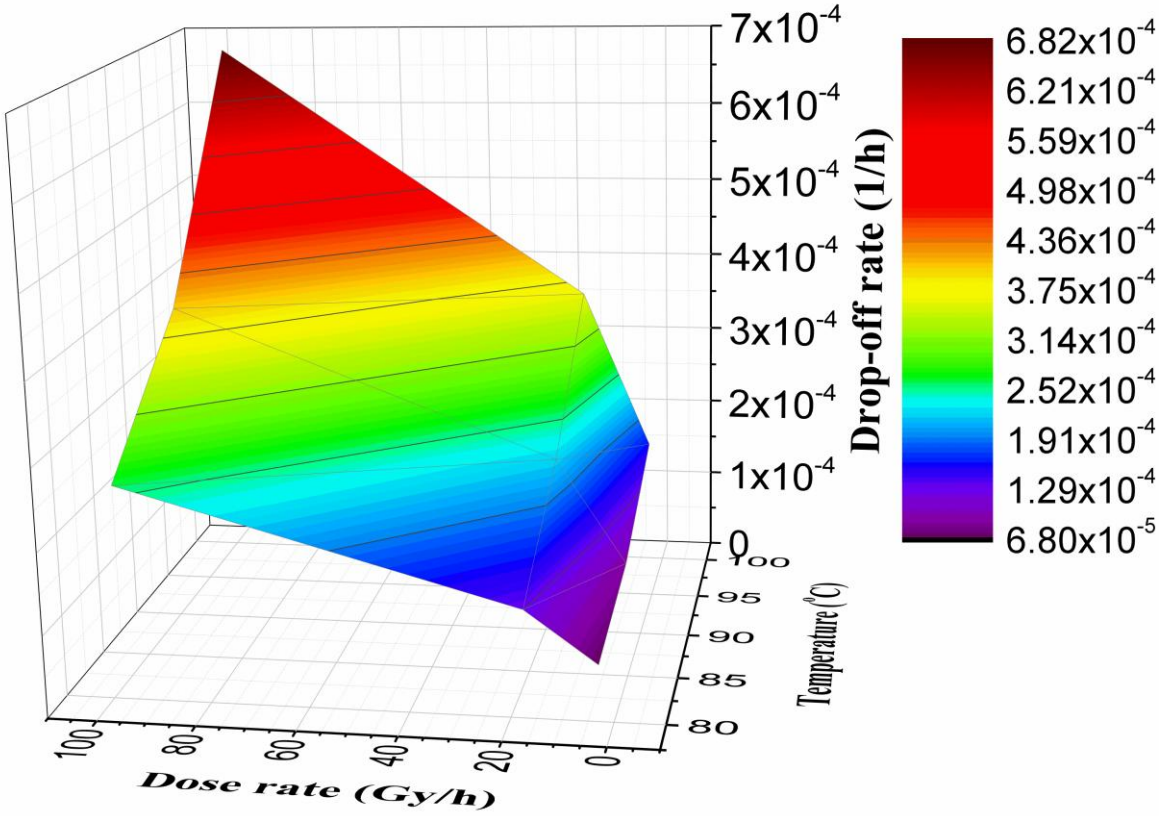

Figure 3.17 Modeled drop-off rate vs. aging temperature and dose rate of FR-XLPE

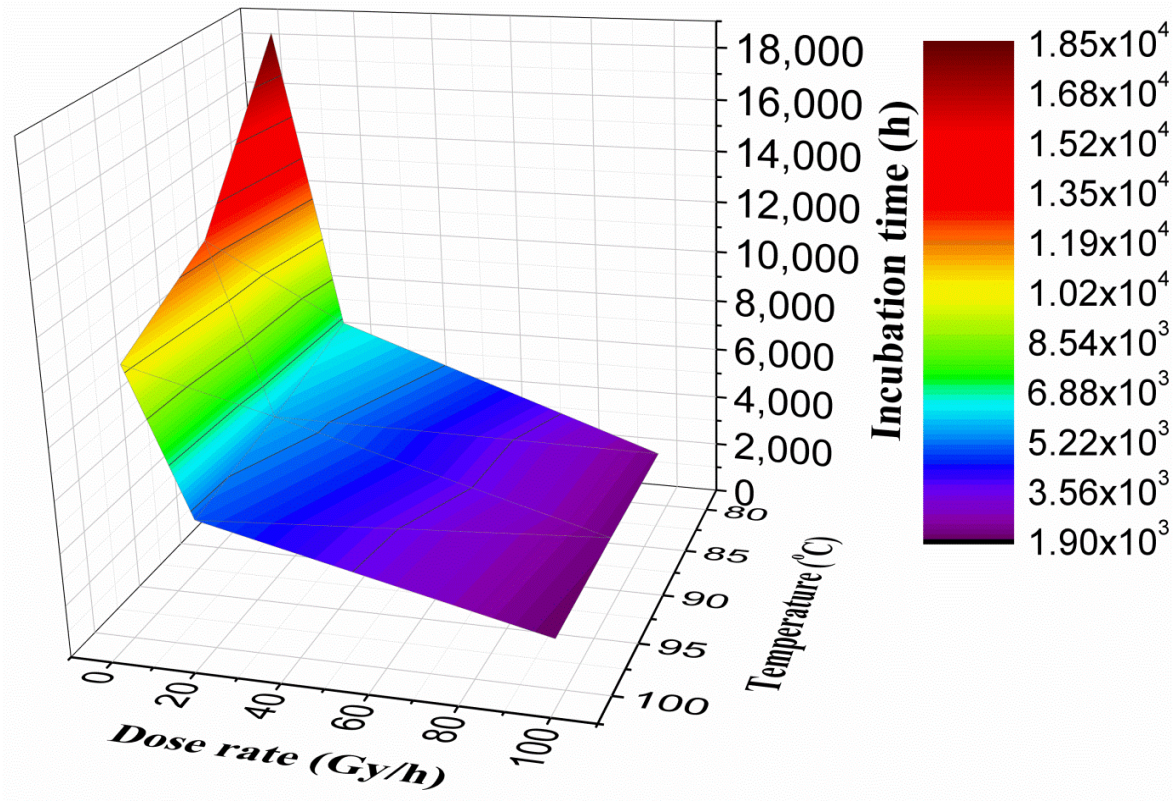

Figure 3.18 Modeled incubation time vs. aging temperature and dose rate of FR-XLPE

3.2.6.3 EPR in Thermal Degradation

The experimental data is from the white core samples of the FR-EPR made by company A discussed in a JNES report [20]. The EAB before aging is 415.8%. Eq. 3.20 with parameters listed in Table 3.3 is plotted by the continuous lines to model the experimental data plotted by the discrete patterns in Figure 3.19. The EPR samples in Figure 3.19 are subjected to thermal aging with no radiation.

Table 3.3 Modeled parameters of FR-EPR (thermal aging)

Dose rate (Gy/hour)	Temperature (℃)	τ_0 (h)	$\nu*10^4$ (1/h)
0	100	4,700	6.5
	110	2,600	18
	120	950	30

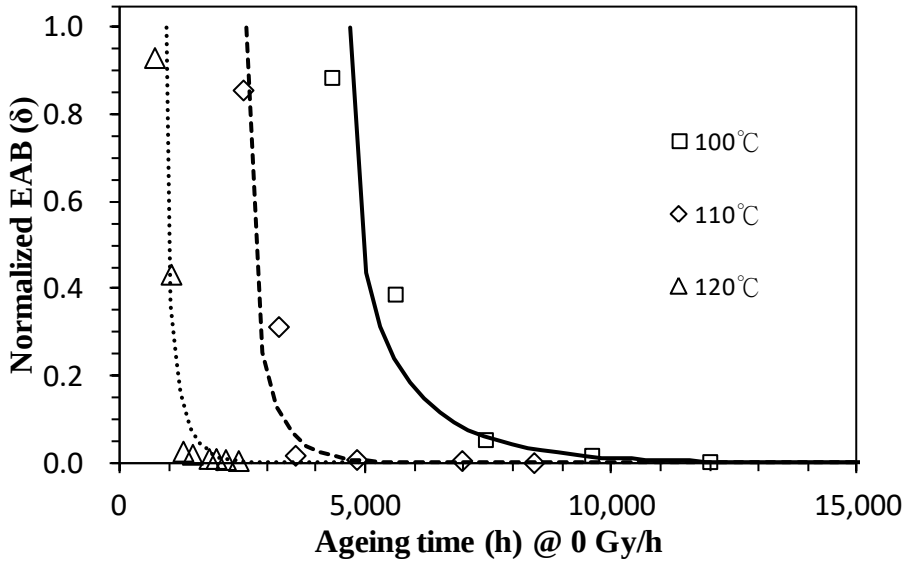

Figure 3.19 Normalized EAB of FR-EPR vs. aging time (thermal)

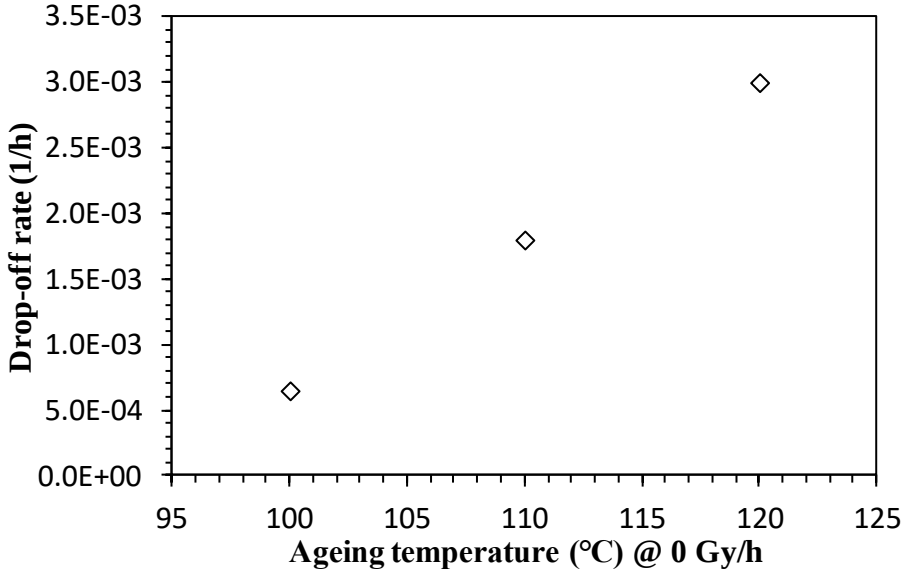

Figure 3.20 Drop-off rate vs. aging temperature of FR-EPR (thermal)

The modeled drop-off rates at different aging temperatures in Figure 3.19 are plotted in Figure 3.20. The same data points are further plotted in the form of Eq. 3.18 and shown by the discrete pattern in Figure 3.21. After linear fitting is applied, the slope is (-11.248). Corresponding to Eq. 3.18, the ΔG can be calculated by (-slope × R), which is -11.248*8.314 ≈ 94 KJ/mol.

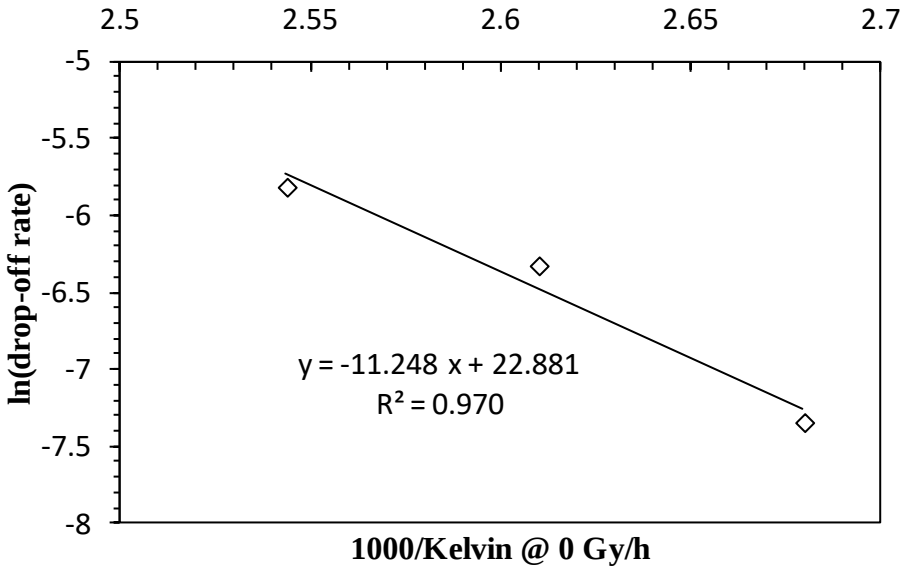

Figure 3.21 Arrhenius plot of FR-EPR

The incubation time in Figure 3.19 is the length of the horizontal segment determined by the intersection of $\delta = 1$ and Eq. 3.20. Each value at its aging temperature is illustrated in Figure 3.22.

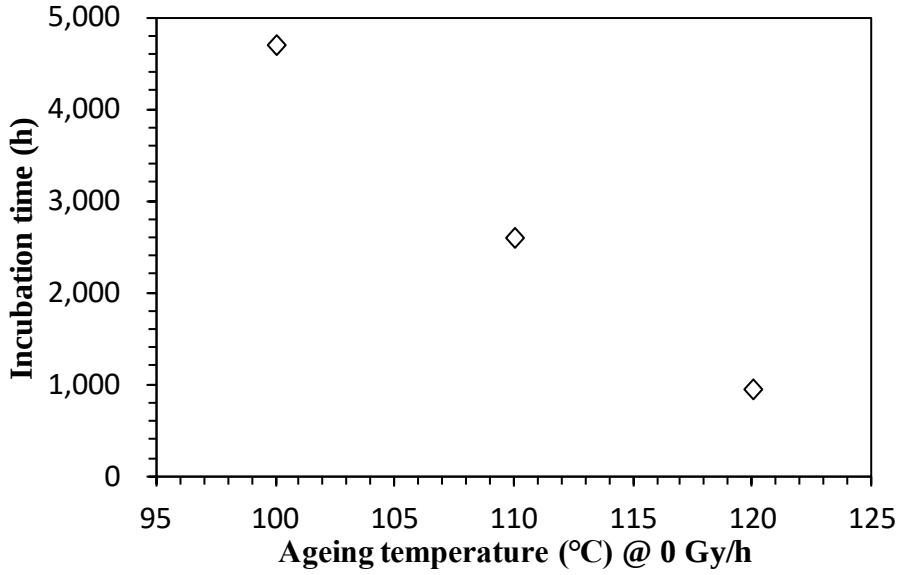

Figure 3.22 Modeled incubation time vs. aging temperature (FR-EPR)

3.2.6.4 EPR in Radiation Degradation

When the same EPR samples are exposed to heat and radiation simultaneously, Eq. 3.20 with parameters listed in Table 3.4 is plotted by the continuous lines to model the experimental data plotted by the discrete patterns in Figure 3.23.

Table 3.4 Modeled parameters of FR-EPR (simultaneous aging)

Dose rate (Gy/hour)	Temperature (°C)	τ_0 (h)	$\nu*10^4$ (1/h)
3	80	9,350	2.6
	90	7,900	4.0

	100	5,900	6.5
18	80	4,700	7
	90	4,100	12
	100	3,200	18
99	80	2,800	4
	90	2,150	6
	100	1,900	10

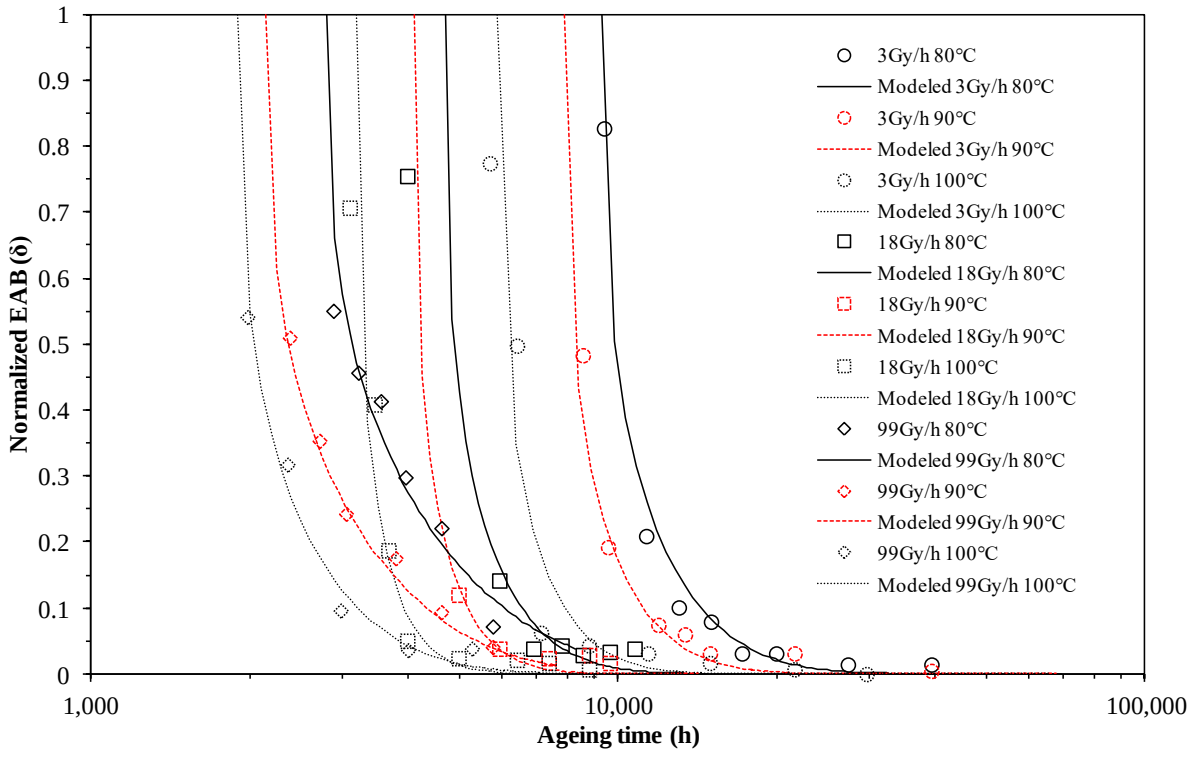

Figure 3.23 Normalized EAB of FR-EPR vs. aging time with radiation

The relations among the drop-off rate, incubation time, aging temperature, and dose rate are plotted in Figure 3.24, Figure 3.25, Figure 3.26, and Figure 3.27. When all the data points along their x-axis directions are connected by straight lines, Figure 3.28 and Figure 3.29 can be plotted.

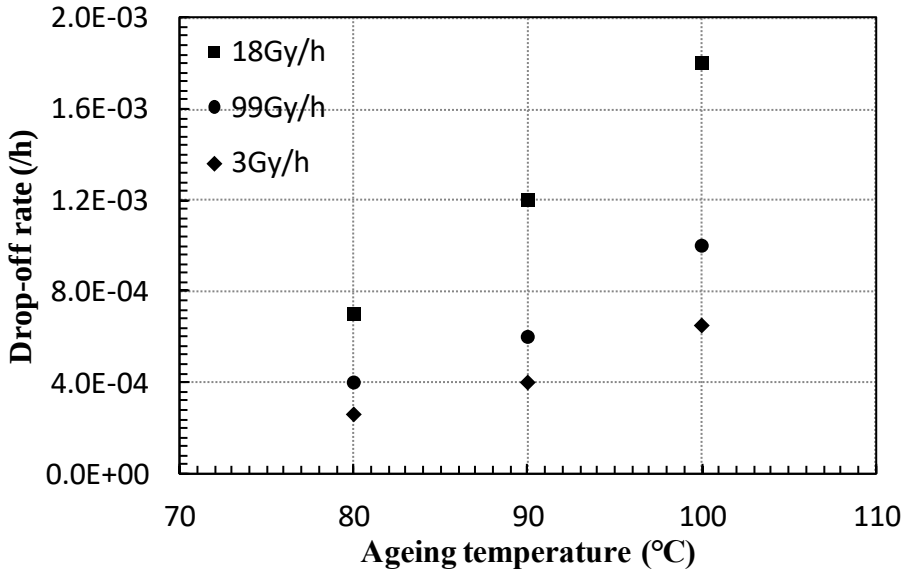

Figure 3.24 Modeled drop-off rate vs. aging temperature (FR-EPR)

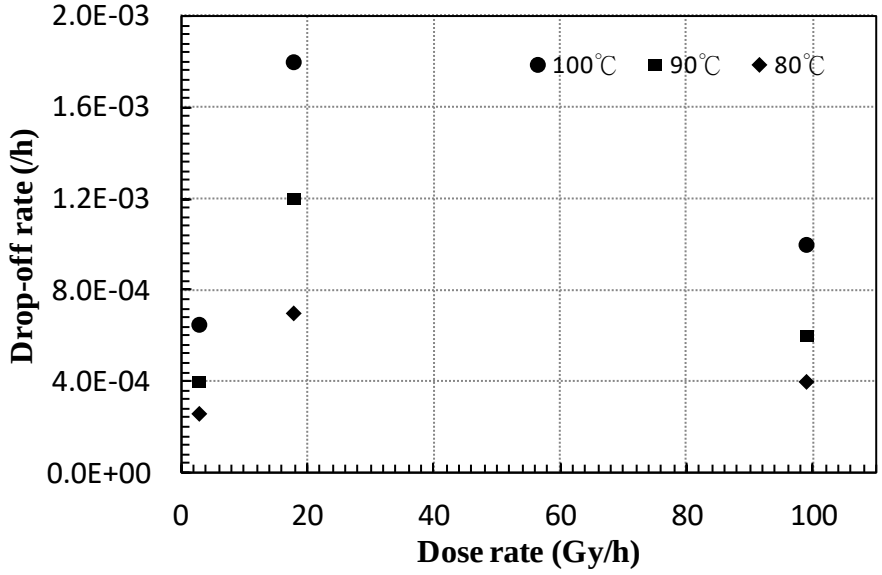

Figure 3.25 Modeled drop-off rate vs. dose rate (FR-EPR)

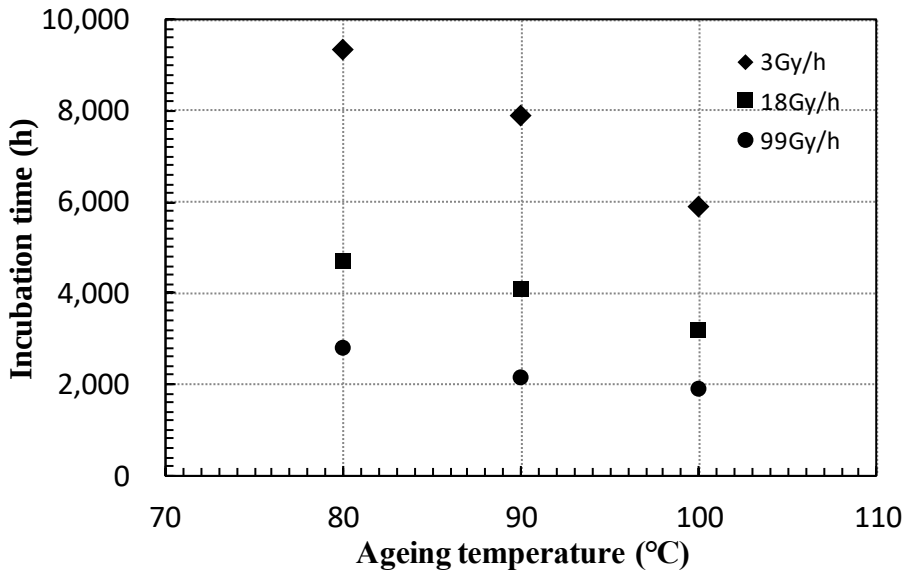

Figure 3.26 Modeled incubation time vs. aging temperature (FR-EPR)

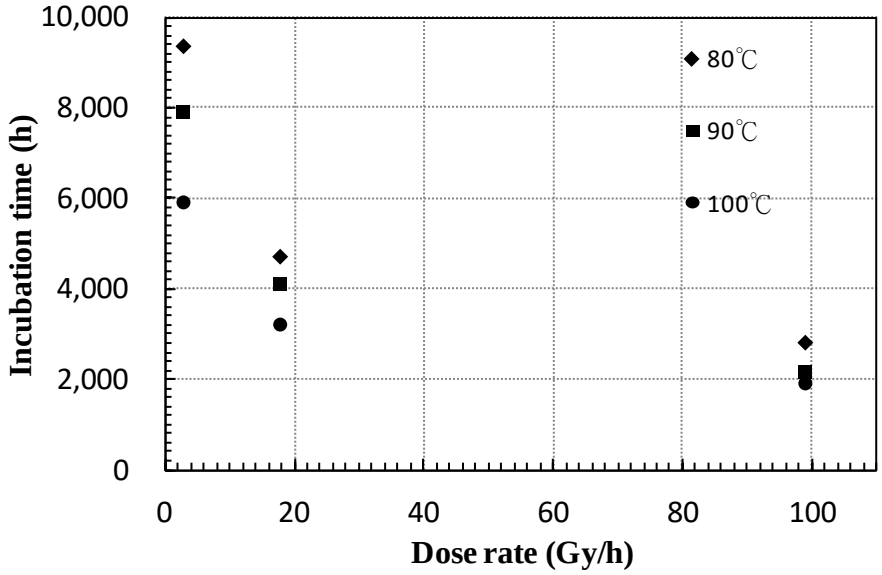

Figure 3.27 Modeled incubation time vs. dose rate (FR-EPR)

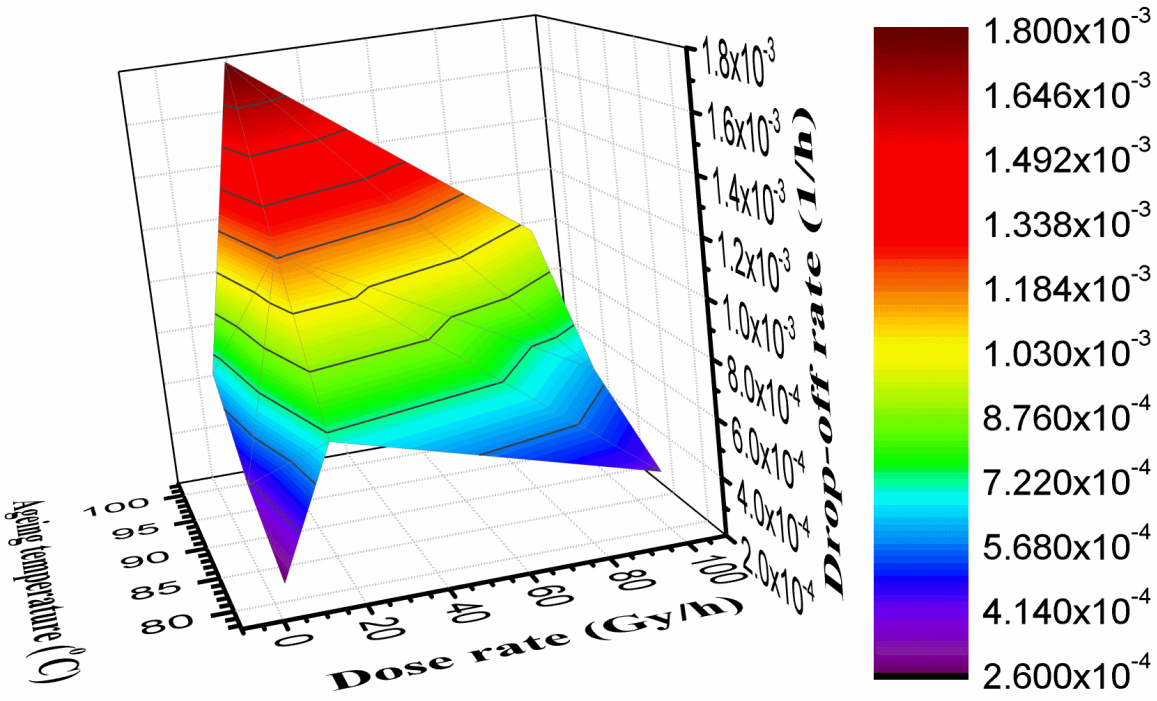

Figure 3.28 Modeled drop-off rate vs. aging temperature and dose rate of FR-EPR

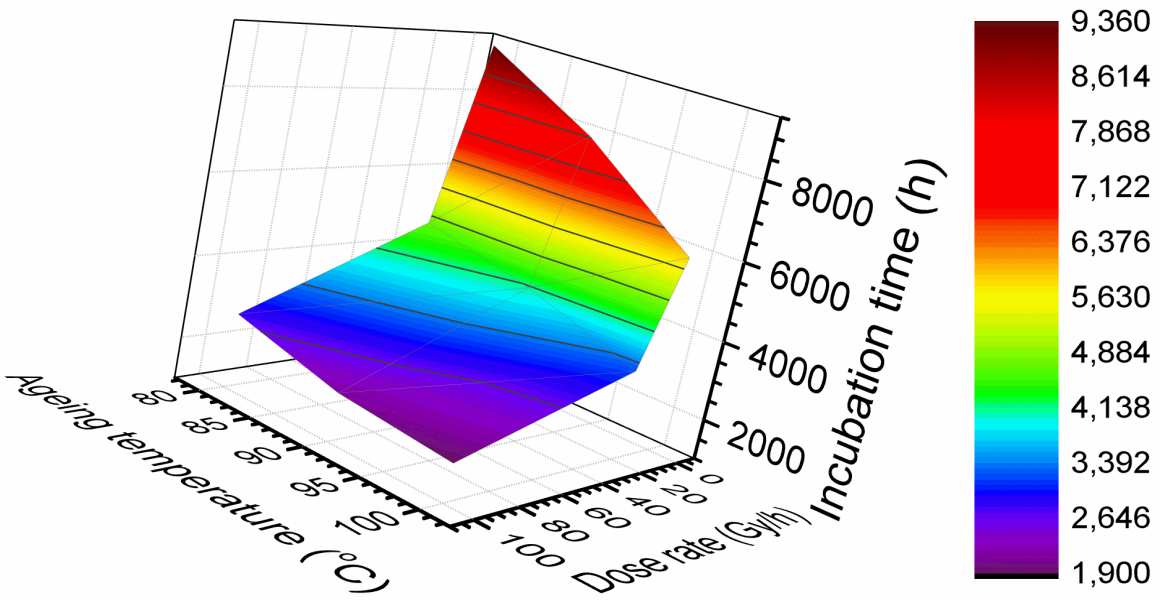

Figure 3.29 Modeled incubation time vs. aging temperature and dose rate of FR-EPR

3.2.6.5 SIR in Thermal Degradation

The experimental data is from the SIR samples made by company A discussed in a JNES report [20]. The EAB before aging for black, white, and red core samples are 352.8, 356.8, and 346.5%, respectively. Eq. 3.20 with parameters listed in Table 3.5 is plotted by the continuous lines to model the experimental data plotted by the discrete patterns in Figure 3.30. The SIR samples in Figure 3.30 are subjected to thermal aging with no radiation. All the continuous lines in Figure 3.30 are organized in Figure 3.31 for the comparison of incubation time and drop-off rate at different aging temperatures.

Table 3.5 Modeled parameters of the SIR (thermal aging)

Dose rate (Gy/hour)	Temperature (°C)	τ_0 (h)	$\nu*10^5$ (1/h)
0	135	8,500	8
	155	4,300	12
	175	2,000	22

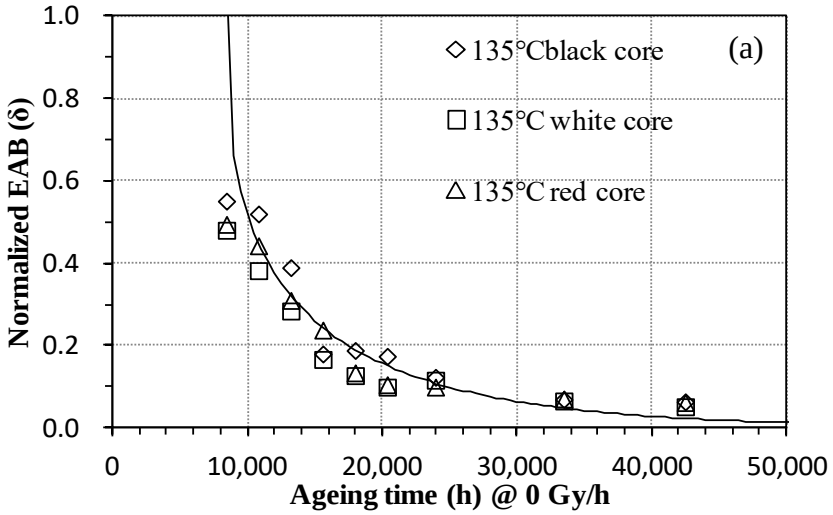

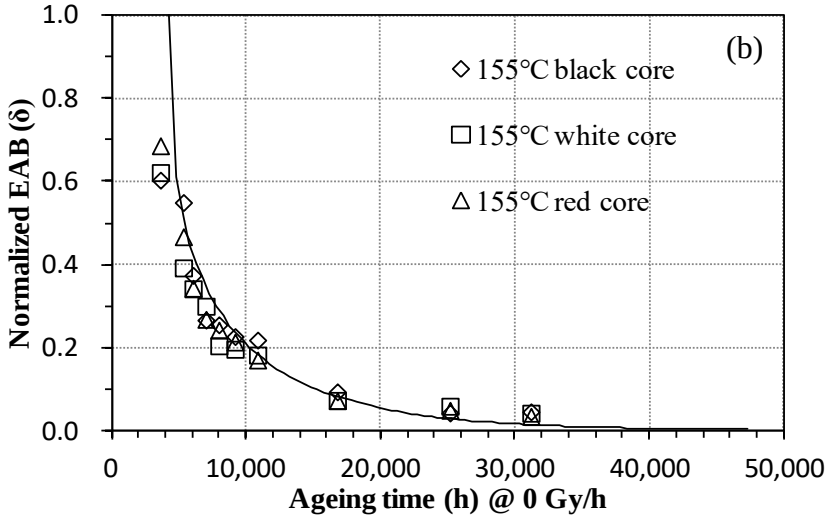

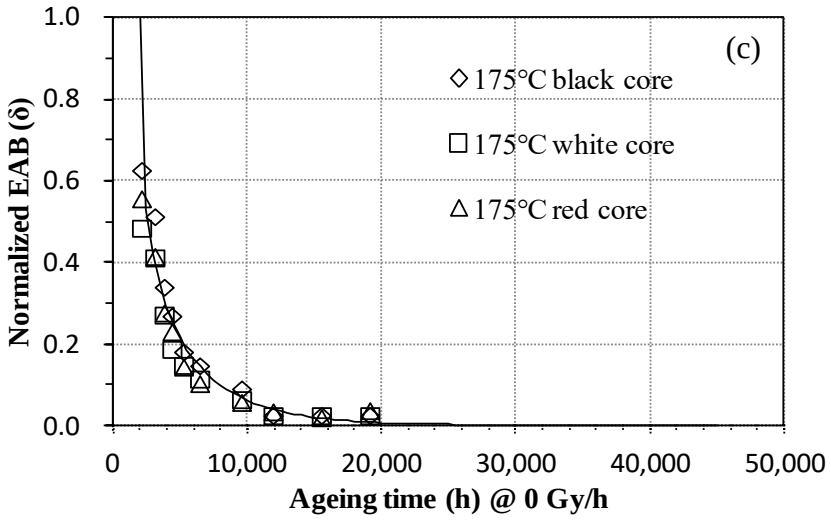

Figure 3.30 Normalized EAB vs. aging time of SIR (thermal)

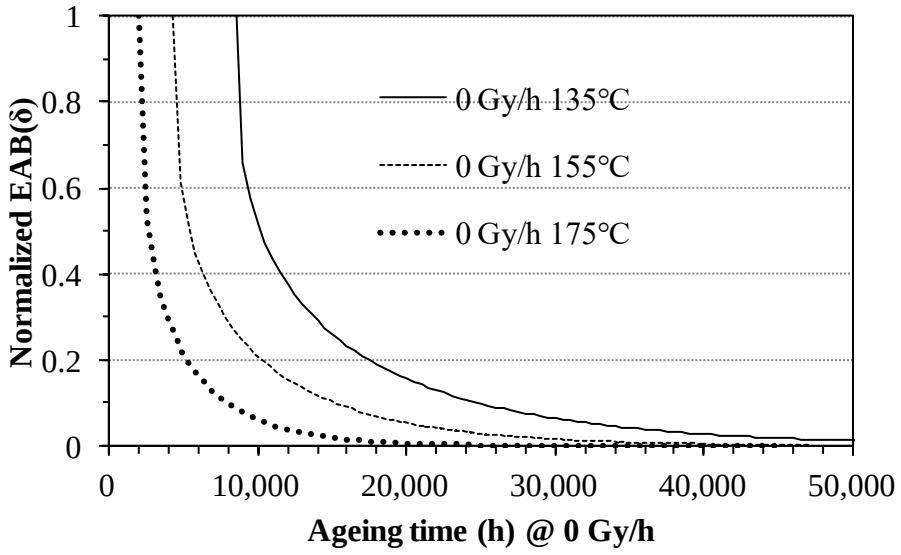

Figure 3.31 Comparison of modeled EAB of SIR vs. aging time (modeled by Eq. 3.20)

The modeled drop-off rates at different aging temperatures in Figure 3.30 are plotted in Figure 3.32. The same data points are further plotted in the form of Eq. 3.18 and shown by the

discrete pattern in Figure 3.33. After linear fitting is applied, the slope is (-4.608). Corresponding to Eq. 3.18, the ΔG can be calculated by (-slope × R), which is 4.608*8.314 ≈ 38 KJ/mol.

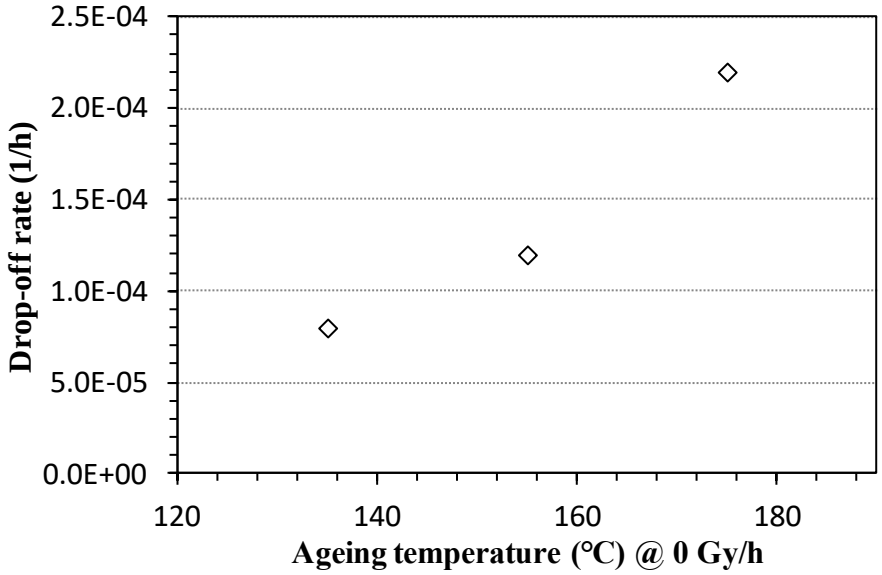

Figure 3.32 Drop-off rate vs. aging temperature of SIR (thermal)

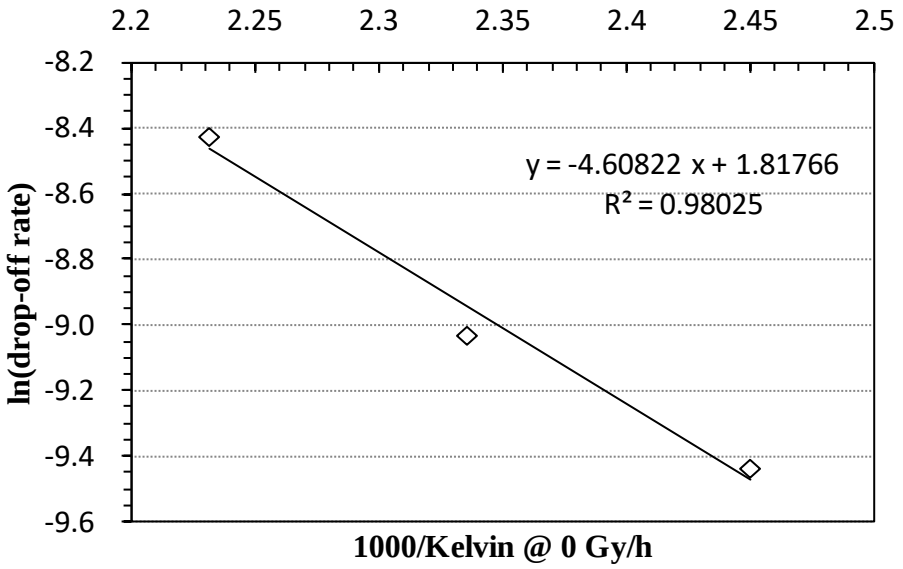

Figure 3.33 Arrhenius plot of SIR

The incubation time in Figure 3.30 is the length of the horizontal segment determined by the intersection of $\delta = 1$ and Eq. 3.20. Each value at its aging temperature is illustrated in Figure 3.34.

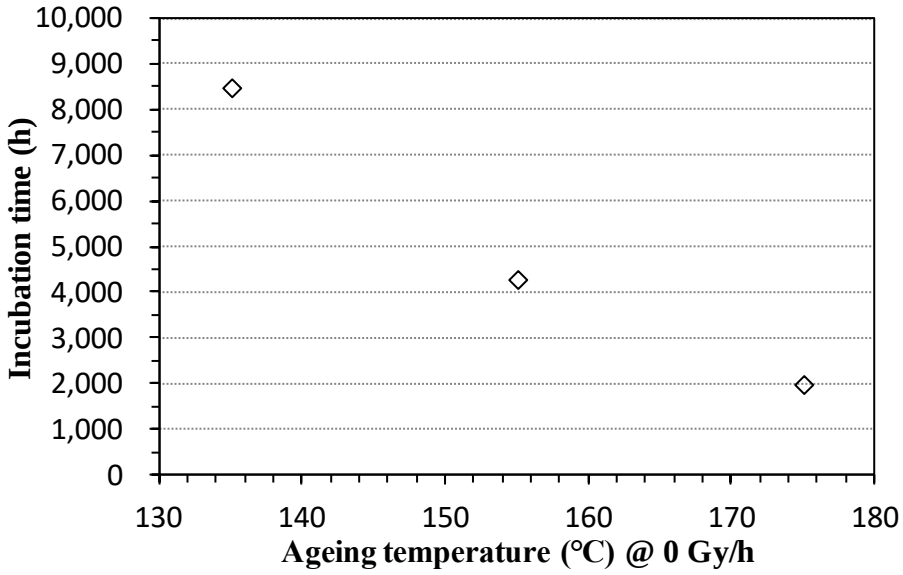

Figure 3.34 Modeled incubation time vs. aging temperature (SIR)

Besides the examples of the thermal degradation, SIR subject to heat and radiation is discussed in the next section by both deterministic and probabilistic approaches.

3.2.7 Probabilistic Model

Eq. 3.20 is a deterministic model predicting the normalized EAB as a function of time. However, experimental data shows uncertainty with respect to the predicted value. Bayesian parameter estimation, Eq. 3.21, can be used to calculate the uncertainty of the drop-off rate. It allows one to consider prior information about the parameters of a model along with the likelihood function which presents the probability of observed data corresponding to the model.

$$\Pr(\theta \mid \text{Data}) = \frac{\Pr(\text{Data} \mid \theta)\ \Pr(\theta)}{\int \Pr(\text{Data} \mid \theta)\ \Pr(\theta) d\theta} \qquad \text{Eq. 3.21}$$

The measured data in this research are aging time (t_i) and normalized EAB (δ_i), such as the discrete data points in Figure 3.30. Estimating the probability distribution of the parameters θ by the given observed experimental data is the goal. If the data (t_i, δ_i) can be represented by the regression equation Eq. 3.20, it is reasonable to assume that the experimental data δ_i is normally distributed around the regression line. That is:

$$\delta \sim \mathcal{N}(\mu_{\boldsymbol{\delta}}, \sigma^2) \qquad \text{Eq. 3.22}$$

The mean $\mu_{\boldsymbol{\delta}}$ follows the regression function Eq. 3.20 and can be represented by Eq. 3.23.

$$\mu_{\boldsymbol{\delta}} = 1 - (1 - e^{-\nu t})^{1/3} \qquad \text{Eq. 3.23}$$

The unknown parameter (θ) of the model consists of the regression parameter ν and the variation of the fitted model σ^2. The likelihood function then can be represented by Eq. 3.24.

$$\Pr(\delta|\mu_\delta,\sigma^2) = \frac{1}{\sqrt{2\pi\sigma^2}}\exp\left(-\frac{(\delta_i-\mu_\delta)^2}{2\sigma^2}\right) \quad \text{Eq. 3.24}$$

Based on Eq. 3.23, the likelihood function Eq. 3.24 can be rewritten into Eq. 3.25.

$$\Pr(\delta|t,\nu,\sigma^2) = \frac{1}{\sqrt{2\pi\sigma^2}}\exp\left(-\frac{\left(\delta_i-(1-[1-\exp(-\nu\times t_i)]^{\frac{1}{3}})\right)^2}{2\sigma^2}\right) \quad \text{Eq. 3.25}$$

This approach is used to determine the probability of the drop-off rate of SIR subject to heat and radiation in the next section.

3.2.7.1 Validation - SIR in Radiation Degradation

The experimental data is from the SIR samples made by company A discussed in a JNES report [20]. The EAB before aging for black, white, and red core samples are 352.8, 356.8, and 346.5%, respectively. The samples are exposed to heat and radiation simultaneously. In Figure 3.35, Figure 3.39, and Figure 3.40, the discrete patterns are the experimental data while the continuous solid, dashed, and dotted lines are plotted according to Eq. 3.20 with the parameters determined by Bayesian parameter estimation. The parameters are organized in Table 3.6. How to determine these parameters will be demonstrated in this section.

Table 3.6 Modeled parameters of SIR by a probabilistic approach (simultaneous aging)

Dose rate	Temperature	τ_0	Mean of ν	Percentile of ν					SD of ν
(Gy/h)	(℃)	(h)	(1/h)	2.5%	25%	50%	75%	97.5%	
3	100	7,000	1.479E-05	1.050E-05	1.319E-05	1.440E-05	1.585E-05	2.118E-05	3.231E-06
3	115	5,800	2.015E-05	1.766E-05	1.937E-05	2.010E-05	2.087E-05	2.290E-05	1.321E-06
3	135	4,300	4.305E-05	3.742E-05	4.151E-05	4.277E-05	4.421E-05	5.033E-05	3.103E-06
18	100	2,100	7.872E-05	7.084E-05	7.630E-05	7.859E-05	8.099E-05	8.772E-05	4.112E-06
18	115	1,700	1.009E-04	9.168E-05	9.801E-05	1.007E-04	1.037E-04	1.108E-04	4.829e-06
18	135	1,000	1.603E-04	1.478E-04	1.562E-04	1.602E-04	1.643E-04	1.738E-04	6.546e-06
104	100	700	4.155E-04	3.295E-04	3.830E-04	4.072E-04	4.390E-04	5.499E-04	5.342e-05
104	115	550	5.104E-04	4.035E-04	4.762E-04	5.070E-04	5.413E-04	6.411E-04	5.697e-05
104	135	300	5.429E-04	4.602E-04	5.167E-04	5.396E-04	5.648E-04	6.525E-04	4.423e-05

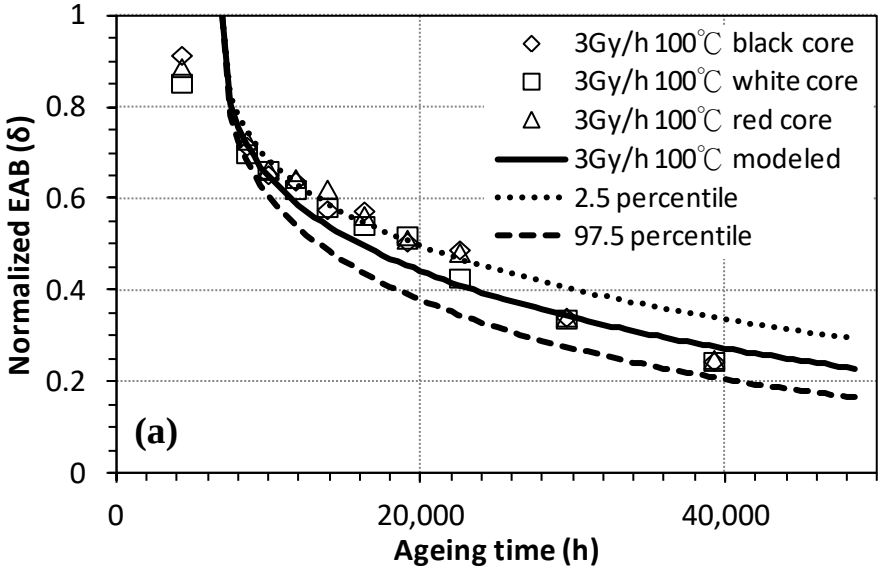
Normalized EAB (δ)
1
0.8
0.6
0.4
0.2
0
0
20,000
40,000
Ageing time (h)
3Gy/h 100℃ black core
3Gy/h 100℃ white core
3Gy/h 100℃ red core
3Gy/h 100℃ modeled
2.5 percentile
97.5 percentile
(a)

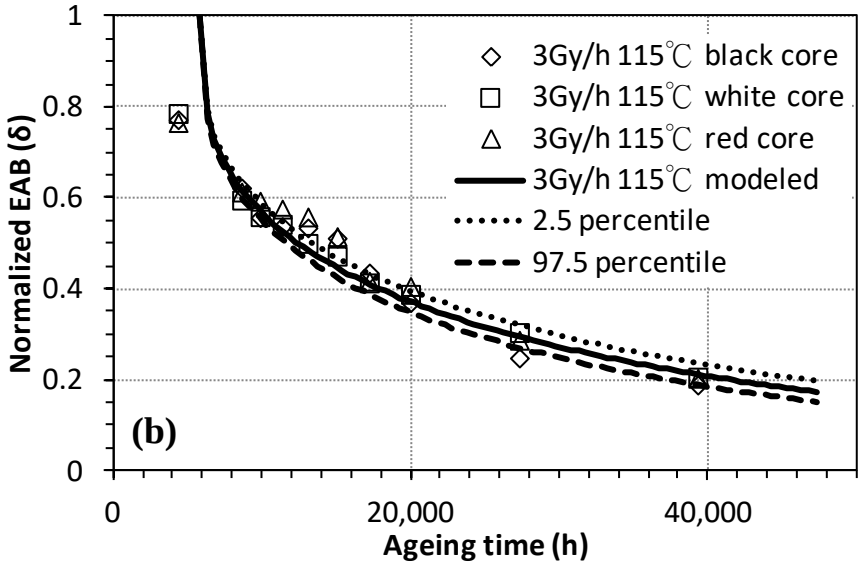
Normalized EAB (δ)
1
0.8
0.6
0.4
0.2
0
0
20,000
40,000
Ageing time (h)
3Gy/h 115℃ black core
3Gy/h 115℃ white core
3Gy/h 115℃ red core
3Gy/h 115℃ modeled
2.5 percentile
97.5 percentile
(b)

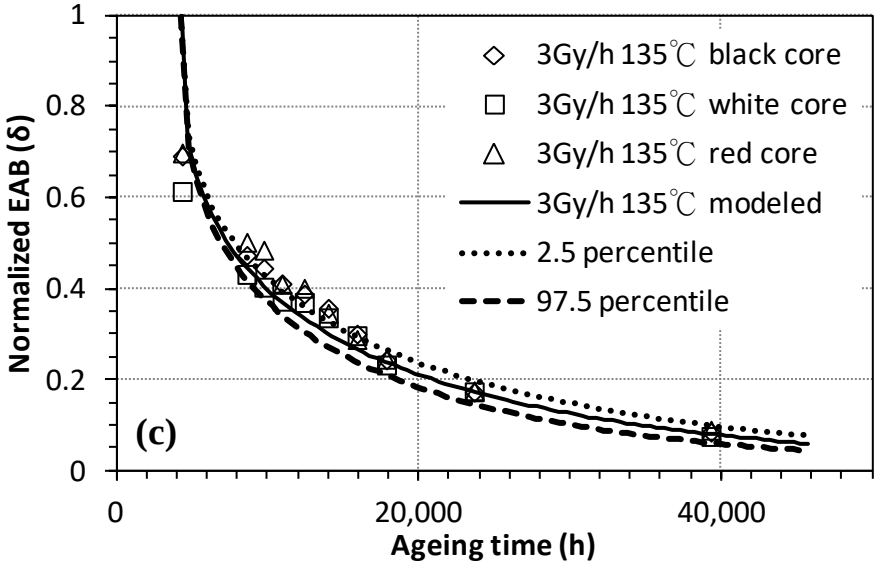

Figure 3.35 Normalized EAB vs. time (SIR at 3 Gy/h)

An example used to demonstrate how to obtain the parameters in Table 3.6 is based on the data points in Figure 3.35(c). Last nine data points in the figure with an aging time longer than 16,000 hours are considered since the EAB close to 50% is interested [6]. The prior for ν is assumed to be a uniform distribution between 0 and 0.0001. Since the error term σ must be a positive value, lognormal distribution is used for the prior with the mean at 0.02 and variance at 2. The result of the estimation is detailed in Table 3.6. The probability distributions of the drop-off rate (ν) and ($1/\sigma^2$) are plotted in Figure 3.36 and Figure 3.37, respectively.

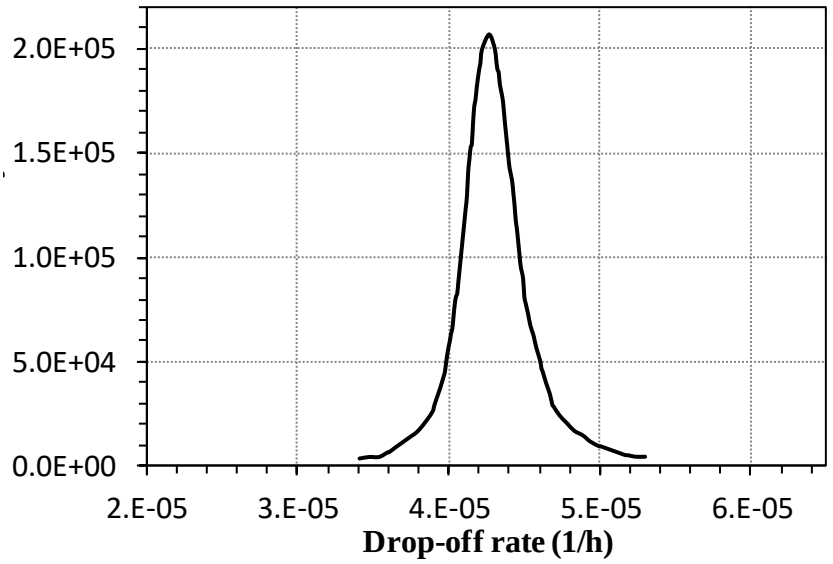

Figure 3.36 The PDF of ν of SIR at 3 Gy/h 135℃

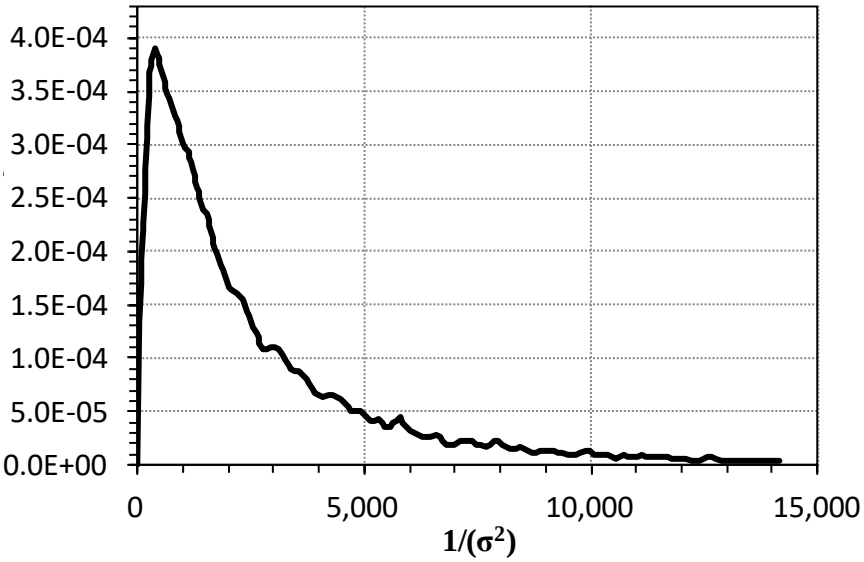

Figure 3.37 The PDF of $(1/\sigma^2)$ of SIR at 3 Gy/h 135℃

Based on rearranging Eq. 3.20, Eq. 3.26 is obtained. Since absolute EAB at 50% is

interested in this research [6], and the average EAB of non-degraded SIR is 352%, (δ = 50% ÷ 352% ≈ 0.14) is plugged into Eq. 3.26. Different ν values at 3 Gy/h and 135℃ corresponding to each percentile in Table 3.6 are plugged into Eq. 3.26 to estimate the lifespan of the insulation shown in Figure 3.38.

$$t = \frac{\ln[1-(1-\delta)^3]}{-\nu} + \tau_0 \qquad \text{Eq. 3.26}$$

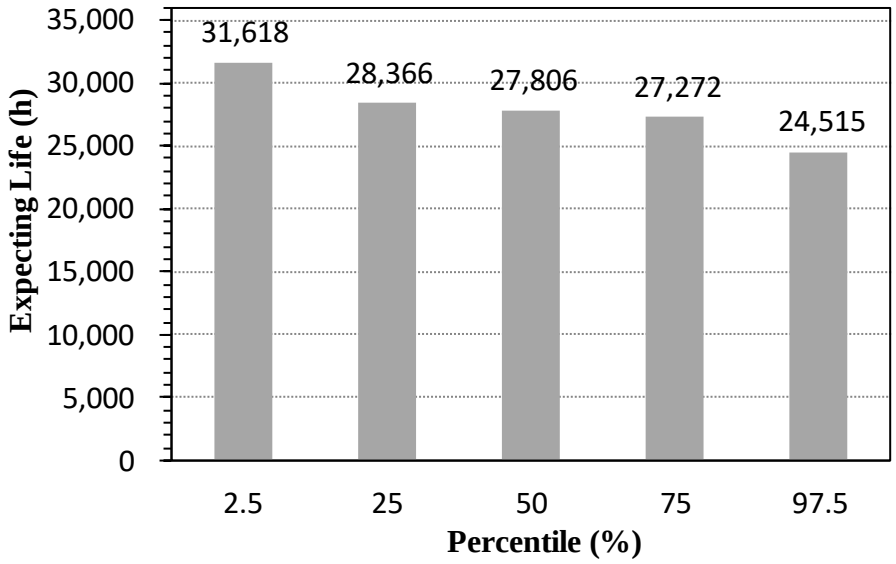

Figure 3.38 Predictive lifespan of SIR at 3 Gy/h, 135℃, and EAB=50%

According to the approaches discussed above, corresponding to Figure 3.35, degradation curves in other aging conditions are plotted in Figure 3.39 and Figure 3.40.

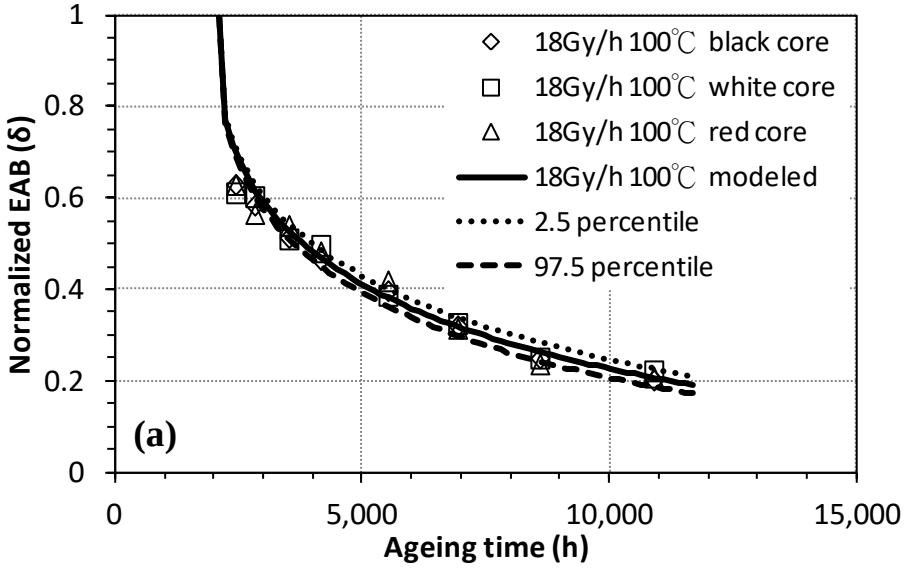
Normalized EAB (δ)
Ageing time (h)
18Gy/h 100℃ black core
18Gy/h 100℃ white core
18Gy/h 100℃ red core
18Gy/h 100℃ modeled
2.5 percentile
97.5 percentile
(a)
0
0.2
0.4
0.6
0.8
1
0
5,000
10,000
15,000

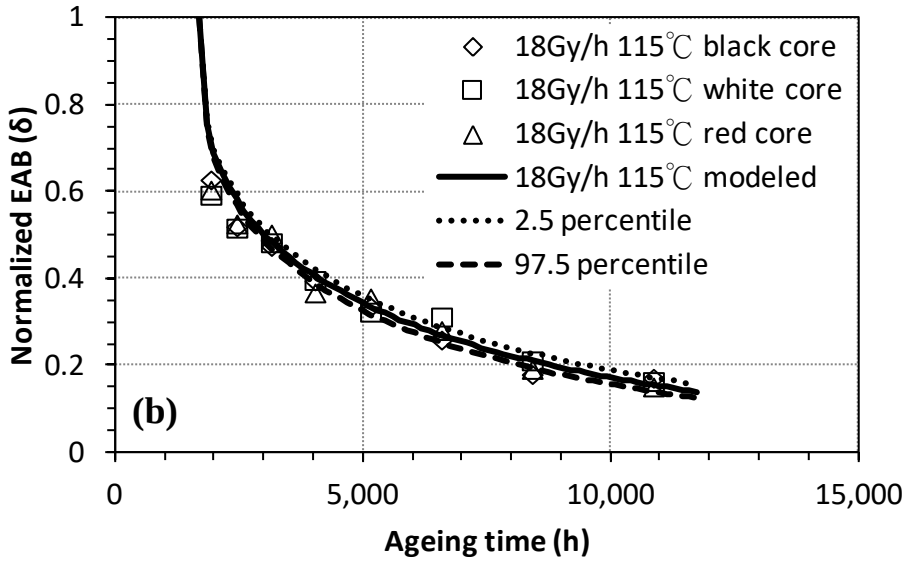
Normalized EAB (δ)
Ageing time (h)
18Gy/h 115℃ black core
18Gy/h 115℃ white core
18Gy/h 115℃ red core
18Gy/h 115℃ modeled
2.5 percentile
97.5 percentile
(b)
0
0.2
0.4
0.6
0.8
1
0
5,000
10,000
15,000

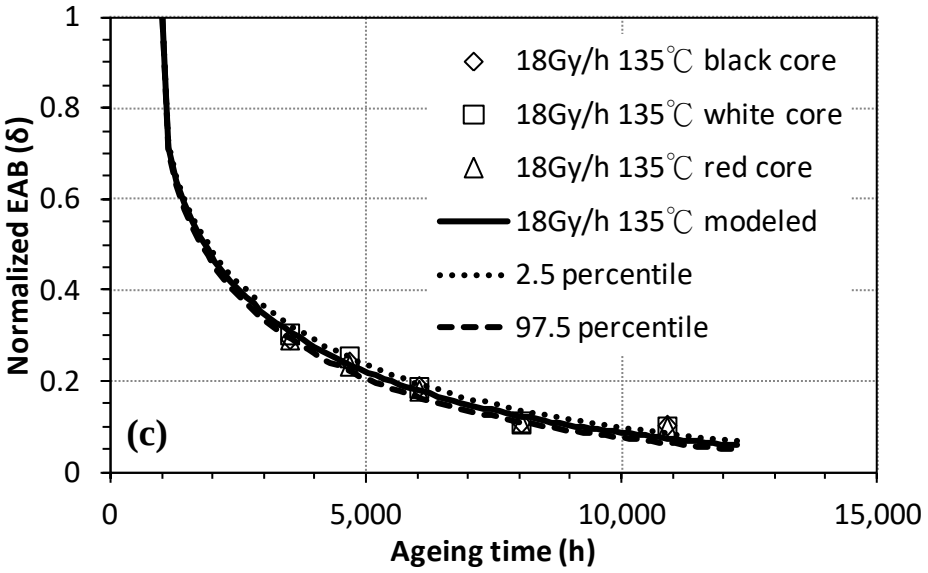

Figure 3.39 Normalized EAB vs. time (SIR at 18 Gy/h)

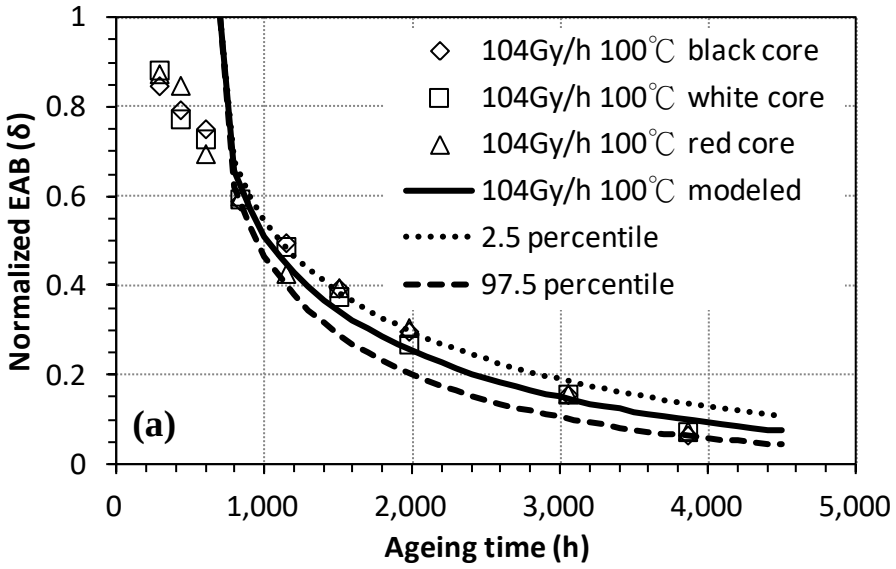

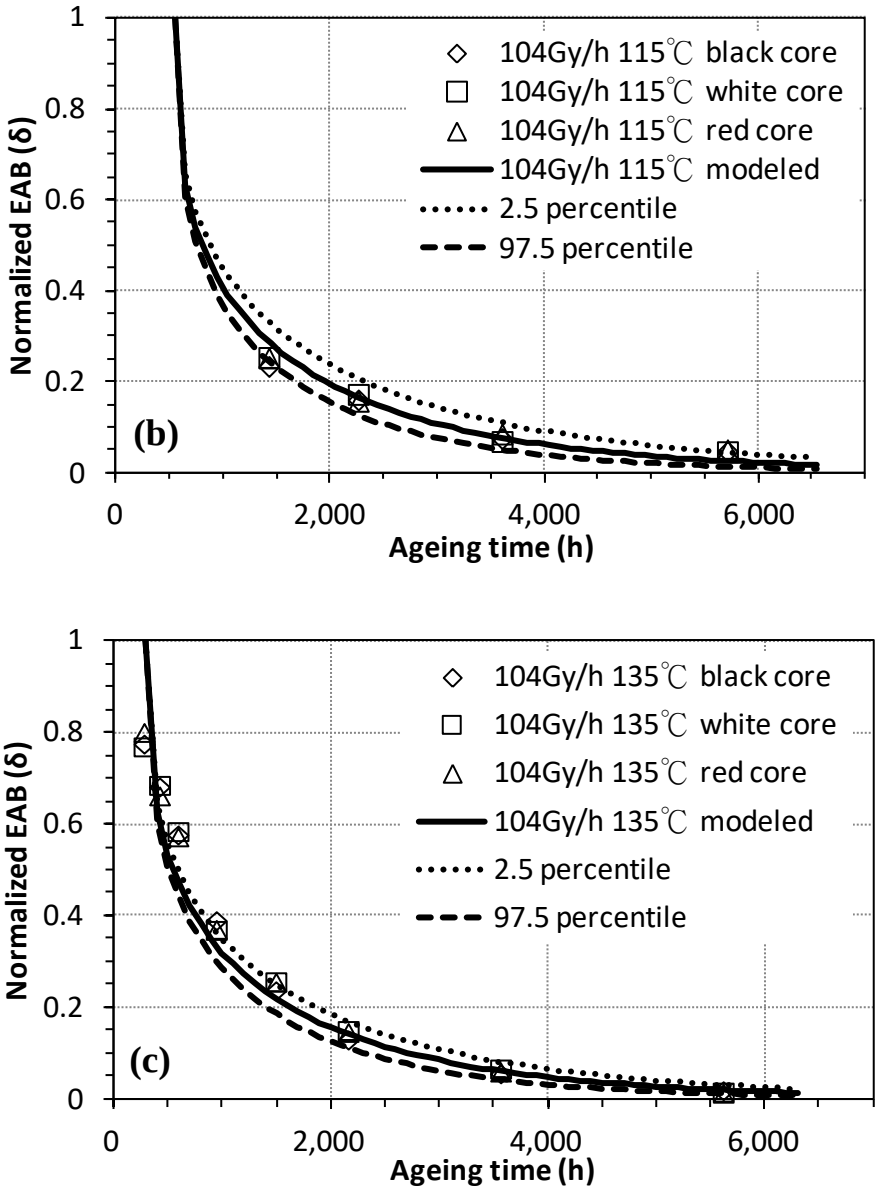

Figure 3.40 Normalized EAB vs. time (SIR at 104 Gy/h)

The modeled drop-off rates at different aging temperatures and dose rates in Figure 3.35, Figure 3.39, and Figure 3.40 are plotted in Figure 3.41. The same data points are further plotted in the form of Eq. 3.18 and shown by the discrete pattern in Figure 3.42. After linear

fitting is applied, the ΔG can be calculated by (-slope × R) based on Eq. 3.18. The values of the ΔG corresponding to each dose rate are plotted in Figure 3.43. Other relations among drop-off rate, incubation time, aging temperature, and dose rate are shown in Figure 3.44, Figure 3.45, and Figure 3.46. When all the data points in Figure 3.35, Figure 3.39, and Figure 3.40 along their x-axis direction are connected by straight lines, Figure 3.47 and Figure 3.48 can be plotted where their relations are shown in 3D forms.

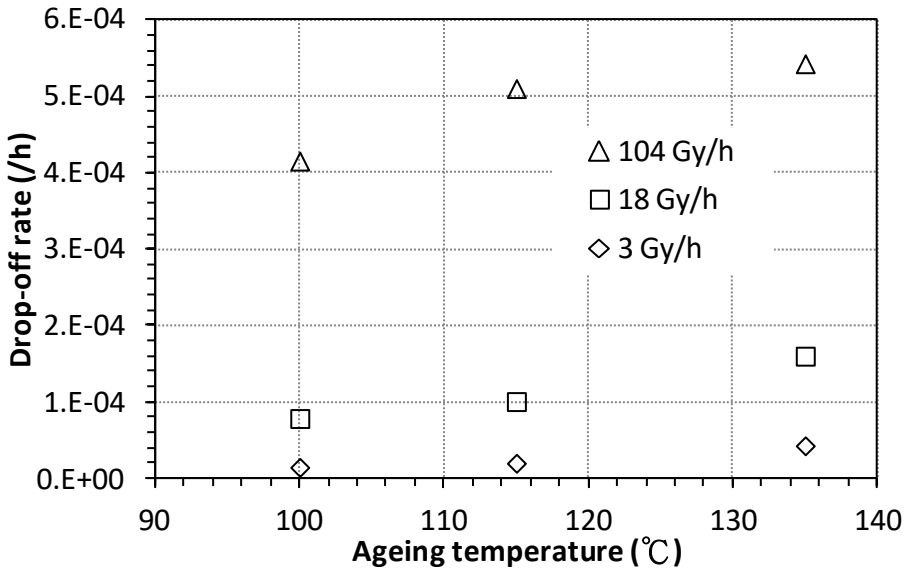

Figure 3.41 Drop-off rate vs. aging temperature (SIR simultaneous aging)

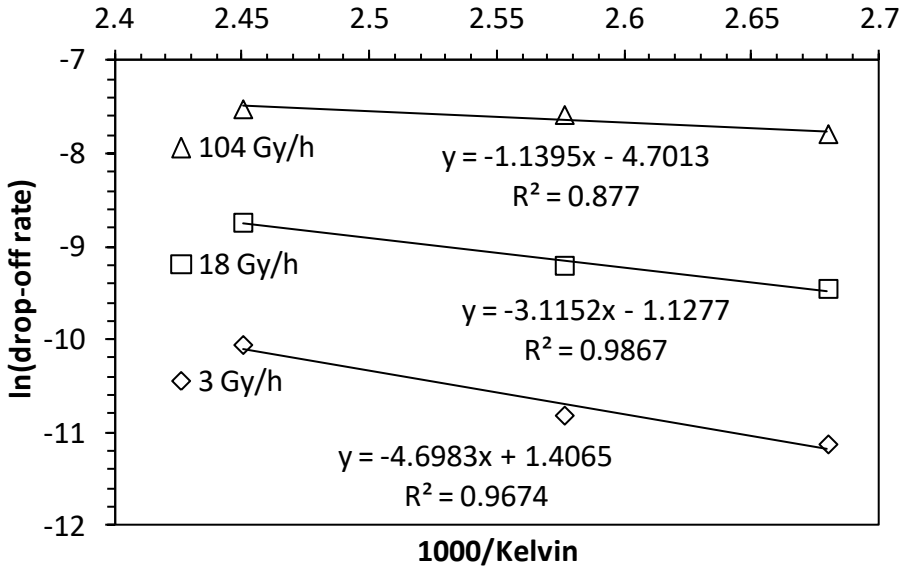

Figure 3.42 Arrhenius plot (SIR simultaneous aging)

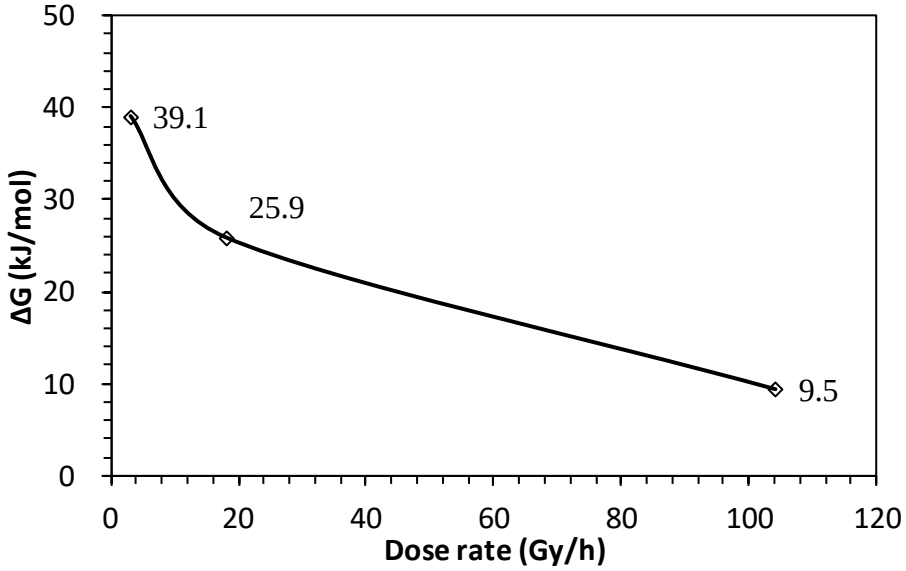

Figure 3.43 Activation energy vs. dose rate (SIR simultaneous aging)

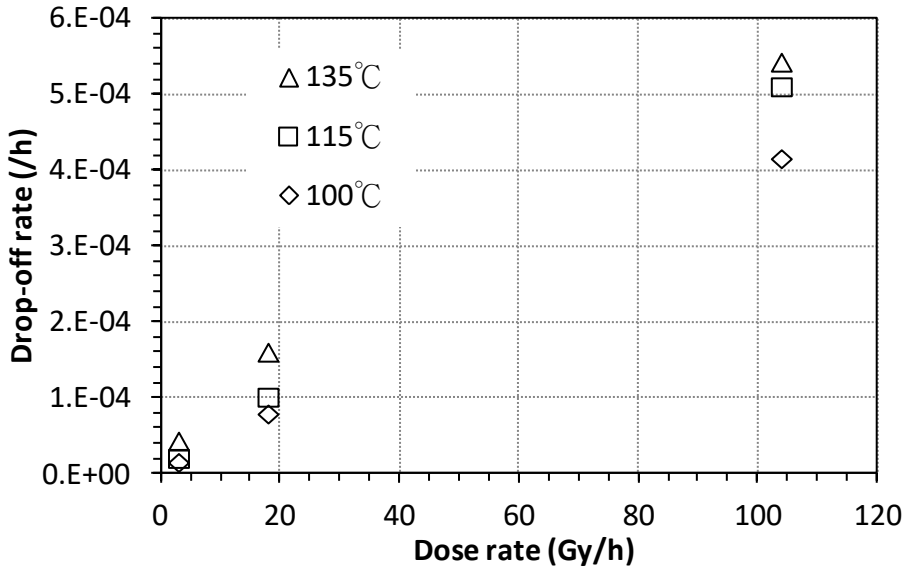

Figure 3.44 Drop-off rate vs. dose rate (SIR simultaneous aging)

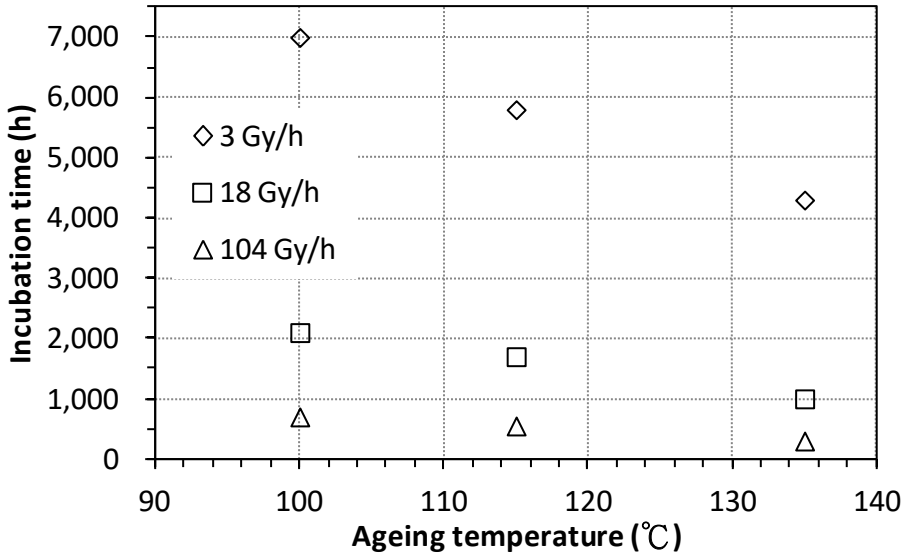

Figure 3.45 Incubation time vs. aging temperature (SIR simultaneous aging)

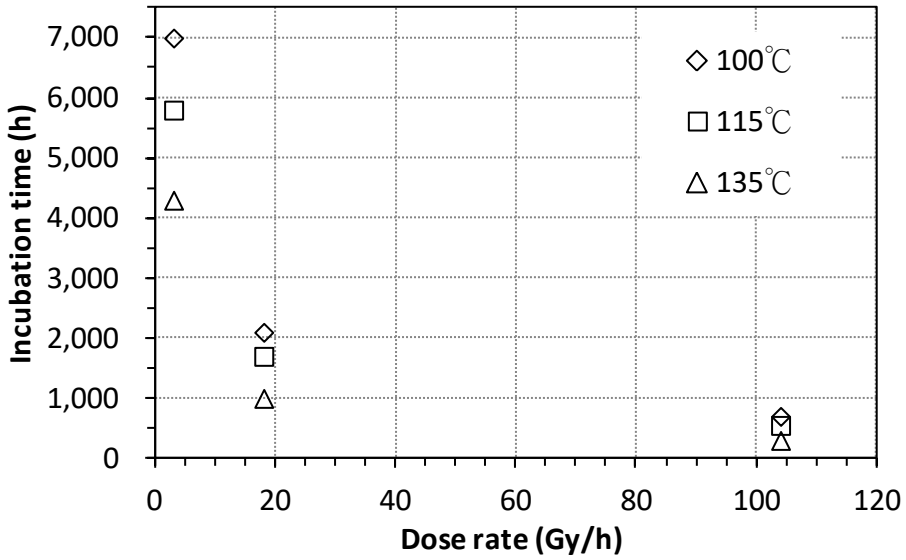

Figure 3.46 Incubation time vs. dose rate (SIR simultaneous aging)

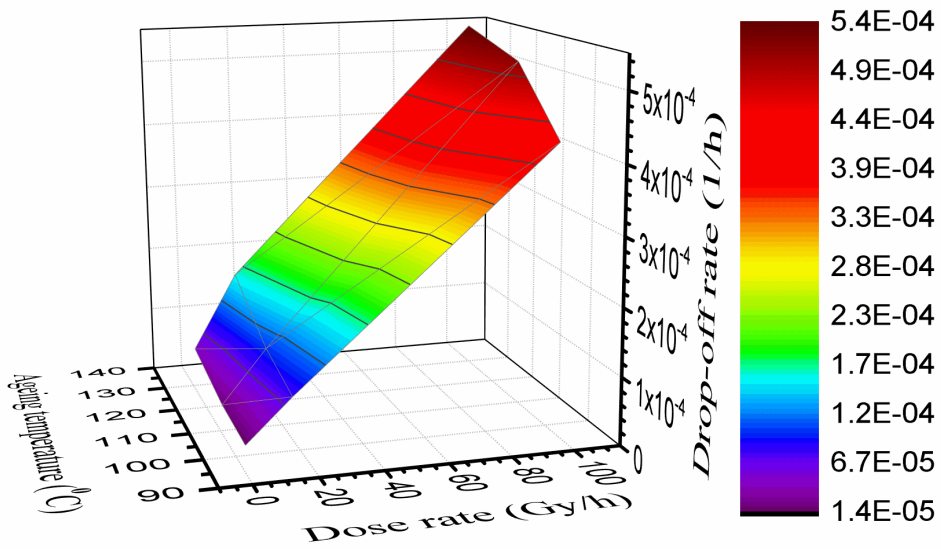

Figure 3.47 Drop-off rate corresponding to aging temperature and dose rate (SIR)

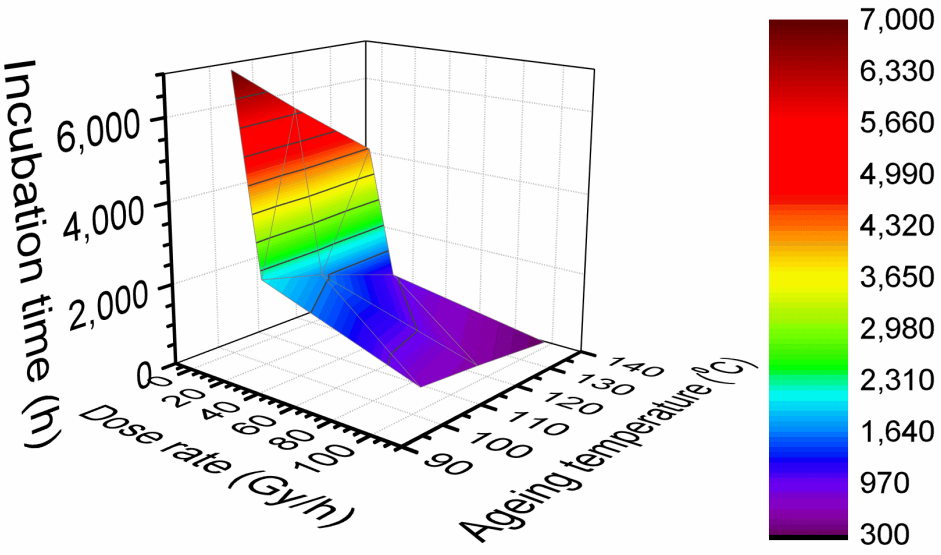

Figure 3.48 Incubation time corresponding to aging temperature and dose rate (SIR)

3.2.7.2 Validation - XLPE in Diffusion Control

Bayesian parameter estimation can also be applied to the calculation of the distribution of D in Eq. 3.3. The following are the steps. Set $\tau_0 = 0$. The measured concentration $\xi(x,t)$ of the carboxylic groups on a cross-section can be obtained by FTIR [34]. c(x,t,D) calculated by Eq. 3.3 is deterministic, which can predict the concentration. However, there is always uncertainty between the measured and predicted values. It is reasonable to assume that $\xi(x,t)$ is normally distributed around μ_C. μ_C is the average of c(x,t,D) at a given position and time. Therefore, the average can be represented by Eq. 3.27.

$$\mu_C(x,t,D) = \text{Eq. 3.3} \qquad \text{Eq. 3.27}$$

The probability of normally distributed ξ(x,t) can be represented by Eq. 3.28.

$$\Pr\left(\xi|\mu_C,\sigma^2\right)=\frac{1}{\sqrt{2\pi\sigma^2}}\exp\left(-\frac{\left(\xi-\mu_C\right)^2}{2\sigma^2}\right) \quad \text{Eq. 3.28}$$

Based on Eq. 3.28, the likelihood function of Bayesian parameter estimation can be represented by Eq. 3.29 where D and σ are the priors.

$$\Pr(\xi(x,t)|D,\sigma^2)=\frac{1}{\sqrt{2\pi\sigma^2}}\exp\left(-\frac{\left(\xi(x,t)-\mu_C(x,t,D)\right)^2}{2\sigma^2}\right) \quad \text{Eq. 3.29}$$

By Eq. 3.29 and Bayesian parameter estimation, the distribution of D can be calculated. On the other hand, the time (t) required to reach the failure can be determined by an experiment. After plugging the t and the mean of D into Eq. 3.15, the value of V_d corresponding to the timing of the failure can be defined. In other words, V_d can serve as an indicator of the failure caused by the oxidation controlled by the diffusion of oxygen. Moreover, by the defined V_d and the distribution of D, the distribution of t can be calculated according to Eq. 3.15, which renders the uncertainty of the lifespan of cable insulation.

The experimental data used to validate Eq. 3.3 and Eq. 3.15 are from the XLPE-1B sample at 135℃ discussed in a published paper [34]. The thickness of the sample (L) is 2 mm. In order to calculate the uncertainty of D in Eq. 3.3, the likelihood function expressed by Eq. 3.29 is applied to Bayesian parameter estimation whose concept is represented by Eq. 3.21. The priors for D and σ are assumed to be uniform distributions. D ranges from 10^{-14} to 10^{-12}. σ ranges from 0 to 1. The experimental data are the concentration of the oxide, which is plotted by the discrete patterns in Figure 3.49. After applying Bayesian parameter estimation, the distribution of D and σ are determined and plotted in Figure 3.50 and Figure 3.51, respectively. The continuous lines in Figure 3.49 are plotted according to Eq. 3.3 where the value of D is the mean value listed in Table 3.7. Figure 3.49 shows that Eq. 3.3 based on the diffusion of oxygen fits the concentration of the oxide measured by FTIR. Therefore, it proves that the concentration of oxide is linearly proportional to the concentration of oxygen in a bulk XLPE, which is an assumption discussed in the section of modeling.

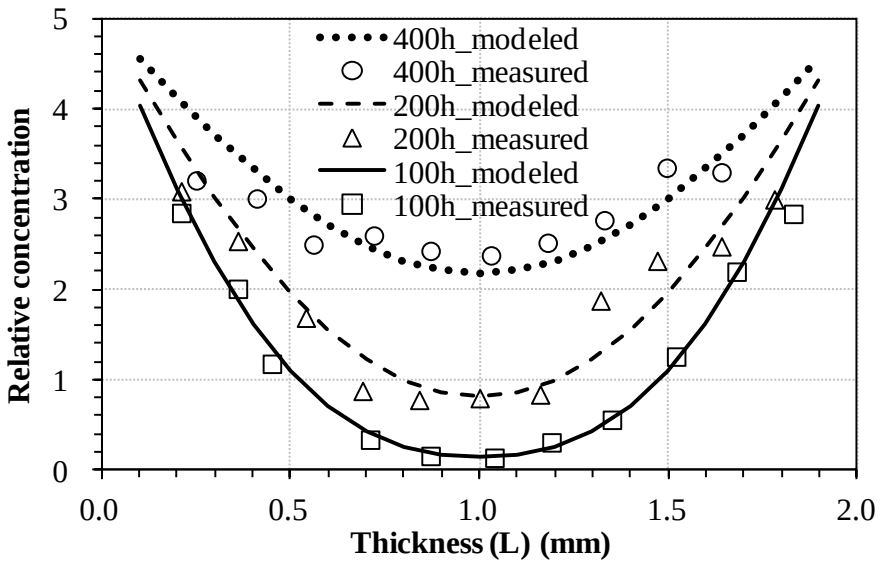

Figure 3.49 The comparison of the concentration of the oxide between experimental data [34] and modeled curves plotted by discrete patterns and continuous lines, respectively

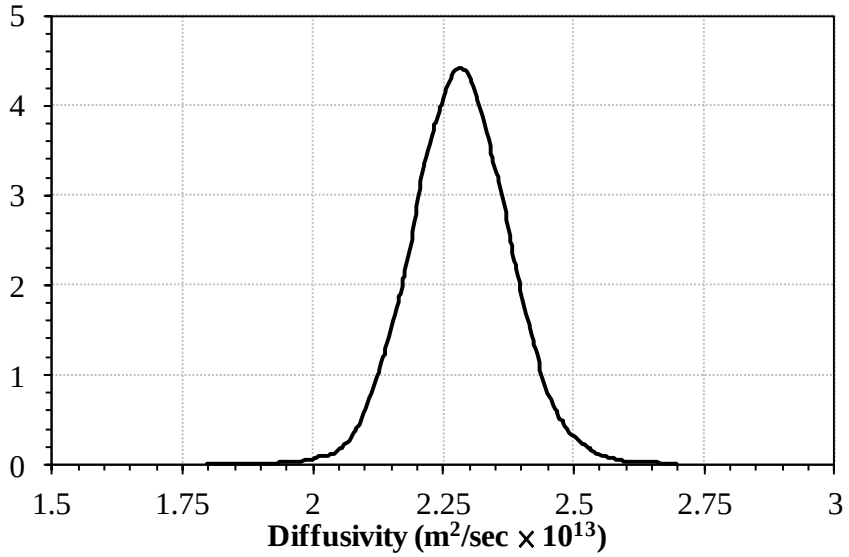

Figure 3.50 The PDF of D

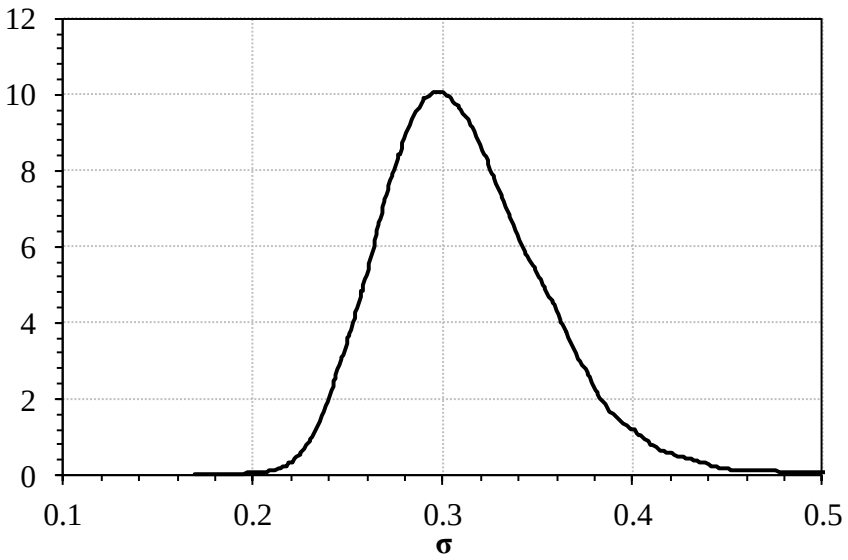

Figure 3.51 The PDF of σ

Table 3.7 Diffusivity × 10^{13} m^2/s

Average	2.5%	25%	50%	75%	97.5%
2.284	2.107	2.222	2.283	2.344	2.468

V_d is an indicator of the degree of the degradation with respect to diffusion-controlled oxidation. The threshold of V_d can be defined by the following steps. IAEA suggests that 0.5 to be the minimum of the absolute EAB for the insulation used in a power plant [6]. XLPE samples adopted by this research show that when the ageing time reaches 400 hours, the absolute EAB is 0.5 [34]. After plugging t = 400 hours and the mean value of D listed in Table 3.7 into Eq. 3.15, the threshold of V_d can be defined at 0.64. When the value of V_d is fixed, corresponding to the distribution of D listed in Table 3.7, the uncertainty of t in Eq.

3.15 can be calculated and plotted in Figure 3.52. This figure represents the reliability of the XLPE insulation controlled by the diffusion oxygen.

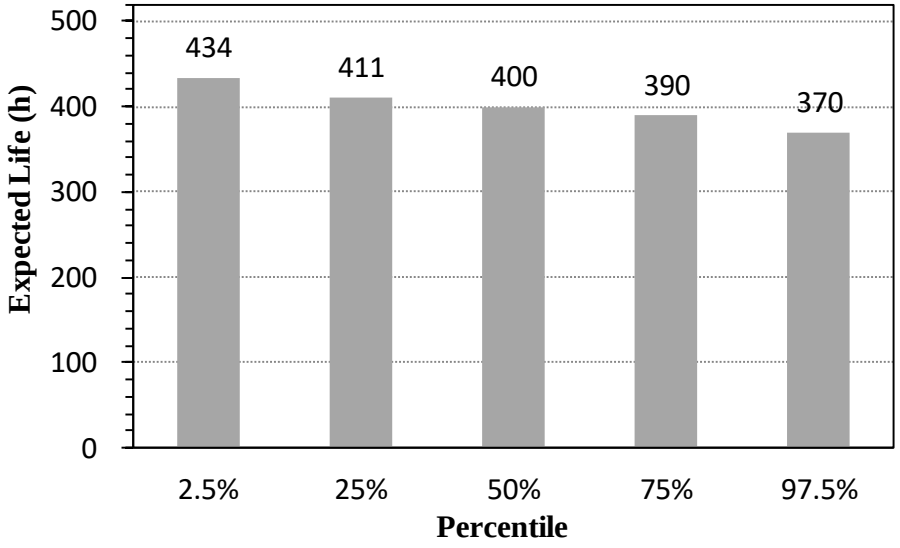

Figure 3.52 The expected lifespan of the XLPE insulation under diffusion control

3.3 Discussion of Mechanical Degradation

The purpose of the empirical factor β is to modify Eq. 3.12 and Eq. 3.15 since the concept of the two equations is based on uniform degradation. Diffusion-controlled oxidation is not uniform especially when aging time is short. Therefore, short-term δ shall be corrected by β. On the other hand, the absolute value of δ at long-term must be small; therefore, β does not significantly affect the value of δ when the time is long at which the oxidation profile approaches uniform. Hence, empirical factor β can pertinently modify the whole δ curve. High

oxide concentration possesses low ductility. When a tensile test is applied, cracks may easily occur at a surface and deteriorate the EAB. This can be one of the reasons making the experimental data drop faster than the predicted curve does in Figure 3.7. Moreover, the purpose of this research is to model the long-term δ. The curves corresponding to different β values converge when the time is long at which β makes little effect on a δ curve, which means Eq. 3.16 is pertinent.

Being able to model the shape change [83] of the data trend is an important requirement for a time-dependent EAB model. One main purpose of the validation section of EPR is to show that Dichotomy Model can accommodate the shape change of the data trend when the insulation is subject to different external conditions, such as temperature- and radiation-dominated environment. Temperature-dominated reaction occurs at high temperature and low dose rate, while radiation-dominated reaction takes place in the opposite conditions. Figure 3.53 shows two of the aging conditions in Figure 3.23. The x-axis of Figure 3.53(a) is logarithmic while Figure 3.53(b) is a linear plot which can express the drop-off trends in a more intuitive way in order to show the shape change between two opposite conditions. The shape change means equation Eq. 3.30 holds.

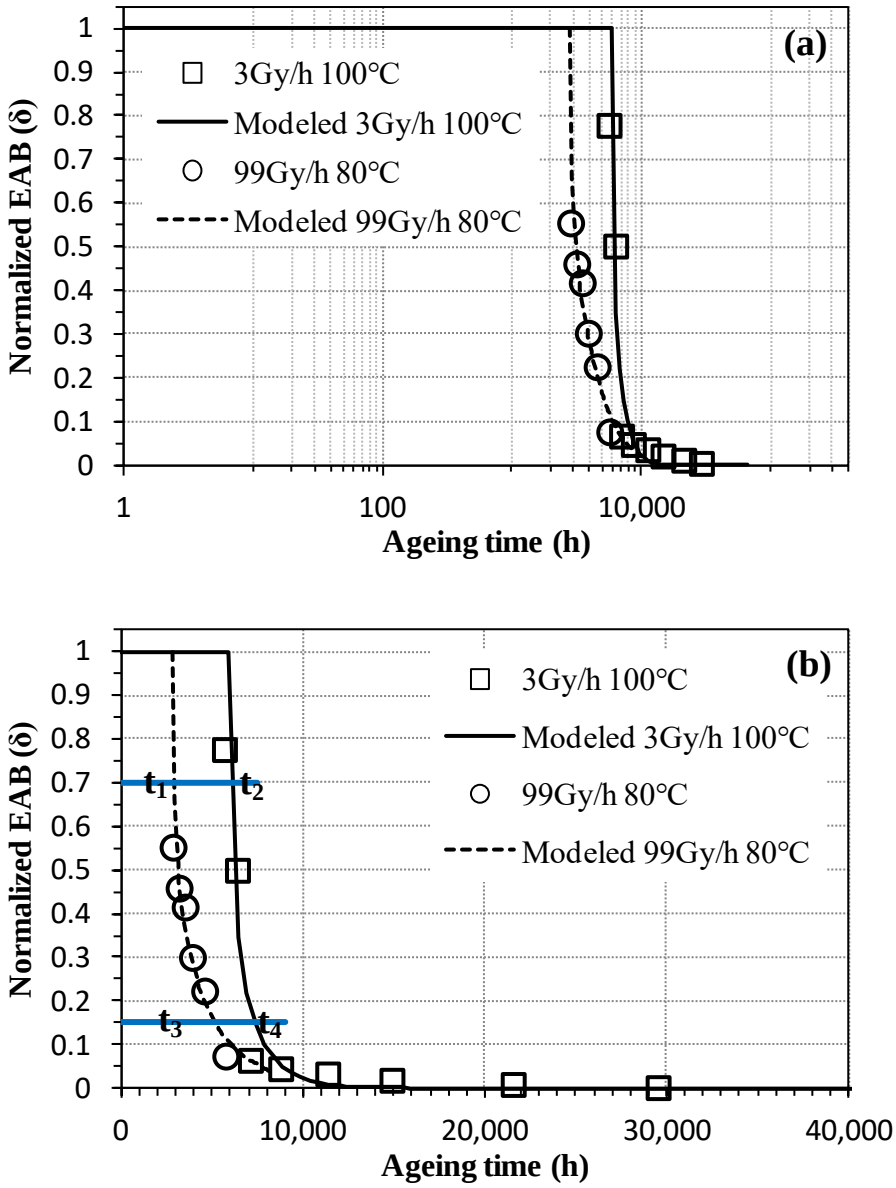

Figure 3.53. Normalized EAB of white core FR-EPR from company A [20] in (a) logarithmic x-axis, and (b) linear x-axis

$$\frac{t_2}{t_1} \neq \frac{t_4}{t_3} \qquad \text{Eq. 3.30}$$

where t_n are the intersections of the horizontal lines and modeled curves in Figure 3.53.

The shape change of the EAB trends is not achievable by TDD approach since its shift factor horizontally connects every paired data points at the same EAB value between two environmental conditions [80]. In other words, TDD can be applied to the materials only when their EAB behavior follows Eq. 3.31 rather than Eq. 3.30. However, for many cable insulations such as EPR and SIR, the shapes of the trends follow Eq. 3.30, as shown in the section on validation. The shape change may be caused by different forms or rates of chemical reactions when an aging temperature or dose rate is varied.

$$\frac{t_2}{t_1} = \frac{t_4}{t_3} \qquad \text{Eq. 3.31}$$

Drop-off rate ν is a concept of ratio per unit time, which is the same as the parameter of an exponential distribution. ν determines the rate of the increasing V_d, which is the same to the concept of CDF represented by Eq. a. 15. According to Eq. 3.4, Eq. 3.12, and Eq. 3.20, when ν increases, the curvature of EAB as a function of time becomes steeper. It must be emphasized that ν is based on EAB only. It is not equal to chemical reaction rate. Usually, ν increases as the temperature is raised, as shown in Figure 3.13 and Figure 3.41. However, as for the effect of radiation on ν, the trend is not monotonic. For instance, the ν of the silicone

rubber in the paper [20] increases when dose rate is increased, but the ν of the EPR in the same paper decreases when dose rate is varied from 18 Gy/h to 99 Gy/h. Another paper also reports similar phenomenon [96]. In other words, the increase of dose rate is not always accompanied by the increase of ν. Radiation-induced cross-linking can decrease EAB, for example. However, the formation of cross-linking requires different reactions consisting of bond scission, chain migration, and recombination [97]. Radiation may unevenly contribute to these reactions and affect the efficiency of cross-linking.

In the incipiency of the degradation caused by radiation or heat, experimental data shows there is a period of time when the decrease of EAB is not significant [20, 80]. In this research, the period of time is termed τ_0 represented by a zero drop-off rate, which is determined by the intersection of δ=1 and Eq. 3.20, and shown in Figure 3.1. In the section on validation, though the EAB within τ_0 only slightly decreases, the length of τ_0 significantly decreases when an aging temperature or dose rate is raised. It may suggest chemical reactions are in process although the EAB does not significantly change. One of the reasons can be the overall effect contributed by both mechanical and chemical cross-linking when the polymer is subject to radiation. Polymer chains are tangled and threaded with one another to increase the entropy, which can restrict their relative movements. This is mechanical cross-linking since the effect is not contributed by covalent bonds between chains. When radiation is applied, the

effect of mechanical cross-linking is replaced by that of chemical cross-linking rendered by radiation, but the overall effect on the EAB is not significantly changed within τ_0. Figure 3.16 and Figure 3.46 are also evidence indicating that radiation effect is important to τ_0. When dose rate is increased from 3 Gy/h to 98 Gy/h in Figure 3.46, the differences of τ_0 among 80°C, 90°C, and 100°C become very small. This suggests radiation dominates the chemical reactions when dose rate is high while temperature effect becomes much insignificant.

When EPR is in a radiation-dominated condition, the curve of the EAB as a function of time is close to a straight line. This linear relation is shown in the circle pattern of Figure 3.53(b). One straight line from point (0,1) can be plotted to fit the circles. However, the authors of this article would like to explain this "linear fit" in a different way. A linear fit may not be proper since when the time is long, the slope of the EAB experimental data shall gradually become smaller and approach to a horizontal line. A linear fit cannot provide a curve with a dynamic slope to fit the experimental data. In this newly proposed model, when radiation is strong, τ_0 becomes shorter and ν gets larger, which makes an EAB vs. time curve steeper and look like a straight line at the beginning of degradation. After V_d is large enough, the slope of an EAB curve becomes smaller and approaches to a horizontal line. The newly-proposed model may be more pertinent to the long-term behavior of EAB compared to a linear fit when EPR is in a radiation-dominated condition.

According to the modeling definition and physical significance of drop-off rate and incubation time, and the modeled result in Figure 3.41, Figure 3.44, Figure 3.45, and Figure 3.46, the values of ν and τ_0 follow the trends corresponding to aging temperature and dose rate. Therefore, by Eq. 3.20, $\delta=1$, and the trends of these two parameters, the EAB as a function of time can be established. The parameters of this predictive model within the ranges of these experimental conditions are illustrated by 3D plots shown in Figure 3.47 and Figure 3.48.

Neither TDD nor DED has tackled the uncertainty of the EAB. This research starts with a physics-based approach by building the relation between the EAB and the integral of ν to derive a deterministic function represented by Eq. 3.20. Then the EAB equation as a function of time is converted into a probabilistic model represented by equation Eq. 3.21 and Eq. 3.25 to quantify the uncertainty of ν shown in Figure 3.36. Accordingly, the curve of the EAB against a time axis can be represented by the form of probability such as the lines in Figure 3.35. The uncertainty of ν renders the distribution of the expecting lifespan of cable insulation shown in Figure 3.38. This unprecedented approach introduces a viewpoint of probability addressing the degradation of cable insulation subject to heat and radiation.

Chapter 4: Electrical Degradation

4.1 Trend of Electrical Resistance

Due to thermal degradation, the trend of the electrical resistance or resistivity of XLPE plotted against time is shown in Figure 4.1 [26, 77, 78]. R_0 is the resistance of non-degraded XLPE. After XLPE is exposed to heat for a long time, its resistance approaches a "degraded final" value R_d. In phase 1, the slope of the solid line gradually decreases. After t_s, there is a sudden drop whose drop-off rate subsides as time approaches t_f. The transition phase is defined by the dashed line between t_s and t_f. After t_f, the convex curve approaches a horizontal line, which is named phase 2, represented by the chain line. When degradation is at different temperatures, the trend is illustrated in Figure 4.2. The slope of phase 1 becomes steeper and the length of the transition phase is shorter as the aging temperature is raised. When the temperature is high enough, the phases denoted by solid, dash, and chain lines seem merged, as shown by the dotted line in Figure 4.2.

The logic of this model starts from deriving the resistance as a function of time (t) and drop-off rate (ν), where t is a variable and ν is a parameter. To be more specific, the differential of this function with respect to time, or the slope against the time axis, becomes steeper as ν increases. The solid line in Figure 4.2 can be represented by this function. Also, as the aging temperature is increased, the three phases merge and this function can represent

the whole process shown by the dotted line in Figure 4.2. Different values of ν are tested to fit the experimental data shown by the solid and dotted lines in Figure 4.2. It should be emphasized that ν is measured by the behavior of the resistance but not the chemical reaction rate. It is worth noting that this fitting approach is a well-established method in modeling in many areas [88-91].

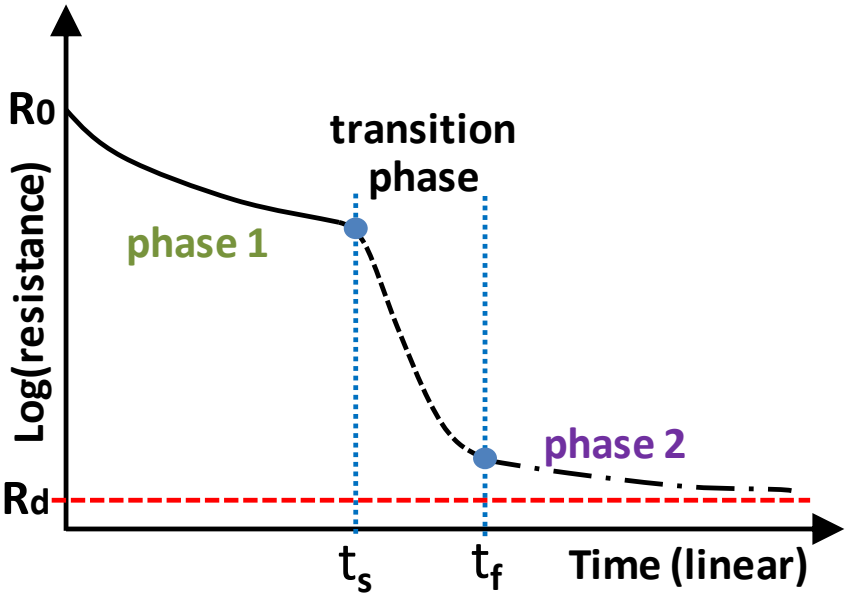

Figure 4.1 Trend of the resistance of XLPE in thermal degradation

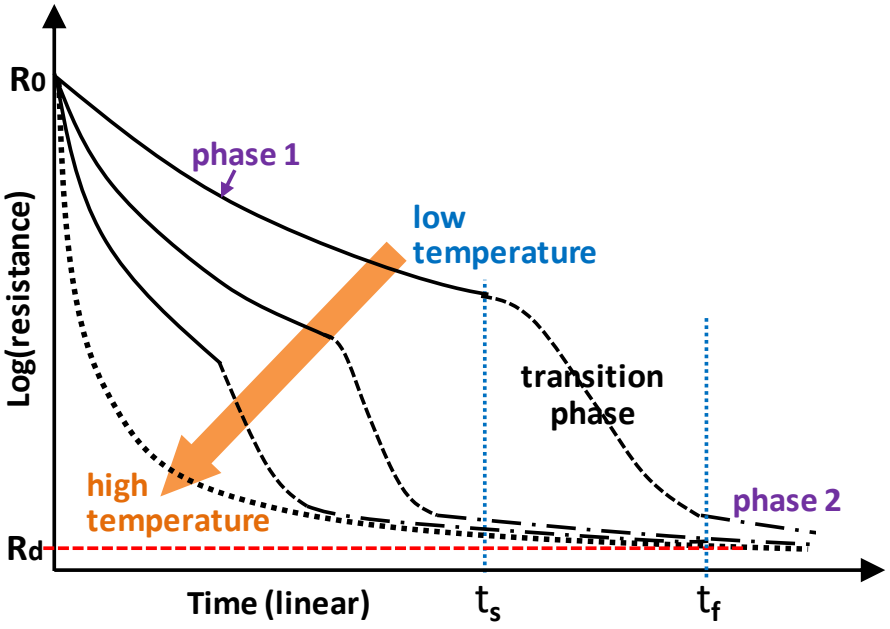

Figure 4.2 Trend of the resistance of XLPE degraded at lower and higher temperatures

4.2 Application of Dichotomy Model

The degradation of XLPE cable insulation represented by phase 1 denoted in Figure 4.1 and Figure 4.2 is assumed to be homogeneous. Therefore, similar to section 3.2.2, a piece of cable insulation can be regarded as the combination of a large number of small cubes. Virtually degraded cubes are uniformly distributed among the virtually non-degraded cubes. The ratio of the degraded part (V_d) is represented by Eq. 4.1.

$$V_d = \frac{\text{The volume of all virtually degraded subcubes}}{\text{The volume of all subcubes}} \qquad \text{Eq. 4.1}$$

V_d in Eq. 4.1 as a function of time can be obtained according to exponential distribution, which is detailed in Appendix A. In other words, V_d follows the same function as Eq. a. 15. The meaning of ν corresponds to that of λ in Eq. a. 15 and Eq. a. 20. In other words, within a limited volume, ν fraction of the material is degraded during a short time interval. Therefore, the accumulated degraded part V_d can be represented by the CDF of an exponential distribution, shown in Eq. 3.4 [86]. V_d is termed virtual degradation ratio, similar to the V_d in section 3.1.2.

4.3 Percolation

Besides the total of the accumulated degraded material, or V_d, the distribution of the degraded parts can also dominate the electrical conductivity since their electrical resistivity is much lower than that of the non-degraded portion. Hence, this research considers the percolation phenomenon caused by the degradation reaction. As shown in Figure 4.3, in the beginning, t_0, V_d is zero. As time elapses, some of the material is degraded; the circles represent the degraded parts which are evenly distributed in a bulk. In this model, the increase of V_d follows Eq. 3.4. When V_d reaches a certain amount denoted by t_3 in Figure 4.3, degraded parts start to form a continuous channel for a current to flow from the upper surface, through the degraded material, to the bottom surface as voltage is applied to the electrodes, as shown by the rectangles attached to the upper and bottom surfaces. This degraded part can

introduce a path for a current with low electrical resistance, which is termed percolation. The current is represented by the solid line at t_3 in Figure 4.3. Percolation is the cause of the sudden drop of the resistance represented by the transition phase in Figure 4.1 and Figure 4.2. Before the onset of percolation, in phase 1, our model assumes that all the currents uniformly flow through a non-degraded or partially degraded bulk, which is shown in Figure 4.4 where the arrows mean currents.

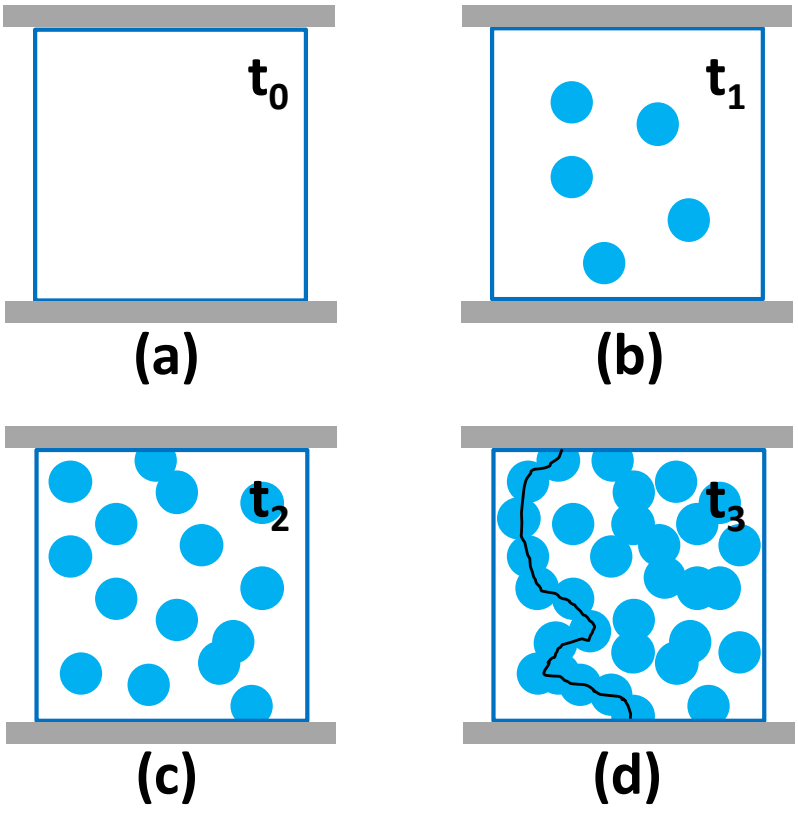

Figure 4.3 Illustration of the formation of percolation

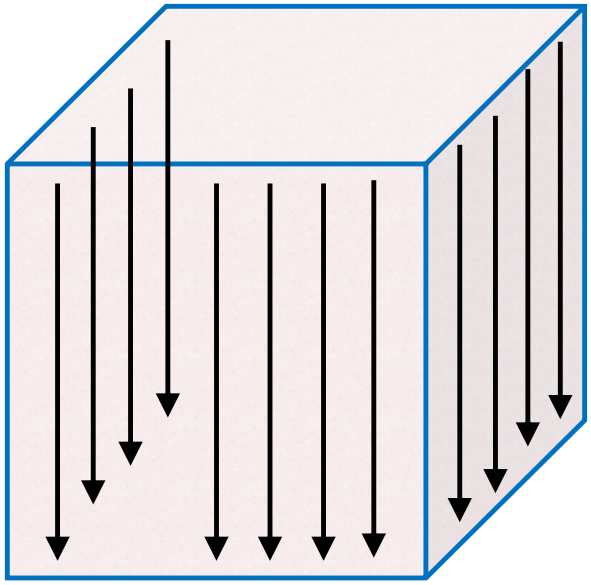

Figure 4.4 Illustration of uniform current flow

4.4 Model for Phase 1

The derivation in this section aims to determine the electrical resistance of a bulk material subject to uniform degradation. To calculate the resistance before the onset of percolation, a specimen is modeled as a unit cube shown in Figure 4.5(a). The unit cube is further divided into a large number of equal subcubes. Currents denoted by the darker arrow evenly flow via each column piled up by the subcubes whether the column is non-degraded or partially degraded, shown in Figure 4.5(b) and (c), respectively. The degraded part is denoted by the darker subcubes which are evenly distributed in each column. The darker subcubes decrease the resistance of a column due to the lower resistivity of the degraded subcube compared to that of the non-degraded subcube.

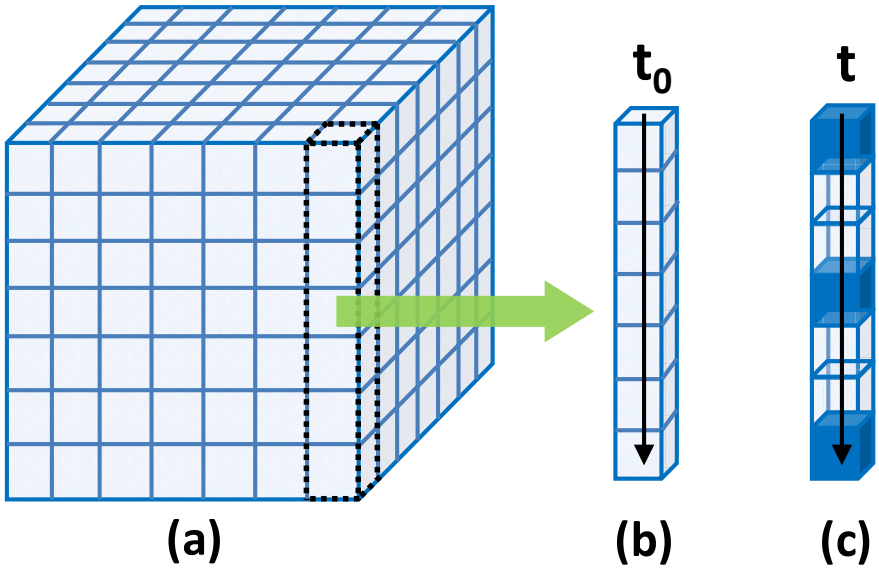

Figure 4.5 (a) A unit cube specimen divided into an infinite number of equal subcubes. (b) One of the columns before, and (c) after aging.

The resistance and resistivity of a material can be calculated by Eq. 4.2, Eq. 4.3, and Eq. 4.4.

$$v = I \times R \qquad \text{Eq. 4.2}$$

$$\rho = R \times \frac{A}{l} \qquad \text{Eq. 4.3}$$

$$R = \rho \times \frac{l}{A} \qquad \text{Eq. 4.4}$$

where v is applied voltage; I is current; R is resistance; ρ is resistivity; A is the area of the cross-section of a specimen perpendicular to a current; l is the length of a specimen parallel to a current.

A unit cube is composed of n×n×n = n^3 equal subcubes shown in Figure 4.5(a). The side length of a subcube is (1/n). The resistance of a non-degraded subcube R_0 and a degraded subcube R_d can be derived from Eq. 4.4, and represented by Eq. 4.5 and Eq. 4.6, respectively.

$$R_0 = \rho_0 \times \frac{\frac{1}{n}}{(\frac{1}{n})^2} = \rho_0 \times n \qquad \text{Eq. 4.5}$$

$$R_d = \rho_d \times \frac{\frac{1}{n}}{(\frac{1}{n})^2} = \rho_d \times n \qquad \text{Eq. 4.6}$$

where ρ_0 and ρ_d are the resistivity of the non-degraded and degraded parts of a material, respectively. In this research, ρ_0 is much larger than ρ_d.

The numbers of the non-degraded subcubes, N_0, and the degraded subcubes, N_d, in one single column shown in Figure 4.5(c) can be calculated by Eq. 4.7 and Eq. 4.8, respectively. Eq. 4.9 represents the resistance of one column in Figure 4.5(c), which is R_{cl}. By plugging Eq. 4.5, Eq. 4.6, Eq. 4.7, and Eq. 4.8 into Eq. 4.9, Eq. 4.10 is obtained.

$$N_0 = [(1 - V_d) \times n^3]^{\frac{1}{3}} = n(1 - V_d)^{\frac{1}{3}} \qquad \text{Eq. 4.7}$$

$$N_d = [V_d \times n^3]^{\frac{1}{3}} = n(V_d)^{\frac{1}{3}} \qquad \text{Eq. 4.8}$$

$$R_{cl} = R_0 N_0 + R_d N_d \quad \text{Eq. 4.9}$$

$$R_{cl} = n^2 \left[\rho_0 (1 - V_d)^{\frac{1}{3}} + \rho_d (V_d)^{\frac{1}{3}}\right] \quad \text{Eq. 4.10}$$

Since a unit cube can be viewed as the combination of n^2 columns parallel to one another, the total resistance of a unit cube, R_{tl}, can be determined by plugging Eq. 4.10 into Eq. 4.11 and represented by Eq. 4.12. V_d in equation Eq. 4.12 can be represented by equation Eq. 3.4. Finally, R_{tl} becomes a function of ν and t, shown in Eq. 4.13.

$$\frac{1}{R_{tl}} = n^2 \times \frac{1}{R_{cl}} \quad \text{Eq. 4.11}$$

$$R_{tl} = \rho_0 (1 - V_d)^{\frac{1}{3}} + \rho_d (V_d)^{\frac{1}{3}} \quad \text{Eq. 4.12}$$

$$R_{tl} = \rho_0 (e^{-\nu t})^{\frac{1}{3}} + \rho_d (1 - e^{-\nu t})^{\frac{1}{3}} \quad \text{Eq. 4.13}$$

The Dichotomy Model applied to the electrical resistance of phase 1 is represented by Eq. 4.13, which is used to plot the solid lines and the dot lines in Figure 4.1 and Figure 4.2.

4.5 Model for Transition Phase

The transition phase starts and ends at t_s and t_f as shown in Figure 4.1. This region is caused by percolation illustrated in Figure 4.3. Percolation renders a steep drop of electrical

resistance because of the formation of a direct channel for currents. During percolation, the majority of the currents does not flow via the mixture composed of degraded and non-degraded materials, but dominantly goes through the channel due to the low resistivity of the degraded part. The range of this transition phase on y-axis can be defined by the resistance at the end of phase 1 and the start of phase 2. The range of the transition phase on x-axis can be defined by the value of $V_d(t)$ represented by Eq. 3.4 where the drop-off rate ν can be determined by fitting experimental data. The values of V_d at t_s and t_f will be calculated in the section on validation. The resistance-versus-time curve of the transition phase may be simply modeled by a straight line connecting the two circular points at t_s and t_f in Figure 4.1.

4.6 Model for Phase 2

After a direct channel caused by percolation is formed by the degraded material shown in Figure 4.3, the additional degraded material can broaden the cross-section area or shorten the length of the channel. It does not significantly decrease the resistance by several orders as percolation does. Empirically, the resistance in phase 2 can be modeled by Eq. 4.14.

$$R_{tl\_(n+1)} = R_{tl\_n} \times \frac{t_n}{t_{n+1}} \qquad \text{Eq. 4.14}$$

R_{tl} is the resistance; n in R_{tl_n} starts from the first measured point in phase 2 in Figure 4.1. $R_{tl\_(n+1)}$ means the next value of the resistance in phase 2. Therefore, $R_{tl\_}1$ is the first resistance value measured by experiments in phase 2. In this model, $R_{tl\_}1$ is assumed to be independent of aging temperature to estimate the resistance at different aging temperature.

4.7 Complete Resistance Curve

This section describes the steps connecting the curves of phase 1, transition phase, and phase 2:

a. ρ_0 in Eq. 4.13 can be determined by measuring a non-degraded material, while ρ_d can be represented by the last point in phase 2 in Figure 4.1 according to experimental result.

b. The ν value corresponding to its aging temperature can be determined by fitting Eq. 4.13 to the experimental data in phase 1.

c. When ν is thermally activated, it can be represented by Eq. 4.15. It means that drop-off rate at different temperature can be predicted by Arrhenius equation.

$$\nu = \nu_0 \exp\left(\frac{-\Delta G}{RT}\right) \quad \text{Eq. 4.15}$$

$$\ln \nu = \left(\frac{-\Delta G}{R}\right)\frac{1}{T} + \ln \nu_0 \quad \text{Eq. 4.16}$$

d. Eq. 4.16 is the logarithmic form of Eq. 4.15 facilitating linear fitting. The discrete data points in Figure 4.6 can be obtained by plot the inverse of aging temperatures versus ln(ν). The solid line is linear fitting, while the dashed line is polynomial fitting.

e. The intercept and slope of the linear fitting can determine ν_0 and ΔG in Eq. 4.16.

f. With ΔG, ν_0, and Eq. 4.15, the ν corresponding to different aging temperature can be calculated.

g. Determine t_s and t_f by identifying the start and end of the transition phase shown in Figure 4.1. $V_d(t_s)$ and $V_d(t_f)$ can be calculated by Eq. 3.4.

h. With ν, ρ_0, ρ_d, $V_d(t_s)$, $V_d(t_f)$, Eq. 4.13, and Eq. 4.14 the resistance of a degraded material can be plotted as a function of time. In this model, the values of $V_d(t_s)$ and $V_d(t_f)$ are assumed to be independent of aging temperature. For example, when $V_d(t_f)$ is determined at 80℃, t_f at 100℃ can be calculated by Eq. 3.4 by plugging the V_d of 80℃ and the ν of 100℃. The ν of 100℃ can be determined by Eq. 4.15.

i. It will be shown in the section on validation that when an aging temperature is above a certain value, phase 1, the transition phase, and phase 2 become indistinguishable. Then, a resistance-versus-time curve can be modeled by only Eq. 4.13 without using the equations of the transition phase and phase 2.

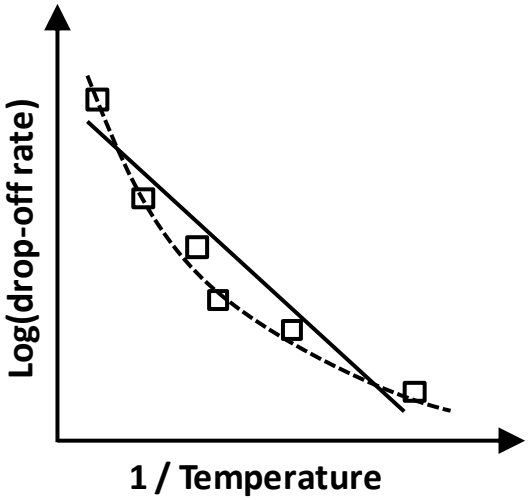

Figure 4.6 Arrhenius plot of drop-off rate

4.8 Validation of Electrical Model

Three sets of XLPE samples subject to thermal degradation are discussed in this section. They are labeled as set A [77], B [78], and C [26].

4.8.1 Case 1

The experimental data of set A samples are from the Figure 3 of reference [77]. Since the data is in the form of resistivity, it is independent of the geometry of a specimen. Therefore, this research starts with discussing the resistances of the specimens by setting that the specimens are unit cubes whose volume is one, for the simplicity of calculation. As shown by Eq. 4.4, under this condition, the values of resistance and resistivity are equal. The discrete patterns in

Figure 4.7 are experimental data [77], which can be used to determine the resistivity of non-degraded ρ_0 and degraded ρ_d XLPE in Eq. 4.13. The values are shown in Table 4.1. The values of the drop-off rates ν are tested and plugged into Eq. 4.13 to fit the experimental data and listed in Table 4.2. It is worth noting that when Eq. 4.13 is used to fit the experimental data in Figure 4.7, for the data points at 80 and 100℃, only the points in phase 1 are used, while for the data points at 120 and 140℃, all the data points in each temperature set are used.

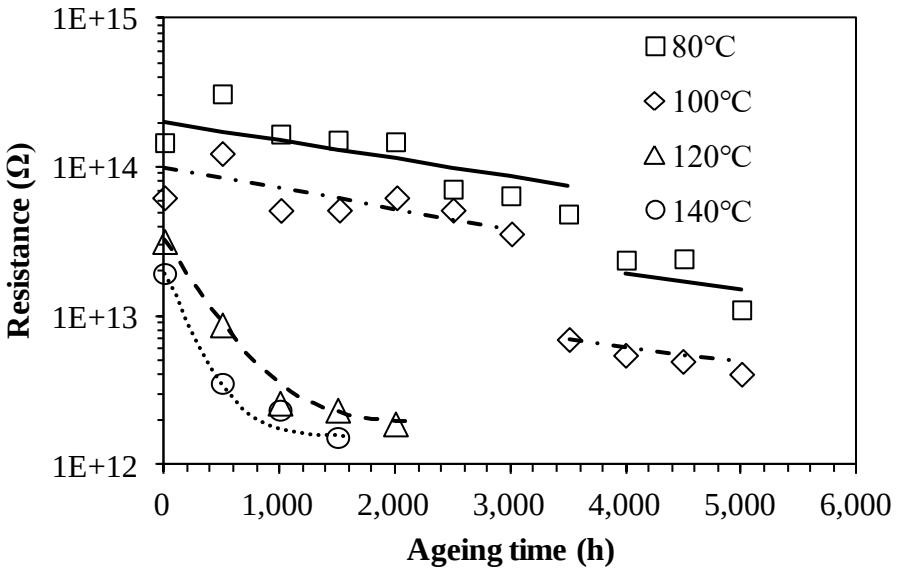

Figure 4.7 Experimental data of sample A XLPE compared with Eq. 4.13 and Eq. 4.14

Table 4.1 Parameters for Eq. 4.13

Resistivity	80℃	100℃	120℃	140℃

ρ_0	2.0E14	1.0E14	3.2E13	1.95E13
ρ_d	1.0E12	1.0E12	1.9E12	1.54E12

Table 4.2 Modeled drop-off rate of sample A XLPE

Temperature (℃)	Drop-off rate (1/h)
80	8.5E-4
100	1.0E-3
120	9.0E-3
140	1.4E-2

By using the data in Table 4.2 to plot Figure 4.8 and applying linear fitting, the slope can be used to determine the activation energy ΔG based on Eq. 4.16 where slope = $-\Delta G / R$. Here the slope is -7696; R = 8.314 J/mol-K. Therefore, ΔG = - slope × R = 64 kJ/mol, which is close to the value in a literature review [20] though different approaches are used. On the other hand, because the curve in Figure 4.8 is convex, if a second order curve fitting is applied, the slope decreases as temperature decreases. This implies that at a lower temperature, the life of the material can be overestimated if the activation energy is determined by an accelerated experiment at higher aging temperature.

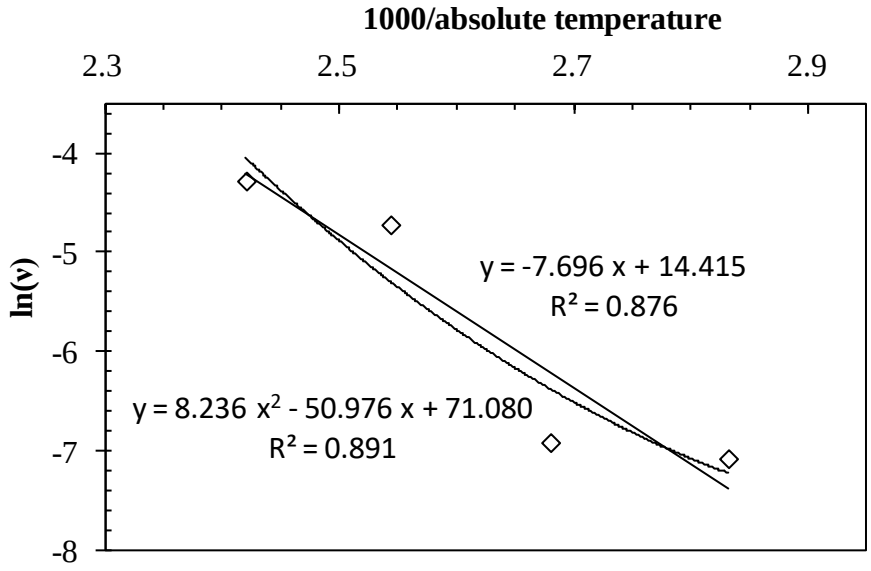

Figure 4.8 Arrhenius plot of sample A XLPE

In order to determine the timing of percolation, or the t_s and t_f of the transition phase at a certain temperature, the following steps can be applied:

a. In Figure 4.7, for 80℃ and 100℃ sample sets, the drop of the resistance starts at ~3500 and ~3000 hours, respectively, and ends at ~4000 and ~3500 hours, respectively. This determines the t_s and t_f in Figure 4.1.

b. By the corresponding ν values at 80 and 100℃ in Table 4.2 and Eq. 3.4, it can be determined that for the two aging temperature, the $V_d(t_s)$ and $V_d(t_f)$ are ~0.95 and ~0.97, respectively. $V_d(t_s)$ and $V_d(t_f)$ are assumed to be independent of temperature.

c. After the ν at a lower temperature is determined by Eq. 4.15, the start time t_s and end time t_f

of the resistance drop at that temperature can be predicted by Eq. 3.4 since the V_d and ν are known.

d. The resistance value R_{tl_1} corresponding to t_f can be determined from the first experimental data point in phase 2.

These procedures are suggested by this research to predict the life of an XLPE sample in the view of the loss of electrical resistance.

As for the model representing the decrease of the resistance in phase 2, empirically, Eq. 4.14 can be applied. Take the data sets at 80℃ for example and set R_{tl_1} at 1.9E13 ohm, R_{tl_2} becomes (1.9E13 ohm × 4000 hours / 45000 hours), which is the second value of the modeled resistance in phase 2 at 80℃ in Figure 4.7.

4.8.2 Case 2

In this case, specimens are labeled as set B. The experimental data is from Figure 5 of reference [78] and plotted by the circles in Figure 4.9. Modeled data is represented by the dash lines. In this case, the lines of phase 1 and phase 2 are overlapped with respect to time axis due to the huge undulation of the experimental result. This undulation causes uncertainty in distinguishing the boundary between phase 1 and phase 2.

As for the modeled line of phase 1, the ρ_0 and ρ_d of Eq. 4.13 in Figure 4.9 are set at 1.5E14

and 1.29E12 ohm-cm, respectively. The drop-off rate ν is determined at 1.1E-3 1//h in phase 1.

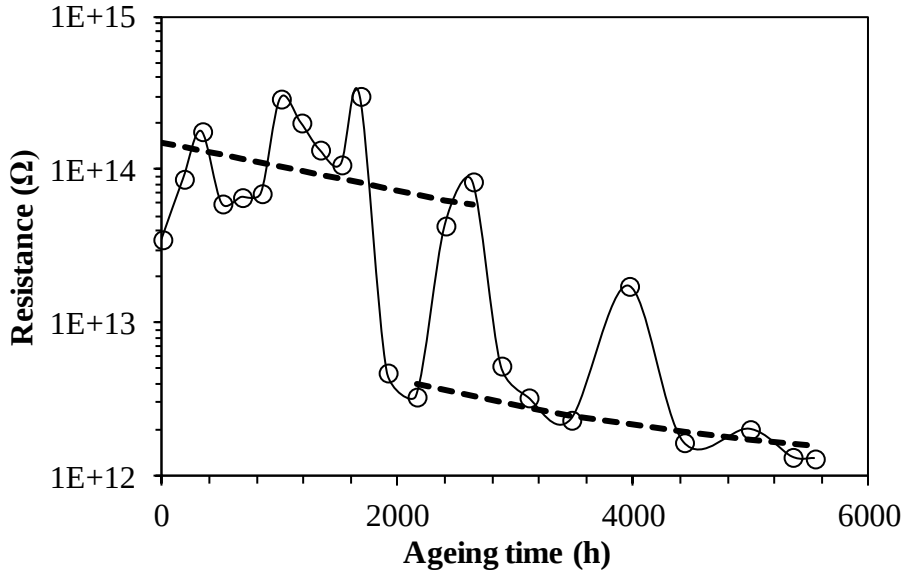

Figure 4.9 Experimental data of sample B XLPE compared with Eq. 4.13 and Eq. 4.14

For the model of phase 2, for instance, the R_{tl_1} is set at 4E12 ohm corresponding to the aging time at 2160 hours estimated by experimental data points. By Eq. 4.14, R_{tl_2} at 2405 hours becomes (4E12 ohm × 2160 hours / 2405 hours). By repeating these steps, the dashed line of phase 2 in Figure 4.9 can be plotted.

4.8.3 Case 3

In this case, specimens are labeled as set C. Experimental data is marked by discrete points in Figure 4.10 from the figure 1 of the research [26]. Despite the experimental data

which should be composed of phase 1, the transition phase, and phase 2, only Eq. 4.13 is used to model the experimental results.

The resistivity of non-degraded ρ_0 and degraded ρ_d XLPE is read from Figure 4.10 and listed in Table 4.3. The values of the drop-off rate ν are tested and plugged into Eq. 4.13 to fit the experimental data. The result is listed in Table 4.4. The values derived by Eq. 4.13 are plotted by the continuous lines in Figure 4.10.

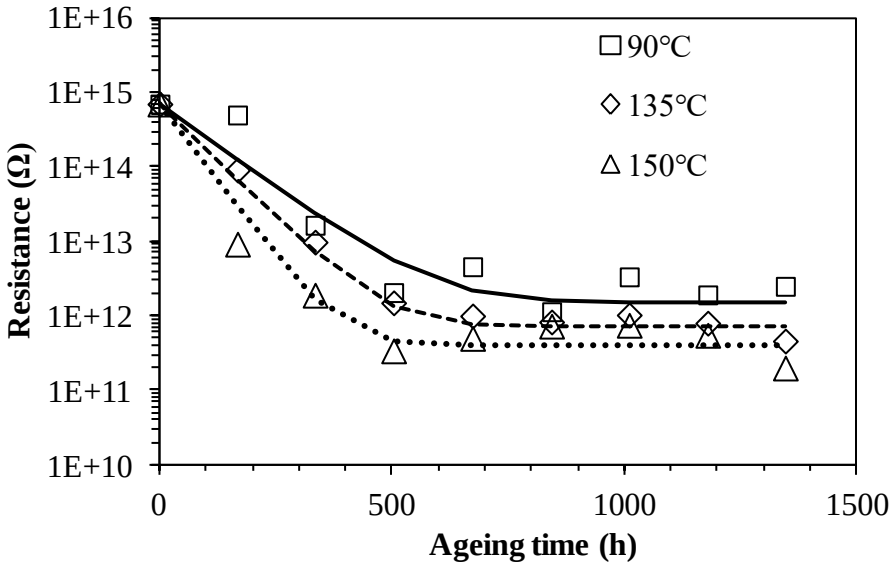

Figure 4.10 Experimental data of sample C XLPE compared with Eq. 4.13

Table 4.3 Parameters for Eq. 4.13

resistivity	90°C	135°C	150°C

ρ_0	7.0E14		
ρ_d	1.5E12	7.0E11	4.0E11

Table 4.4 Modeled drop-off rate of sample C XLPE

Temperature (℃)	Drop-off rate (1/h)
90	0.031
135	0.042
150	0.057

By using the data in Table 4.4 to plot Figure 4.11 and applying a linear fitting, the slope can be used to determine the activation energy ΔG of set C samples based on Eq. 4.16 where slope = -ΔG / R. Here, the slope is -1414. R = 8.314 J/mol-K. Therefore, ΔG is about (1414 × 8.314 = 12) kJ/mol, which is significantly lower than that of set A samples. However, this value is expected when the drop-off rate of the resistance shown in Figure 4.10 is compared with that plotted in Figure 4.7.

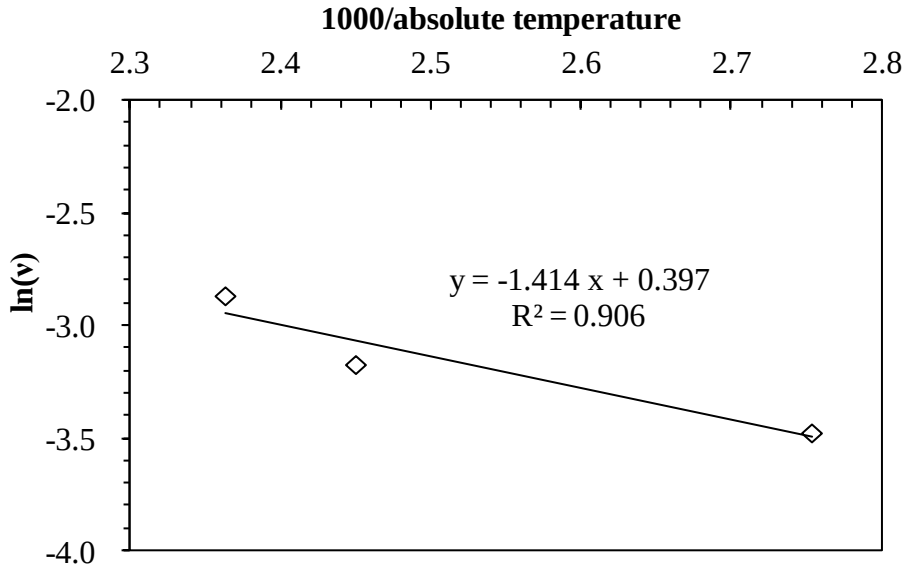

Figure 4.11 Arrhenius plot of sample C XLPE

4.9 Discussion of Electrical Degradation

Unlike the previous studies using one single resistivity value to represent the electrical degradation of a bulk XLPE [26, 77, 78], this research models a bulk material by two parts: the non-degraded and the degraded, as shown by Eq. 4.13 based on Eq. 4.15 and Eq. 3.4. This newly proposed concept quantifies the electrical degradation of XLPE in three phases whose progresses are visualized by Figure 4.3. In phase 1, it is the progress before the occurrence of percolation; electrical current uniformly flows within a specimen. Instead of considering a bulk XLPE as a whole, this model views a partially degraded specimen as a non-degraded matrix embedded with uniformly distributed subcubes which have been degraded, as shown in Figure 4.5. The novelty of this approach is that it models the amount of degraded part by Eq. 3.4 with

a kinetics approximation known as Arrhenius equation shown by Eq. 4.15. These equations become the basis of the prediction of the lifespan of XLPE cable insulation with respect to the loss of electrical resistance.

The t_s and t_f denoted in Figure 4.1 define the transition phase, which is the region between phase 1 and phase 2. It is the duration that is required to form a direct channel whose cross-section is wide enough for most of the currents to flow from one surface to the opposite surface of a specimen via the channel. At percolation, currents concentrate in the vicinity of a channel. In other words, as for the distribution of currents in XLPE, they tend to choose the direct route paved by the degraded material, whose resistivity is several orders lower than that of the non-degraded part via which currents do not flow after percolation. At the beginning of percolation, the channel is so thin that the measured resistance is the effect of the combination of the whole bulk and the thin channel. As time elapses, the cross-section of the channel is getting wider due to the further degraded material, which renders sudden drop of resistance during measurement. In other words, after the channel caused by percolation forms, the further degraded material can be viewed as “broadening” the cross-section of a channel.

In phase 2, the channel formed by degraded part is already wide enough, so most of the currents flow only via the channel. An insignificant amount of currents goes through the mixture of non-degraded and degraded parts. Further degraded material shortens the length or

widens the cross-section of a channel. This can be justified by adopting Eq. 4.4. The progress can only slowly decrease the resistance measured by a current-versus-voltage (I-V) experiment. Unlike percolation, the decrease of the electrical resistance in final phase is caused by the increase of A or the decrease of l in Eq. 4.4, while the drop of the resistance due to percolation is rendered by the formation of a channel made from another low resistivity material whose property is significantly different from the non-degraded material.

By combining the three phases discussed above, Figure 4.7 in the first case study and Figure 4.10 in the third case study can be further analyzed since multiple aging temperatures are performed in the corresponding experiments. At lower aging temperature, the resistance curve shows an obvious transition phase, which is a drop of resistance along the time axis. For example, it can be found in the 80℃ and 100℃ curves of the set A samples in Figure 4.7. Phase 1 with a smaller slope is followed by a transition phase with a steep trend, and the curve returns to a nearly horizontal slope in phase 2. On the other hand, when the aging temperature is higher, such as the 120℃ and 140℃ curves of the set A samples in Figure 4.7, or when the activation energy is lower, such as the set C samples in Figure 4.10, the resistance drop so fast in phase 1 whose resistance approaches to the value of phase 2 shortly. In these conditions, the time required to accomplish the transition phase is comparatively short and the transition phase becomes indistinguishable. In brief, the resistance trends from lower to a higher temperature

can be represented by a schematic plot shown in Figure 4.2. The curves from the top to the bottom represent the increase of an aging temperature or the decrease of activation energy. From the top to the bottom, the section of the transition phase becomes steeper and shorter and finally indistinguishable. When the transition phase shows, phase 1 and phase 2 can be represented by Eq. 4.13 and Eq. 4.14, respectively. While aging temperature is higher or activation energy is lower, Eq. 4.13 along can be used to represent the entire progress, which is plotted by the lowest solid line in Figure 4.2.

It is worth noting that all the trends of electrical degradation in this research are plotted and discussed in the unit of resistance instead of resistivity for two reasons. First, during the experiments used to measure the electrical degradation of a bulk XLPE, a current-versus-voltage plot is adopted to determine the resistance of a specimen. Therefore, the value of the resistance is a direct reading from the measurement. Second, unlike the previous studies [26, 77, 78], they considered a bulk XLPE specimen as a whole and using one single resistivity value to represent the degradation of the electrical property in average. On the contrary, in this newly proposed model, a specimen is considered degraded when the volume ratio of the degraded part relative to the whole specimen is increased. The conductivity of two different materials contributes to the trend of resistance. To be more specific, one XLPE bulk is modeled by two materials with different resistivity values, the non-degraded and degraded

parts, which are the parameters of the model but not a direct reading from the measurement. Hence, the changing of the resistance instead of resistivity is measured during experiments for estimating the degree of degradation. This approach facilitates a person to assess the electrical resistance of a bulk XLPE by connecting the yield of the degradation reaction and the degradation rate modeled by Arrhenius equation.

Besides quantifying the relation between aging temperature and electrical resistance, one of the most useful results in this research is that the value of the activation energy representing the decrease of electrical resistance can be anchored. The value of activation energy is an essential parameter in an accelerated aging experiment at a higher temperature which is used to predict a thermally activated reaction taking place at a lower temperature. The approach is by plotting Eq. 4.16 as shown in Figure 4.6, Figure 4.8, and Figure 4.11. The slope can be used to determine the activation energy. There is one point that should be emphasized: in the thermal degradation of XLPE, activation energy can be lower at a lower temperature. This makes the curve in the plot may be better fitted by a convex polynomial than a linear relation, as shown in Figure 4.6 and Figure 4.8. If this nonlinear relation is significant but ignored, the life of a material will be overestimated.

The main goal of this model is to design a method to estimate the life of XLPE cable insulation. In consideration of the resistance degradation, this research suggests that either the

start or the end of the transition phase caused by percolation can be viewed as the threshold if the resistance of phase 2 is lower than the requirement of field application.

Chapter 5: Uphill Diffusion of Antioxidant

5.1 Introduction to Uphill Diffusion

In reference [34], the measured concentration of the antioxidant during the thermal ageing is lower at the center and higher at the surface although the antioxidant diffuses outward. In other words, this paper shows the antioxidant diffuses outward against the concentration gradient. Hence, the authors of the paper stated the trend of the concentration of the antioxidant is “unexpected”, as shown in Figure 5.1 [34].

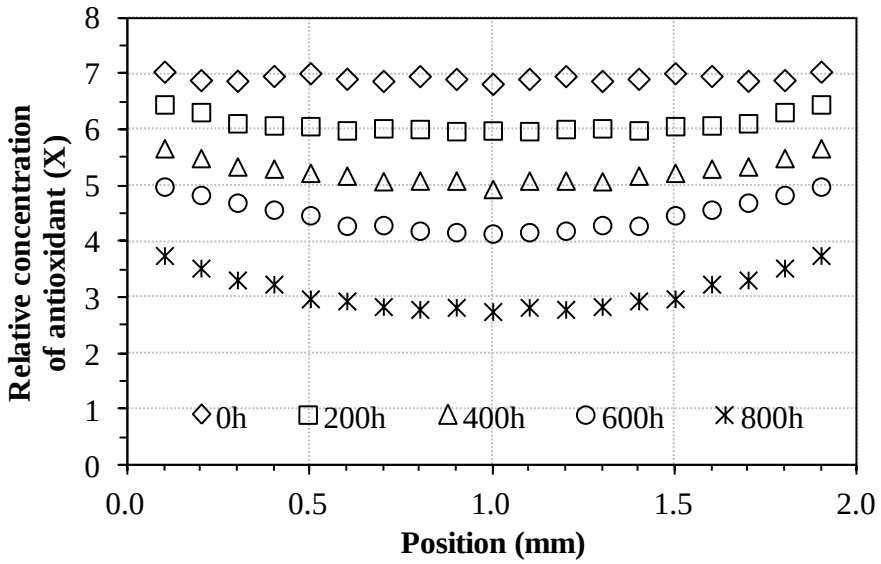

Figure 5.1 The experimental data of the relative concentration of the antioxidant (Nocrac-300) published in Figure 7 of reference [34]

Figure 5.1 shows the distribution of the antioxidant (Nocrac-300) along the cross-section

of a 2-mm thick XLPE sheet with various durations in the thermal ageing at 135℃ [34]. The distribution is convex instead of concave, which is characterized as “unexpected” by the paper [34]. In other words, the convex profile indicates the antioxidant diffuses from the center (lower concentration) to the surface (higher concentration) against the concentration gradient.

There is a specific term called uphill diffusion [98] describing this phenomenon: diffusion species moves from lower to higher concentration against the concentration gradient because the chemical potential [99] determined by activity is relatively lower at the location with higher concentration, and a matter always migrates from the position with higher activity to the location with lower activity. To understand and quantify the “unexpected” trend of the antioxidant in XLPE, the activity of the antioxidant is discussed in this research. Basing on Fick’s Law, we have developed a model to bridge the activity and the concentration of the antioxidant by introducing a dynamic activity coefficient, which is a function of oxygen concentration. Besides, this model provides an algorithm to quantify the decomposition rate of the antioxidant. It represents the decomposition ratio of an antioxidant exposed to external energy for a given period of time. With this model, the diffusion behavior and decomposition rate of the antioxidant in a bulk XLPE can be quantified.

5.2 Modeling Uphill Diffusion

To model activity coefficient as a function of oxygen concentration, first, the trend of the activity coefficient with respect to the oxygen concentration in XLPE must be established. The second step is to model the profile of the activity of the antioxidant. Third, the profile of the oxygen concentration need be formulized. The last step is finding the correlation between the activity coefficient and oxygen concentration.

5.2.1 Trend of Activity Coefficient

The concept of this model is based on the difference of activity rather than the gradient of concentration. Activity, but not solely concentration, determines the driving force making a diffusion species migrate. The relation between the activity (C_a) and the concentration (X) of the antioxidant can be represented by Eq. 5.1 [100].

$$C_a = \gamma X \qquad \text{Eq. 5.1}$$

where γ is the activity coefficient of the antioxidant.

Since the molecules of the antioxidant move from the core toward the surface and evaporate out of an XLPE specimen, the activity at the center must be higher than the activity

near the surface. In Figure 5.1, X at the surface is relatively high while the activity shall be lower. Therefore, according to Eq. 5.1, γ must be small near the surface. By the same token, the value of γ at the center shall be higher.

The physical significance of the γ represents the interaction between the antioxidant and the environment in a matrix. The concentration of oxygen is a factor making the environment inhomogeneous in a bulk XLPE. Oxygen in the air can diffuse into the bulk by diffusion. This diffusion process renders higher oxygen concentration at a sample surface [84, 85] where γ is small. On the contrary, lower oxygen concentration occurs near the core of the XLPE sample where γ shall be higher. The correlation between oxygen concentration and γ makes the major assumption of this article, which is represented by Eq. 5.2 and has been proven in the section on validation.

$$\gamma = \gamma(\text{oxygen concentration}) \qquad \text{Eq. 5.2}$$

In summary, Eq. 5.2 states γ is a function of oxygen concentration, and the decrease of γ is caused by the increase of oxygen concentration resulting from the diffusion of the oxygen in the atmosphere.

5.2.2 Profile of Antioxidant Activity

The antioxidant dissipates out of XLPE by diffusion. This suggests the profile of the activity of the antioxidant shall follow Fick's Law, which is represented by Eq. 5.3.

$$\frac{\partial C_a}{\partial t} = D_a \frac{\partial^2 C_a}{\partial x^2} \qquad \text{Eq. 5.3}$$

where t is time, D_a is the diffusivity, and x is the position on a cross-section.

Besides diffusing out of a bulk XLPE, the antioxidant can decompose due to thermal degradation. In other words, the activity of the antioxidant can be compromised by thermal ageing. Therefore, according to reaction-diffusion theory [101], Eq. 5.3 cannot pertinently represent the behavior of the antioxidant and shall be further modified into Eq. 5.4.

$$\frac{\partial C_a}{\partial t} = D_a \frac{\partial^2 C_a}{\partial x^2} - \zeta C_a \qquad \text{Eq. 5.4}$$

where ζ is the decomposition rate of the antioxidant in the unit of [1/time]. The value of ζ shall be between 0 and one.

The boundary conditions for Eq. 5.4 are: $C_a(x,0) = C_{a0}$, $C_a(0,t) = 0$, $C_a(L,t) = 0$, and $C_a(x,\infty) = 0$. C_{a0} is the initial concentration of the antioxidant. L is the thickness of a sample. By

applying separation of variables and Fourier series [84, 85], the solution of Eq. 5.4 can be represented by Eq. 5.5.

$$\mathrm{C_a(x,t)} = \frac{4\,C_{a0}}{\boldsymbol{\pi}} \sum_{j=0}^{n} \left\{ \left[\frac{1}{2\mathrm{j}+1} \sin \frac{(2j+1)\pi x}{\mathrm{L}} \right] \times \left[\exp\left(\left(-\left[\frac{(2\mathrm{j}+1)\boldsymbol{\pi}}{\mathrm{L}} \right]^2 \mathrm{D_a} - \boldsymbol{\zeta} \right) \mathrm{t} \right) \right] \right\} \qquad \text{Eq. 5.5}$$

To visualize the trend of the activity (C_a), Eq. 5.5 is plotted in Figure 5.2 where C_{a0} = 6.93, L = 2 mm, $D_a = 2.3\times10^{-13}$ m^2/s, and $\zeta = 3.4\times10^{-7}$ /s, for example.

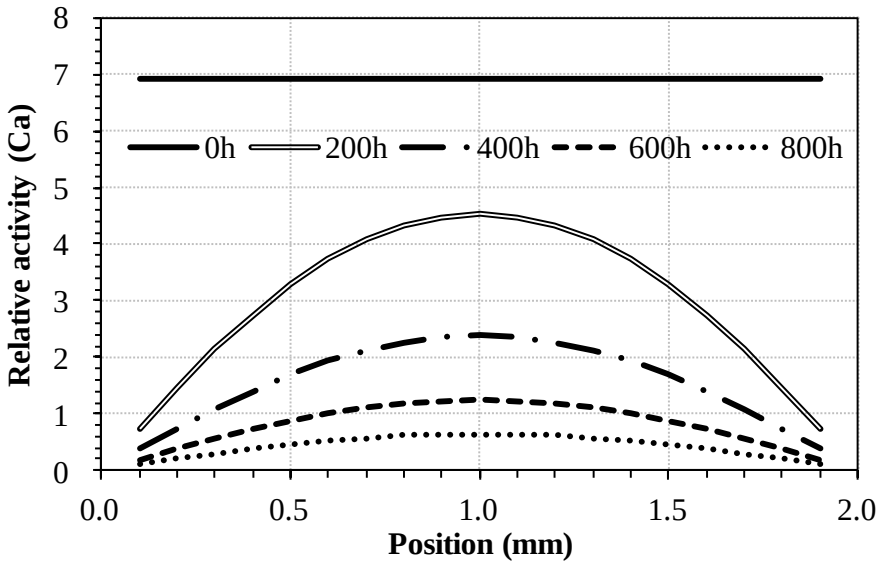

Figure 5.2 An example of the activity of the antioxidant plotted according to Eq. 5.5

5.2.3 Profile of Oxygen Concentration

The profile of the oxygen concentration in a bulk XLPE can be measured by analyzing the concentration of the carboxylic groups, or the oxidation products, [34, 57] on the cross-section of an XLPE sample. To be more specific, in the section on validation the experimental data of the oxidation products [34] shows that the profile of the oxidation products is linearly proportional to the oxygen concentration modeled by Fick's Law. In other words, the diffusion profile of oxygen modeled by Fick's Law and the concentration profile of the oxidation products are of the same trend. Experimentally, the relative concentration of the oxidation products can be measured by FTIR [34, 57]. As for the diffusion of oxygen in a bulk XLPE, Fick's Law in the form of Eq. 5.6 can represent the concentration profile of oxygen (C_x).

$$\frac{\partial C_x}{\partial t} = D_x \frac{\partial^2 C_x}{\partial x^2} \qquad \text{Eq. 5.6}$$

where D_x is the diffusivity.

The boundary conditions for Eq. 5.6 are: $C_x(x,0) = 0$, $C_x(0,t) = C_{x0}$, $C_x(L,t) = C_{x0}$, and $C_a(x,\infty) = C_{x0}$. C_{x0} is the concentration of oxygen at the surface of a sample where x = 0 or L. C_{x0} is fixed by the constant ingredient of the atmosphere. L is the thickness of a sample. By applying separation of variables and Fourier series [84, 85], the solution of Eq. 5.6 can be represented by

Eq. 5.7.

$$C_x(x,t) = C_{x0} - \frac{4\,C_{x0}}{\pi}\sum_{j=0}^{n}\left\{\left[\frac{1}{2j+1}\sin\frac{(2j+1)\pi x}{L}\right]\left[\exp\left(-\left[\frac{(2j+1)\pi}{L}\right]^2 D_x\,t\right)\right]\right\} \quad \text{Eq. 5.7}$$

In the section on validation, it has been proved that the profile plotted according to Eq. 5.7 is linearly proportional to the distribution of the oxidation products measured by FTIR.

5.2.4 Activity Coefficient Function

To solve γ function represented by Eq. 5.2, X(x,t) and $C_a(x,t)$ in Eq. 5.1 shall be determined. Applying FTIR is one method to measure X(x,t). $C_a(x,t)$ can be modeled by Eq. 5.5. Therefore, according to Eq. 5.1, γ(x,t) can be expressed by Eq. 5.8.

$$\gamma(x,t) = \frac{C_a(x,t)}{X(x,t)} \quad \text{Eq. 5.8}$$

Since the goal of this section is to prove Eq. 5.2, the oxygen concentration in the equation must be calculated. Eq. 5.7 can model the oxygen concentration in the parentheses of Eq. 5.2. Moreover, Eq. 5.7 can also be validated by using FTIR to measure the distribution of the

carboxylic groups on the cross-section of an XLPE sample [34, 57]. The reason and proof are stated in section 5.2.3 and 5.3.2, respectively. The final step is to use a Cartesian coordinate to plot the values of $\gamma(x,t)$ determined by Eq. 5.8 on the y-axis, and the corresponding values of the oxygen concentration calculated by Eq. 5.7 on the x-axis. After the value of ζ in Eq. 5.5 is determined, it can be shown that γ is a function of the oxygen concentration in XLPE but independent of time, which justifies that γ is the driving force rendering the uphill diffusion of the antioxidant. Detailed processes of these calculations have been demonstrated in the section on validation.

5.3 Validation

In this section, the experimental data used to validate our models are from a published paper [34]. The antioxidant is Nocrac-300 [34]. For the observation of the behavior of the antioxidant, the XLPE matrix is doped with the antioxidant at 1 phr under 135℃ thermal ageing for 800 hours. For the measurement of the oxidation products, the same XLPE matrix is adopted but no Nocrac-300 is added. The oxidation products had been measured after 135℃ thermal ageing for 400 hours.

5.3.1 Antioxidant Activity Profile

The activity of the antioxidant can be modeled by Eq. 5.5. In order to be consistent with Figure 7 of reference [34], C_{a0} is set at 6.93 since this value is the initial concentration (X) of the antioxidant in the figure. Then, according to Eq. 5.8, $\gamma = (C_{a0} = 6.93) \div (X = 6.93) = 1$. In other words, the maximum value of γ is one because γ decreases when oxygen concentration increases during ageing. Other initial values for γ will not alter the result of the modeling. Setting the initial value of γ at one is for the convenience of the calculation. The thickness of the XLPE sample is 2 mm. n is set at 100 for approximation. Mathematically, when j is larger than 5, the summation terms in Eq. 5.5 become indiscernible. Therefore, setting n at 100 is pertinent. As for D_a, values should be tested to make the value of C_a(1mm, 200h) calculated by Eq. 5.5 slightly less than the corresponding experimental result in Figure 7 of the paper [34] at x = 1mm and t = 200h, which is emphasized by the dotted-line circle in Figure 5.3. This is because, as shown in Figure 11 of the paper [34], oxide concentration at (x = 1mm, t = 200h) is still low. Therefore, it can be assumed that the value of γ in Eq. 5.1 is only slightly less than 1 since the oxygen concentration at the center is still relatively low at the beginning of the experiment. In other words, the activity of antioxidant has not been compromised too much at the center of the cross-section when the concentration of oxygen is still low. To visualize this approach, Figure 5.3 shows the lines plotted according to Eq. 5.5. In this condition, $\mathbf{D_a}$ in Eq.

5.5 has been determined to be 2.3×10^{-13} m^2/s. ζ is tentatively set at 0 and will be corrected later. $\gamma(x,t)$ can be calculated by Eq. 5.8 based on the values of $C_a(x,t)$ and $X(x,t)$ read from Figure 5.3.

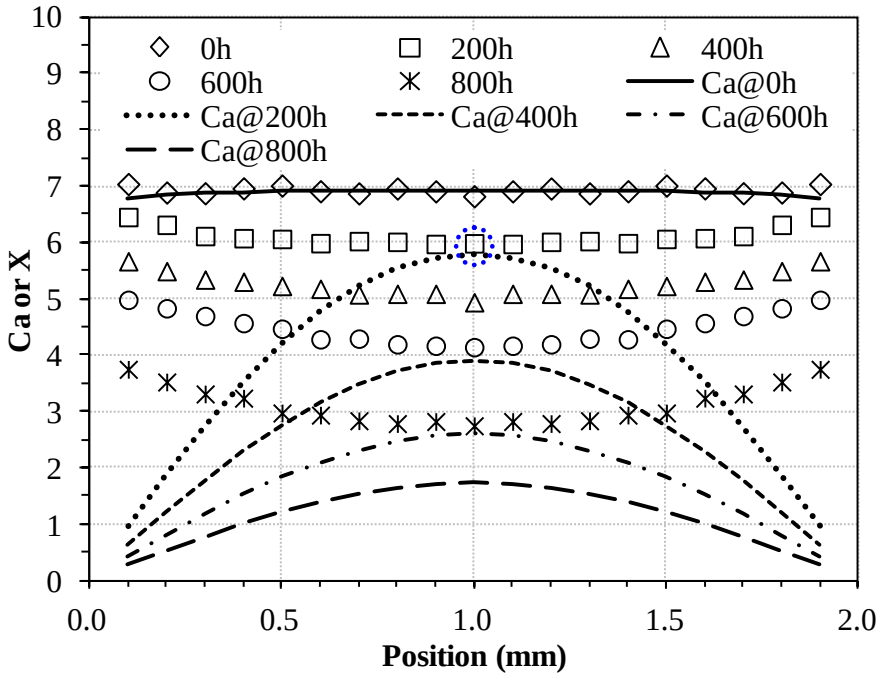

Figure 5.3 Continuous lines: modeled activity plotted according to Eq. 5.5. Discrete patterns: the concentration of the antioxidant measured by FTIR [34]

5.3.2 Profile of Oxygen Concentration

The functional form of $\gamma(x,t)$ was determined in Section 5.3.1. To find the correlation between γ and oxygen concentration, Eq. 5.7 can be applied to quantify the oxygen concentration. The discrete patterns in Figure 5.4 are the experimental data of the distribution

of the oxidation products in the XLPE sample measured by FTIR [34]. The concentration of the oxidation products measured by FTIR is not equal to the concentration of the oxygen modeled by Eq. 5.7. However, continuous lines plotted according to Eq. 5.7 can fit the experimental data denoted by the discrete patterns shown in Figure 5.4. This result means the concentration of the oxidation products is linearly proportional to the concentration of the oxygen diffusing in a bulk XLPE. In other words, in the XLPE where the antioxidant is deficient, the oxidation reaction is controlled by the diffusion kinetics of the oxygen migrating from the atmosphere into the core of the sample.

The thickness (L) in Eq. 5.7 is 2 mm. The value of the extrapolation of the experimental data at x = 0 mm and x = 2.0 mm in Figure 5.4 is 5. To be consistent with the experimental data, C_{x0} in Eq. 5.7 is set at 5. Setting C_{x0} at 5 is only for the convenience of the calculation. C_{x0} at different values do not alter the trend of Eq. 5.7 since it is a proportional constant in the equation. When j in the equation is larger than 5, the summation terms are too small to be discernible. Hence, setting n at 100 is pertinent for the approximation. After testing different values of D_x, continuous lines plotted according to Eq. 5.7 with $\mathbf{D_x}$ at 2.28×10^{-13} m^2/s can properly fit the experimental data denoted by the discrete patterns shown in Figure 5.4.

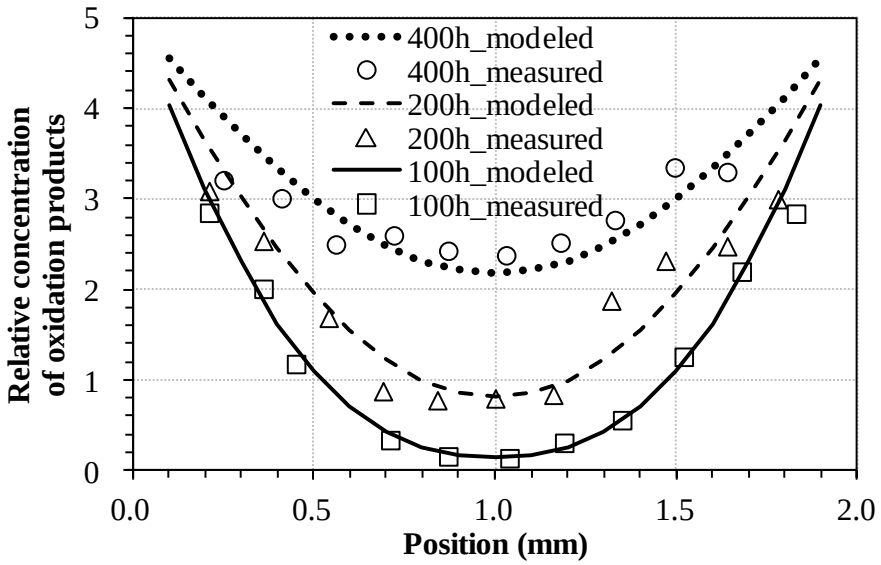

Figure 5.4 Continuous lines: modeled data plotted according to Eq. 5.7. Discrete patterns: the experimental data from Figure 11 of reference [34] (Specimens with no antioxidant at 135℃ thermal ageing)

5.3.3 Activity Coefficient Function

Section 5.3.1 determined the values of $\gamma(x,t)$. Section 5.3.2 quantified $C_x(x,t)$ on the cross-section of the bulk XLPE. This section correlates γ with C_x by starting with the linear fitting in Figure 5.5.

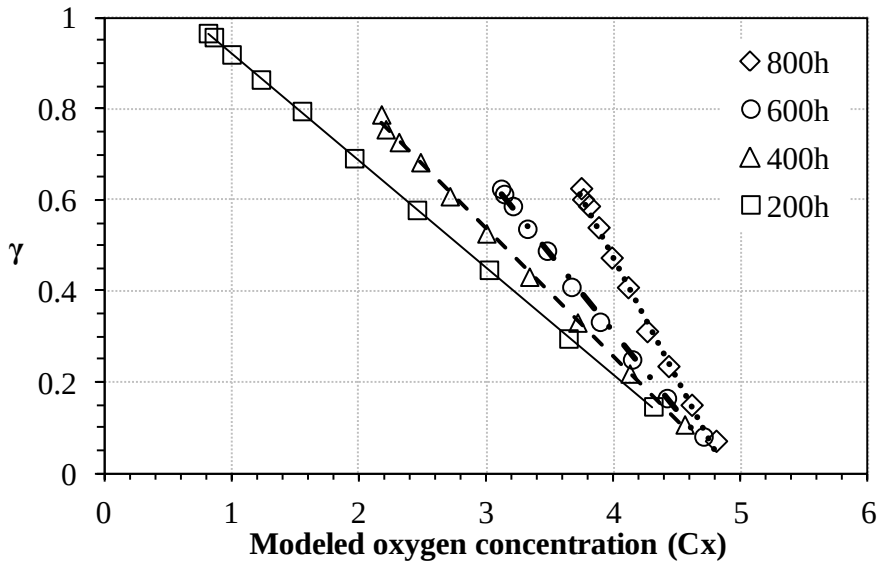

Figure 5.5 The correlation between activity coefficient (γ) and modeled oxygen concentration (C_x) before the decomposition rate (ζ) is anchored

Four sets of experimental data are plotted with respect to different ageing time in Figure 5.5. Linear fitting has been applied to each data set. The coefficients, a and b, of the linear functions representing the straight lines in Figure 5.5 are listed in Table 5.1. The R^2 of each linear fitting is also shown in the table. High values of R^2 suggest a strong correlation between γ with C_x. Negative slopes of the linear functions indicate the activity coefficient of the antioxidant decreases when the oxygen concentration increases. However, Figure 5.5 reflects γ is a function of oxygen concentration and time, which does not conform to the preliminary: γ is a function of only oxygen concentration. This is because the value of ζ in Eq. 5.5 has not been determined. In other words, all the previous calculation has tentatively set $\zeta = 0$.

Table 5.1 The coefficients, a and b, of the linear equation: y = a · x + b corresponding to each straight line in Figure 5.5

Aging time (h)	a	b	R^2
200	-0.2350	1.1564	0.9999
400	-0.2815	1.3802	0.9985
600	-0.3451	1.6890	0.9973
800	-0.5295	2.5926	0.9953

To determine the correct ζ value, a γ-C_x plot similar to Figure 5.5 shall be plotted. However, different from Figure 5.5, all the discrete points (squares, triangles, circles, and rhombuses) in Figure 5.5 are combined into one data set shown in Figure 5.6(b) ~ (d) where different ζ values from 0 to 1 are plugged into Eq. 5.5 to determine the corresponding γ calculated by Eq. 5.8. In each new γ-C_x plot such as Figure 5.6(b), one linear fitting is applied to all the points in order to obtain an R^2 value. Each ζ value corresponds to one R^2 value, which is shown in Figure 5.6(a). When $\zeta = 3.2 \times 10^{-7}$ /sec, the highest R^2 value is located, which is shown in Figure 5.6(c). In this condition, γ as a function of oxygen concentration is represented by Eq. 5.9.

$$\gamma = -0.18398\, C_X + 0.90287 \qquad R^2 = 0.99341 \qquad \text{Eq. 5.9}$$

This result directly concludes that the activity coefficient (γ) is linearly proportional to the oxygen concentration (C_x) with a negative slope. Hence, Eq. 5.2 has been solved and can be rewritten as Eq. 5.9.

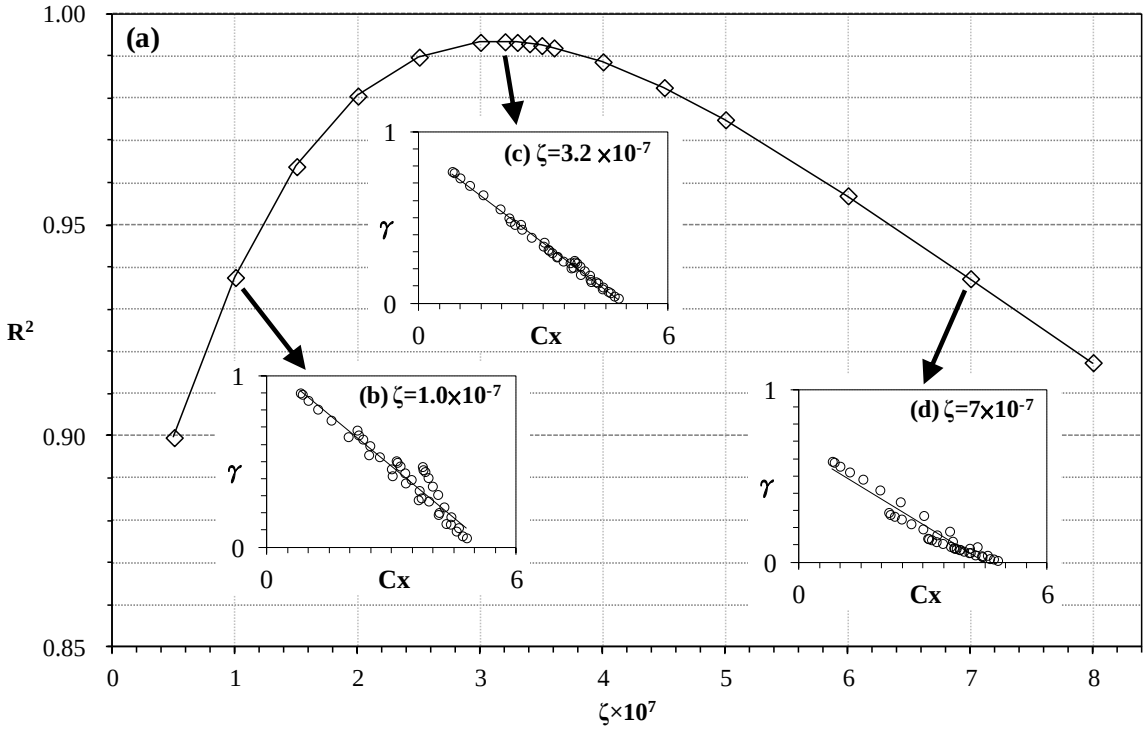

Figure 5.6 Testing different ζ values to maximize R^2

5.4 Discussion

The experimental data shown in Figure 5.1 indicate that the amount of the antioxidant decreases when the XLPE matrix is under thermal ageing. There are at least two root causes:

the diffusion of the antioxidant molecules and the decomposition of the antioxidant. Diffusion makes the antioxidant migrate from the center to the surface of the matrix, and dissipate in the air. On the other hand, the antioxidant molecule can decompose; the decomposed molecule may react with a substance in the matrix, such as oxygen inducing oxidation. Either diffusion or decomposition makes FTIR detect less antioxidant left in the XLPE matrix.

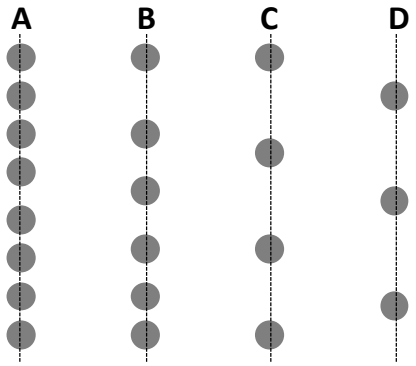

Figure 5.7 Illustration of 1-D diffusion mechanism

Diffusion kinetics can be modeled by Fick's Law. At the very beginning of the derivation of 1-D Fick's Law, diffusion species can be represented by the dots in Figure 5.7 [74]. The lines in the figure mean planes whose normals are perpendicular to the normal of this paper. If each dot has the same probability to migrate from one plane to the adjacent planes, the net flux of the dots shall be from plane A to plane D since the concentration of the dots is higher in plane A and decreases from plane A to plane D. This process renders

diffusion from high to low concentration. In other words, diffusion goes from the left to the right of Figure 5.7. However, this diffusion direction is certain only when the matrix is homogeneous, or the jumping probability of each dot is the same. In other words, if the jumping probability of the dots in plane D is high and gradually decreases from plane D to plane A, the net flux of diffusion may become from the right to the left, which is termed uphill diffusion [98]: diffusion from low to high concentration.

The physical significance of the jumping probability means the interaction between the diffusing species and the matrix. From the energy viewpoint, when the dots in plane A of Figure 5.7 are stable, the jumping frequency of the dots shall be low. For instance, if the density of certain defects is high in plane A and decreases from plane A to plane D, diffusing species may move from the right to the left. This is a very common phenomenon in material science since a defect always provides a site with a lower energy state.

In thermodynamics, one way to quantify the jumping probability is to introduce the concept of activity. Activity can be regarded as “effective” concentration. As shown in Eq. 5.1 [100], activity (C_a) is based on the concentration (X) and modified by activity coefficient (γ). The role of γ is to determine the “effective” concentration contributing to the change of Gibbs free energy. In other words, while the dots in plane A of Figure 5.7 are trapped by the high density of certain defects, it renders low jumping probability to the dots, which means the

“effective” concentration of the dots in plane A is low. Fewer dots per unit time can migrate away from plane A and contribute to the diffusion.

To extend the concept of Figure 5.7 to Figure 5.1, the migration of the dots can be regarded as the diffusion of the antioxidant in the XLPE matrix. In Figure 5.7, plane A is like the location near the surface while plane D is analogous to the position at the core of the XLPE sample corresponding to Figure 5.1. The concentration of the dots (representing the antioxidant molecules) in plane A is higher than the concentration in plane D. Although the concentration of the antioxidant is higher near plane A and decreases from plane A to plane D, the net flux of the antioxidant can still flow from plane D to plane A against concentration gradient as long as the concentration of oxygen in plane A is higher. This is because oxygen can lower the jumping probability of the antioxidant molecule. In other words, the activity of the antioxidant near the surface is significantly compromised by the molecules of the diffusing oxygen from the air. In other words, the antioxidant near oxygen has a lower energy state compared to the antioxidant far from an oxygen molecule. This correlation is formulized by Eq. 5.2 and quantified by Eq. 5.9. Based on the concept of activity derived from the migration behavior of a diffusing species, the nominators of Fick’s Law represented by Eq. 5.2 have been denoted by activity (C_a) instead of solely concentration, which means the “effective” concentration shall be considered.

Besides diffusion driven by activity, the loss of the antioxidant can also result from the decomposition of the antioxidant itself. The ageing temperature discussed in this study is 135℃. The melting temperature of the antioxidant is 150 - 165℃. Hence, the molecular chains in the antioxidant can decompose and react with oxygen, XLPE, or other species in the environment. Therefore, Eq. 5.3 shall be modified by the reaction-diffusion theory represented by Eq. 5.4 [101]. The value of ζ in Eq. 5.4 has been determined at 3.2×10^{-7} /sec in section 5.3.3. It means in every second, ζ portion of the antioxidant decomposes. Without diffusion, the amount of the decomposition ratio (V_d) in the first 100 hours can be calculated by Eq. 5.10 [86].

$$V_d = 1 - e^{-\zeta t} \qquad \text{Eq. 5.10}$$

where $t = 100 \times 60 \times 60$ seconds.

Eq. 5.10 means in the first 100 hours, if there is no diffusion, 11% of the original antioxidant is decomposed due to the thermal ageing. When both the diffusion and the decomposition contribute to the loss of the activity of the antioxidant, the accumulating loss of the activity can be determined by integrating Eq. 5.5, the solution of Eq. 5.4.

In Section 5.2.3 and 5.3.2, we have shown that the concentration of the oxidation

products is linearly proportional to the diffusion profile represented by Eq. 5.7, which is the solution of Fick's Law expressed by Eq. 5.6. In this study, the diffusion species of Eq. 5.6 is assumed to be oxygen although other diffusion species can be modeled by this equation as well. However, since oxygen is an essential reactant in oxidation reactions and oxygen can be constantly supplied from the atmosphere, the assumption based on the diffusing oxygen shall be pertinent.

The main objective of this chapter is quantifying the uphill diffusion of the antioxidant based on the activity. The activity is determined by the activity coefficient (γ), which has been shown to be linearly proportional to the oxygen concentration with a negative slope. This correlation means when the antioxidant and oxygen are spatially close to each other, their total energy becomes lower. A study provided a result conforming to our research. According to reference [33] reported, in the vicinity of the antioxidant molecule, the probability of the oxidation reaction caused by oxygen and the polymer matrix decreases. This may suggest that the antioxidant can increase the total energy between oxygen and the polymer, or, on the other hand, the energy between oxygen and the antioxidant is lower than the energy between oxygen and the polymer. In other words, the antioxidant is competing with the polymer in order to attract oxygen. Moreover, the antioxidant has been reported to spontaneously oxidize [102] and combustible [103] in the air, which means the antioxidant

tends to attract oxygen. This is evidence indicating that the activity of the antioxidant decreases when oxygen presents.

Chapter 6: Summary and Conclusion

Predictive models as functions of time, temperature, and dose rate are important for power plants to estimate the lifespan of cable insulations. However, to the best of our knowledge, a model with these variables had not been developed before this dissertation. To tackle this issue, three approaches have been taken in this research to quantify the degradation of cable insulation. Experimental data have been incorporated to validate the developed models.

6.1 Chemical Degradation

Physics-based equations derived from the degradation mechanisms serve as the base of the models representing mechanical and electrical degradation. The mechanisms are categorized into reaction-controlled and diffusion-controlled kinetics, which are homogeneous and inhomogeneous degradation, respectively. In reaction-controlled degradation, the virtual degradation ratio is the integral of the virtual degradation rate; the concept is the same as the CDF of an exponential distribution. In diffusion-controlled degradation, the oxidation reaction is used to represent the trend of degradation; the virtual degradation ratio is proportional to the integral of the diffusion profile of oxygen migrating in a bulk material. The diffusion profile is controlled by diffusivity, which determines the virtual

degradation ratio. Both the virtual degradation rate in reaction control and the diffusivity in diffusion control are temperature-dependent on Arrhenius equation facilitating the prediction of mechanical and electrical degradation at different temperatures. Moreover, the virtual degradation rate is further related to dose rate, which extends the prediction from temperature domain to radiation domain.

The loss of the antioxidant in XLPE can accelerate the degradation caused by the oxidation. One the one hand, the loss of the antioxidant is driven by uphill diffusion. Uphill diffusion is caused by the unevenly distributed activity coefficient in the matrix. The coefficient is linearly proportional to the oxygen concentration with a negative slope. On the other hand, the loss of the antioxidant results from the decomposition of the antioxidant itself. A reaction-diffusion theory is used to model the profile and the amount of the antioxidant left in an XLPE matrix.

6.2 Mechanical Degradation

On a linear Cartesian coordinate, the experimental data of the EAB as a function of time is similar to an S shape, which is modeled by two parts: a period of insignificant decrease followed by a section with a gradually subsiding slope. The period is modeled by incubation time (τ_0). The section is modeled by an equation with a parameter: drop-off rate (ν). The

equation is derived from a physics-based approach dichotomizing one material into two parts: virtually degraded and virtually fresh subcubes. The ratio of the degraded subcubes can be used to model the EAB both in reaction- and diffusion-controlled degradation.

Unlike the TDD approach, the shape of the EAB curve in this model is flexible. In other words, there is no shift factor framing a curve in this newly-proposed method. The model can fit both temperature- and radiation-dominated conditions since no assumption is made corresponding to reaction types. There are only two parameters, τ_0 and ν, in the model. The simplicity makes this model practical in the filed applications. τ_0 and ν are of physical significance and their trends are related to aging temperature and dose rate. Therefore, by following the trends among τ_0, ν, aging temperature, and dose rate, three-dimensional figures are plotted to establish a predictive model representing the EAB as a function of time, which can predict the remaining life of cable insulation.

Bayesian parameter estimation is applied to convert the deterministic model into the probabilistic model addressing primarily the uncertainty of drop-off rate, which renders the distribution of expected lifespan. Therefore, the degradation of cable insulation can be represented in the probabilistic form. This aspect of our model is also new.

6.3 Electrical Degradation

In additional to being applied to mechanical degradation, Dichotomy Model can represent the electrical degradation of cable insulation. The degradation of the resistance can be divided into three phases: phase 1 with a uniform current, transition phase caused by percolation, and phase 2 paved by the degraded part whose resistivity is much lower than that of the non-degraded part. Phase 1 is modeled by the Dichotomy Model. Transition phase and phase 2 are empirically calculated.

Either at lower or higher temperature, the curve of phase 1 can be used to determine the drop-off rate and activation energy affecting the decrease of the resistance. This approach offers an advantage since the activation energy is an essential factor in Arrhenius equation, which is a method widely used to predict the life of a material from an accelerated aging experiment.

At lower aging temperature or higher activation energy, the transition phase is longer and can be discerned. Three phases of the resistance degradation are discrete. However, in the opposite conditions, the curves of the transition phase and phase 2 are not much different compared to the data point calculated by the equation of phase 1. Therefore, at high temperature or low activation energy, the equation of phase 1 can model the entire degradation progress.

6.4 Degradation Portfolio

Three aspects are considered in this research to quantify the degradation of cable insulation. In the field application, the accumulated virtual degradation ratio of each category can be simultaneously monitored along a time axis by the corresponding model. Once one of the ratios exceeds its threshold, an alarm shall be triggered at discretion.

6.5 Future Work

According to the chemical degradation model, the increase of degradation ratio is calculated by the CDF of an exponential distribution or the diffusion profile. Other kinetics such as linear degradation has not been considered. Dichotomy Model may be compatible with different reaction kinetics as long as the environmental conditions are given.

As for the mechanical degradation model, besides EAB, strength is another important physical property of the structural materials such as aviation. However, limited research and experimental data have been published addressing the tensile strength, yield strength, or Young's Modulus of a polymer in relation to degradation. Dichotomy Model may also be pertinent to the development of such models.

The theories of the homogeneous degradation and percolation in the electrical

degradation model may be used to quantify the degradation of the polymer in electronic packaging. Homogeneous degradation can be used to represent the change of the dielectric properties of the package. Percolation is another major phenomenon rendering the diffusion of moisture. Since Dichotomy Model is generic, it may be applicable to the prediction of the degradation of electronic devices, particularly in space applications.

Appendix

A. Introduction of Exponential Distribution

Since an exponential distribution is used in this dissertation to construct one of the major parts of the degradation models, a detailed derivation of the distribution from a very fundamental aspect is introduced in this section. It starts from a geometric distribution, which serves as the beginning of the derivation of an exponential distribution.

A.1 Geometric Distribution

Let Y be the random variable of a geometric distribution [104]. There are n' trials. The result of the next trial is not affected by the previous trials; In other words, each test is a lack of memory. For each trial, the success and the failure probabilities are p' and (1-p'), respectively. The probability of the occurrence of the first success after n' trials can be represented by Eq. a. 1, which is a function of a discrete random variable.

$$P(Y = n') = p' \cdot (1 - p')^{(n'-1)} \qquad \text{Eq. a. 1}$$

A.2 Exponential Distribution

Exponential distribution has a continuous probability distribution function (PDF), which

can be derived from geometric distribution. In other words, as n' in Eq. a. 1 approaches infinity, geometric distribution becomes exponential distribution. The following is the derivation process.

Assume an event can occur in every hour with a probability λ. Here the unit "hour" is chosen in order to be in accordance with the experimental data of this dissertation. Other time units are certainly applicable. If one hour is divided into n parts where n is a very large non-zero integer, the probability of the occurrence of the event p in this very small time interval can be represented by Eq. a. 2.

$$p = \frac{\lambda}{n} \qquad \text{Eq. a. 2}$$

Let X be the random variable of an exponential distribution with a parameter λ. Let Y be the random variable of a geometric distribution with a parameter (λ/n). After b hours, the probability of the occurrence of an event can be represented by Eq. a. 3.

$$P(X \leq b) \approx P(Y \leq b \cdot n) \qquad \text{Eq. a. 3}$$

In order to calculate the right-hand side of Eq. a. 3, the summation algorithm in Eq. a. 4 is

introduced.

$$P(Y \leq b \cdot n) = \sum_{k=1}^{b \cdot n} P(Y = k) \qquad \text{Eq. a. 4}$$

Plug the p in Eq. a. 2 into the p' in Eq. a. 1; then plug the result into Eq. a. 3 and Eq. a. 4. These steps can result in Eq. a. 5 and Eq. a. 6.

$$P(Y \leq b \cdot n) = \sum_{k=1}^{b \cdot n} \left(1 - \frac{\lambda}{n}\right)^{k-1} \cdot \frac{\lambda}{n} \qquad \text{Eq. a. 5}$$

$$= \frac{\lambda}{n} \cdot \sum_{k=0}^{b \cdot n - 1} \left(1 - \frac{\lambda}{n}\right)^{k} \qquad \text{Eq. a. 6}$$

The summation algorithm in Eq. a. 6 is a typical form of the summation of a geometric progression, which can be calculated by Eq. a. 7, whose parameters can be substituted by Eq. a. 8 and Eq. a. 9 in order to be in accordance with Eq. a. 6.

$$\sum_{k=0}^{m} a^k = \frac{1 - a^{m+1}}{1 - a} \qquad \text{Eq. a. 7}$$

$$m = b \cdot n - 1 \qquad \text{Eq. a. 8}$$

$$a = (1 - \frac{\lambda}{n})$$ Eq. a. 9

The equations above can lead to Eq. a. 10, Eq. a. 11, and Eq. a. 12.

$$P(Y \leq b \cdot n) = \frac{\lambda}{n} \cdot \frac{1 - (1 - \frac{\lambda}{n})^{m+1}}{1 - (1 - \frac{\lambda}{n})}$$ Eq. a. 10

$$P(Y \leq b \cdot n) = \frac{\lambda}{n} \cdot \frac{1 - (1 - \frac{\lambda}{n})^{b \cdot n}}{1 - (1 - \frac{\lambda}{n})}$$ Eq. a. 11

$$= 1 - (1 - \frac{\lambda}{n})^{b \cdot n}$$

$$= 1 - \left[(1 - \frac{\lambda}{n})^{n} \right]^{b}$$ Eq. a. 12

By the bridge provided by Eq. a. 3, Eq. a. 12 can be approximated to Eq. a. 13.

$$P(X \leq b) \approx 1 - \left[(1 - \frac{\lambda}{n})^{n} \right]^{b}$$ Eq. a. 13

Since the n in Eq. a. 13 is a very large integer, which means the time interval is very small, the concept of limitation algorithm can be introduced to Eq. a. 13, so Eq. a. 14 and Eq. a. 15 can be obtained.

$$P(X \leq b) = \lim_{n\to\infty} \left\{ 1 - \left[(1 - \frac{\lambda}{n})^n \right]^b \right\} \quad \text{Eq. a. 14}$$

$$= 1 - \left\{ \lim_{n\to\infty} \left[(1 - \frac{\lambda}{n})^n \right] \right\}^b$$

$$= 1 - \left(e^{-\lambda} \right)^b$$

$$= 1 - e^{-\lambda \cdot b} \quad \text{Eq. a. 15}$$

Finally, the cumulative distribution function (CDF) of an exponential distribution is shown by Eq. a. 15 [86]. Followed by the steps from Eq. a. 16 to Eq. a. 19, and by the premise that no event occurs when the time is not larger than zero, Eq. a. 20 can be obtained.

$$P(X \leq b) = \int_{-\infty}^{b} f_X(x)\, dx \quad \text{Eq. a. 16}$$

$$P(X \leq b) = \int_{0}^{b} f_X(x)\, dx \quad \text{Eq. a. 17}$$

$$\frac{d}{db} P(X \leq b) = \frac{d}{db} \int_{0}^{b} f_X(x)\, dx \quad \text{Eq. a. 18}$$

$$\frac{d}{db} P(X \leq b) = \frac{d}{db} \left(1 - e^{-\lambda \cdot b} \right) \quad \text{Eq. a. 19}$$

$$f_X(b) = \lambda \cdot e^{-\lambda \cdot b} \quad \text{Eq. a. 20}$$

Eq. a. 20 is the PDF of an exponential distribution [86], which is the final goal of the derivation in this section.

Reference

[1] P. Voosen. (2009). *How Long Can a Nuclear Reactor Last?* Available: https://www.scientificamerican.com/article/nuclear-power-plant-aging-reactor-replacement-/

[2] J. N. Crawford. (2015). *Aging U.S. Nuclear Plants Pushing Limits of Life Expectancy*. Available: http://www.insurancejournal.com/news/national/2015/11/29/390222.htm

[3] W. D. Callister and D. G. Rethwisch, *Materials science and engineering: an introduction*, 7 ed. 605 Third Avenue, New York, NY 10158-0012: John Wiley & Sons, Inc., 2007.

[4] NEI. (2016). *US Nuclear Generating Statistics*. Available: https://www.nei.org/Knowledge-Center/Nuclear-Statistics/US-Nuclear-Power-Plants/US-Nuclear-Generating-Statistics

[5] IAEA. (2016). *Nuclear Share of Electricity Generation in 2015*. Available: https://www.iaea.org/PRIS/WorldStatistics/NuclearShareofElectricityGeneration.aspx

[6] IAEA, "Assessment and management of ageing of major nuclear power plant components important to safety: In-containment instrumentation and control cables Volume I," International Atomic Energy Agency, Vienna, Austria IAEA-TECDOC-1188, December 2000.

[7] EPRI and G. Toman, "Initial Acceptance Criteria Concepts and Data for Assessing Longevity of Low-Voltage Cable Insulations and Jackets," Electric Power Research Institute, Charlotte, North Carolina 1008211, March 2005.

[8] L. Bustard and P. Holzman, "Low-voltage environmentally-qualified cable license renewal industry report: Revision 1. Final report," Electric Power Research Institute, Palo Alto, CA. USA TR-103841, July 1994.

[9] S. Dalal, R. S. Gorur, and M. L. Dyer, "Aging of distribution cables in service and its simulation in the laboratory," *IEEE transactions on dielectrics and electrical insulation*, vol. 12, pp. 139-146, 2005.

[10] C. Kim, Z. Jin, P. Jiang, Z. Zhu, and G. Wang, "Investigation of dielectric behavior of thermally aged XLPE cable in the high-frequency range," *Polymer testing*, vol. 25, pp. 553-561, 2006.

[11] F. Lim and R. Fleming, "The temperature dependence of space charge accumulation and DC current in XLPE power cable insulation," in *Electrical Insulation and Dielectric Phenomena, 1999 Annual Report Conference on*, 1999, pp. 66-69.

[12] M. Shwehdi, M. Morsy, and A. Abugurain, "Thermal aging tests on XLPE and PVC

cable insulation materials of Saudi Arabia," in *Electrical Insulation and Dielectric Phenomena, 2003. Annual Report. Conference on*, 2003, pp. 176-180.

[13] L. Cao and S. Grzybowski, "Life-time characteristics of EPR cable insulation under electrical and thermal stresses," in *2013 IEEE International Conference on Solid Dielectrics (ICSD)*, 2013, pp. 632-635.

[14] P. L. Cinquemani, F. L. Kuchta, M. M. Rahman, F. Ruffinazzi, and A. Zaopo, "105°C/140°C rated EPR insulated power cables," *IEEE transactions on power delivery*, vol. 11, pp. 31-42, 1996.

[15] OMNI. (2017). *Medium Voltage Power Cable: EPR Insulation - PVC Jacket*. Available: http://www.omnicable.com/spec-sheets/15kv-shielded-eprpvc-133-insulation-medium-voltage-power-cable-15-kv.html

[16] T. A. Short, *Electric Power Distribution Handbook*, 2 ed. Boca Raton, FL: CRC Press, 2014.

[17] (2017). *Silicone Cable*. Available: http://silicone.co.uk/products/silicone-cable/

[18] IEWC. (2017). *Technical Guide - Popular Insulation Types*. Available: http://www.iewc.com/resources/technical-guide/popular-insulation-types

[19] O. Keski-Rahkonen, J. Björkman, and J. Farin, *Derating of cables at high temperatures*, 2 ed. Vuorimiehentie 3, P.O. Box 1000, FI-02044 VTT, Finland: Valtion teknillinen tutkimuskeskus (VTT), 2008.

[20] T. Yamamoto and T. Minakawa, "The final report of the project of assessment of cable aging for nuclear power plants," Japan Nuclear Energy Safety Organization, Tokyo, Japan JNES-SS-0903, July 2009.

[21] IEEE, "IEEE Recommended Practices and Requirements for Harmonic Control in Electrical Power Systems," in *519-1992*, ed. 345 East 47th Street, New York, NY 10017-2394: The Institute of Electrical and Electronics Engineers, Inc., 2004.

[22] EPRI and G. Toman, "Plant Support Engineering: Aging Management Program Development Guidance for AC and DC Low-Voltage Power Cable Systems for Nuclear Power Plants, Final Report," Electric Power Research Institute, 1300 West W.T. Harris Blvd. Charlotte, NC 28262 1020804, June 2010.

[23] ANSI, "Voltage Rating for Electric Power Systems and Equipment," in *ANSI C84.1-1989*, ed. 1300 North 17th Street, Suite 900, Rosslyn, Virginia 22209: National Electrical Manufacturers Association, 1989.

[24] T. Yamamoto, "The interim report of the project of assessment of cable aging for nuclear power plants," Japan Nuclear Energy Safety Organization, Tokyo, Japan JNES-SS-0619, December 2006.

[25] N. Hampton, R. Hartlein, H. Lennartsson, H. Orton, and R. Ramachandran,

"Long-life XLPE insulated power cable," presented at the Jicable, Paris-Versailles, France, 2007.

[26] Y. Mecheri, S. Bouazabia, A. Boubakeur, and M. Lallouani, "Effect of thermal Ageing on the Properties of XLPE as an Insulating Material for HV Cables," presented at the International Electrical Insulation Conference, IET Centre, Birmingham, UK, 2013.

[27] IAEA, "Assessing and Managing Cable Ageing in Nuclear Power Plants," International Atomic Energy Agency, Vienna International Centre, Vienna, Austria NP-T-3.6, May 2012.

[28] T. Seguchi, K. Tamura, T. Ohshima, A. Shimada, and H. Kudoh, "Degradation mechanisms of cable insulation materials during radiation–thermal ageing in radiation environment," *Radiation Physics and Chemistry*, vol. 80, pp. 268-273, 2011.

[29] IAEA, "Controlling of Degradation Effects in Radiation Processing of Polymers," International Atomic Energy Agency, Vienna, Austria IAEA-TECDOC-1617, May 2009.

[30] ASTM, "Standard Specification for Crosslinked Polyethylene (PEX) Tubing," ed. 100 Barr Harbor Drive, PO Box C700, West Conshohocken, PA 19428-2959: ASTM, 2015.

[31] (2017). *XLPE insulated power cable*. Available: http://www.leadercable.com.my/dl/leader-xlpe.pdf

[32] S. PÉLISSOU, J. CÔTÉ, S. ST-ANTOINE, and J. DALLAIRE, "Emergency Conditions Applied To Triplex Medium-Voltage XLPE Cables Having Flat Strap Neutrals," presented at the Jicable, Paris-Versailles, France, 2007.

[33] T. Seguchi, K. Tamura, A. Shimada, M. Sugimoto, and H. Kudoh, "Mechanism of antioxidant interaction on polymer oxidation by thermal and radiation ageing," *Radiation Physics and Chemistry,* vol. 81, pp. 1747-1751, 2012.

[34] A. Shimada, M. Sugimoto, H. Kudoh, K. Tamura, and T. Seguchi, "Degradation distribution in insulation materials of cables by accelerated thermal and radiation ageing," *IEEE Transactions on Dielectrics and Electrical Insulation*, vol. 20, pp. 2107-2116, 2013.

[35] K. J. Saunders, *Organic polymer chemistry: an introduction to the organic chemistry of adhesives, fibres, paints, plastics and rubbers*. London: Chapman and Hall, 1973.

[36] Xiameter. (2017). *Silicone Rubber Chemistry And Properties*. Available: https://www.xiameter.com/en/ExploreSilicones/ProductTypes/Silicone_Rubber/Pages/Rubber-Chemistry.aspx

[37] F. W. J. Billmeyer, *Textbook of polymer science*. New York: Wiley, 1984.

[38] AZOM. (2017). *Silicone Rubber*. Available: http://www.azom.com/article.aspx?ArticleID=920

[39] "Characteristic properties of silicone rubber compounds," Shin-Etsu-Silicone, 6-1, Ohtemachi 2-chome, Chiyoda-ku, Tokyo, 100-0004 Japan2017.

[40] "RTV Silicone Rubber for Electrical & Electronic Applications," Shin-Etsu-Silicone, 6-1, Ohtemachi 2-chome, Chiyoda-ku, Tokyo, 100-0004 Japan2017.

[41] X. Wang, S. Kumagai, and N. Yoshimura, "Contamination performances of silicone rubber insulator subjected to acid rain," *IEEE Transactions on dielectrics and Electrical Insulation,* vol. 5, pp. 909-916, 1998.

[42] P. C. PAINTER and M. M. COLEMAN, *Essentials of Polymer Science and Engineering*. 439 North Duke Street, Lancaster, Pennsylvania 17602 U.S.A.: DEStech Publications, Inc., 2009.

[43] J. Gulmine and L. Akcelrud, "FTIR characterization of aged XLPE," *Polymer Testing,* vol. 25, pp. 932-942, 2006.

[44] J. Lacoste, D. Carlsson, S. Falicki, and D. Wiles, "Polyethylene hydroperoxide decomposition products," *Polymer degradation and stability,* vol. 34, pp. 309-323, 1991.

[45] Y. J. Yu, F. W. Shen, H. McKellop, and R. Salovey, "Hydroperoxide formation in irradiated polyethylene," *Journal of Polymer Science Part A: Polymer Chemistry,* vol. 37, pp. 3309-3316, 1999.

[46] A. Gillis, B. Furman, and S. Li, "Variations in the determination of oxidation in UHM by 10 different FTIR protocols and a proposed standard protocol," in *Annual meeting-society for biomaterials in conjunction with the international biomaterials symposium*, 1998, pp. 28-28.

[47] M. Goldman, M. Lee, R. Gronsky, and L. Pruitt, "Oxidation of ultrahigh molecular weight polyethylene characterized by Fourier Transform Infrared Spectrometry," *Journal of biomedical materials research,* vol. 37, pp. 43-50, 1997.

[48] J. P. Collier, L. C. Sutula, B. H. Currier, J. H. Currier, R. E. Wooding, I. R. Williams, *et al.*, "Overview of Polyethylene as a Bearing Material Comparison of Sterilization Methods," *Clinical orthopaedics and related research,* vol. 333, pp. 76-86, 1996.

[49] L. C. Sutula, J. P. Collier, K. A. Saum, B. H. Currier, J. H. Currier, W. M. Sanford, *et al.*, "The Otto Aufranc Award: Impact of Gamma Sterilization on Clinical Performance of Polyethylene in the Hip," *Clinical orthopaedics and related research,* vol. 319, pp. 28-40, 1995.

[50] W. DiMaio, W. Lilly, W. Moore, and K. Saum, "Low wear, low oxidation radiation

crosslinked UHMWPE," in *TRANSACTIONS OF THE ANNUAL MEETING-ORTHOPAEDIC RESEARCH SOCIETY*, 1998, pp. 363-363.

[51] W. Sanford and K. Saum, "Accelerated oxidative aging testing of UHMWPE," *Trans Orthop Res Soc*, vol. 20, p. 119, 1995.

[52] H. McKellop, B. Yeom, D. Sun, and W. Sanford, "Accelerated aging of irradiated UHMW polyethylene for wear evaluations," in *TRANSACTIONS OF THE ANNUAL MEETING-ORTHOPAEDIC RESEARCH SOCIETY*, 1996, pp. 483-483.

[53] H. McKellop, F. Shen, T. Ota, B. Lu, H. Wiser, and E. Yu, "Wear of UHMWPE acetabular cups after gamma sterilization in nitrogen, thermal stabilization and artificial aging," *Trans Soc Biomaterials*, vol. 23, p. 45, 1997.

[54] S. M. Kurtz, O. K. Muratoglu, M. Evans, and A. A. Edidin, "Advances in the processing, sterilization, and crosslinking of ultra-high molecular weight polyethylene for total joint arthroplasty," *Biomaterials*, vol. 20, pp. 1659-1688, 1999.

[55] B. C. Smith, *Fundamentals of Fourier transform infrared spectroscopy*, 2 ed. 6000 Broken Sound Parkway NW, Suite 300, Boca Raton, FL 33487-2742: CRC Press, Taylor & Francis Group, 2011.

[56] A. Elzubair, J. C. M. Suarez, C. M. C. Bonelli, and E. B. Mano, "Gel fraction measurements in gamma-irradiated ultra high molecular weight polyethylene," *Polymer testing*, vol. 22, pp. 647-649, 2003.

[57] M. Sugimoto, A. Shimada, H. Kudoh, K. Tamura, and T. Seguchi, "Product analysis for polyethylene degradation by radiation and thermal ageing," *Radiation Physics and Chemistry*, vol. 82, pp. 69-73, 2013.

[58] A. Tidjani, "Comparison of formation of oxidation products during photo-oxidation of linear low density polyethylene under different natural and accelerated weathering conditions," *Polymer degradation and Stability*, vol. 68, pp. 465-469, 2000.

[59] I. Banik and A. K. Bhowmick, "Influence of electron beam irradiation on the mechanical properties and crosslinking of fluorocarbon elastomer," *Radiation Physics and Chemistry*, vol. 54, pp. 135-142, 1999.

[60] T. Seguchi, N. Hayakawa, K. Yoshida, N. Tamura, Y. Katsumura, and Y. Tabata, "Fast neutron irradiation effect—II. Crosslinking of polyethylene, ethylene-propylene copolymer, and tetrafluoroethylene-propylene copolymer," *Radiation Physics and Chemistry*, vol. 26, pp. 221-225, 1985.

[61] J. Luongo, "Infrared study of oxygenated groups formed in polyethylene during oxidation," *Journal of Polymer Science*, vol. 42, pp. 139-150, 1960.

[62] V. Krishnakumar and R. Mathammal, "Density functional theory calculations and vibrational spectra of 3, 5 dichloro hydroxy benzaldehyde and 2, 4 dichloro benzaldehyde," *Journal of Raman Spectroscopy*, vol. 39, pp. 1890-1899, 2008.

[63] T. Seguchi, K. Tamura, H. Kudoh, A. Shimada, and M. Sugimoto, "Degradation of cable insulation material by accelerated thermal radiation combined ageing," *IEEE Transactions on Dielectrics and Electrical Insulation,* vol. 22, pp. 3197-3206, 2015.

[64] S. Baccaro, U. Buontempo, and P. D'atanasio, "Radiation induced degradation of EPR by IR oxidation profiling," *Radiation Physics and Chemistry,* vol. 42, pp. 211-214, 1993.

[65] S. Baccaro and U. Buontempo, "Radiation induced oxidative degradation of ethylene-propylene rubber by IR spectroscopy," *International Journal of Radiation Applications and Instrumentation. Part C. Radiation Physics and Chemistry,* vol. 40, pp. 175-180, 1992.

[66] K. Anandakumaran and D. Stonkus, "Assessment of oxidative thermal degradation of crosslinked polyethylene and ethylene propylene rubber cable insulation," *Polymer Engineering & Science,* vol. 32, pp. 1386-1393, 1992.

[67] K. Anandakumaran, W. Seidl, and P. Castaldo, "Condition assessment of cable insulation systems in operating nuclear power plants," *IEEE transactions on dielectrics and electrical insulation,* vol. 6, pp. 376-384, 1999.

[68] D. J. Hill, C. M. Preston, and A. K. Whittaker, "NMR study of the gamma radiolysis of poly (dimethyl siloxane) under vacuum at 303K," *Polymer,* vol. 43, pp. 1051-1059, 2002.

[69] H. Menhofer, J. Zluticky, and H. Heusinger, "The influence of irradiation temperature and oxygen on crosslink formation and segment mobility in gamma-irradiated polydimethylsiloxanes," *International Journal of Radiation Applications and Instrumentation. Part C. Radiation Physics and Chemistry,* vol. 33, pp. 561-566, 1989.

[70] A. Miller, "Radiation chemistry of polydimethylsiloxane. 1 I. Crosslinking and gas yields," *Journal of the American Chemical Society,* vol. 82, pp. 3519-3523, 1960.

[71] A. Shimada, M. Sugimoto, H. Kudoh, K. Tamura, and T. Seguchi, "Degradation mechanisms of silicone rubber (SiR) by accelerated ageing for cables of nuclear power plant," *IEEE Transactions on Dielectrics and Electrical Insulation,* vol. 21, pp. 16-23, 2014.

[72] H. S. Fogler, *Elements of Chemical Reaction Engineering*, 3 ed. Upper Saddle River, NJ: Prentice-Hall, 1999.

[73] O. Levenspiel, *Chemical Reaction Engineering*, 3 ed. New York, NY: John Wiley & Sons, 1999.

[74] D. A. Porter and K. E. Easterling, *Phase Transformations in Metals and Alloys*, 2 ed. Cheltenham, United Kingdom: Nelson Thornes Ltd, 2001.

[75] S. Kurtz, O. Muratoglu, L. Mounib, B. Currier, R. Gsell, B. Hastings, *et al.*,

"Interlaboratory validation of a standard for determining the oxidation index of UHMWPE," in *Proceedings of the 45th Annual Meeting of Orthopaedic Research Society*, 1999.

[76] M. Villaran and R. Lofaro, "Condition Monitoring of Cables Task 3 Report: Condition Monitoring Techniques for Electric Cables," Nuclear Energy and Infrastructure Division, Energy Sciences and Technology Department, Brookhaven National Laboratory, Washington, D.C. BNL-90735-2009-IR, November 2009.

[77] Y. Mecheri, L. Boukezzi, A. Boubakeur, and M. Lallouani, "Dielectric and mechanical behavior of cross-linked polyethylene under thermal aging," in *Electrical Insulation and Dielectric Phenomena, 2000 Annual Report Conference on*, 2000, pp. 560-563.

[78] Y. Mecheri, M. Nedjar, A. Lamure, M. Aufray, and C. Drouet, "Influence of moisture on the electrical properties of XLPE insulation," presented at the Conference on Electrical Insulation and Dielectric Phenomena (CEIDP), Purdue University, West Lafayette, IN, 2010.

[79] A. Motori, F. Sandrolini, and G. Montanari, "Degradation and electrical behavior of aged XLPE cable models," in *Conduction and Breakdown in Solid Dielectrics, 1989., Proceedings of the 3rd International Conference on*, 1989, pp. 352-358.

[80] K. T. Gillen and R. L. Clough, "Time-temperature-dose rate superposition: a methodology for extrapolating accelerated radiation aging data to low dose rate conditions," *Polymer Degradation and Stability*, vol. 24, pp. 137-168, 1989.

[81] S. Burnay, "A practical model for prediction of the lifetime of elastomeric seals in nuclear environments," presented at the ACS Symposium, Washington DC, 1991.

[82] IAEA, "Assessment and management of ageing of major nuclear power plant components important to safety: In-containment instrumentation and control cables Volume II," International Atomic Energy Agency, Vienna, Austria IAEA-TECDOC-1188, December 2000.

[83] K. T. Gillen and R. Bernstein, "Review of nuclear power plant safety cable aging studies with recommendations for improved approaches and for future work," Sandia National Laboratories, Albuquerque, New Mexico SAND 2010-7266, 2010.

[84] R. W. Balluffi, S. Allen, and W. C. Carter, *Kinetics of materials*. New Jersey: John Wiley & Sons, Inc, 2005.

[85] K. A. Jackson, *Kinetic Processes Crystal Growth, Diffusion, and Phase Transitions in Materials*. Weinheim, Germany: 2004 WILEY-VCH Verlag GmbH & Co. KGaA, 2004.

[86] W. Navidi, *Statistics for Engineers and Scientists*, 3 ed. New York: McGraw-Hill, 2009.

[87] S. M. Sze and M. K. Lee, *Semiconductor Devices Physics and Technology*, 3 ed. New York, NY: John Wiley & Sons, Inc., 2012.

[88] J. S. Blakemore, *Solid State Physics*, 2 ed. Cambridge, UK: Cambridge University Press, 1985.

[89] P. Debye, "Zur Theorie der spezifischen Wärmen," *Annalen der Physik*, vol. 344, pp. 789-839, 1912.

[90] A. Einstein, "Die Plancksche Theorie der Strahlung und die Theorie der spezifischen Wärme," *Annalen der Physik*, vol. 327, pp. 180-190, 1907.

[91] K.-N. Tu, *Electronic thin-film reliability*: Cambridge University Press, 2011.

[92] Y.-S. Chang and A. Mosleh, "Predictive model of the degradation of cable insulation subject to radiation and temperature," presented at the International topical meeting on probabilistic safety assessment and analysis (PSA), Pittsburgh, PA, 2017.

[93] Y.-S. Chang and A. Mosleh, "Physics-Based Model of the Degradation of Cable Insulation Subject to Radiation and Heat," presented at the IEEE Conference on Electrical Insulation and Dielectric Phenomenon, Fort Worth, TX, 2017.

[94] Y.-S. Chang and A. Mosleh, "Probabilistic Degradation Models for Cable Insulation in Nuclear Power Plants," presented at the ANS Winter Meeting and Nuclear Technology Expo, Washington, D.C., 2017.

[95] D. L. Smith, *Thin-film deposition: principles and practice*. New York, NY: McGraw-Hill, Inc, 1995.

[96] T. Šarac, N. Quiévy, A. Gusarov, and M. Konstantinović, "The study of temperature and radiation induced degradation of cable polymers: A comparison between the mechanical properties of industrial and neat EPDM," *Procedia Structural Integrity*, vol. 2, pp. 2405-2414, 2016.

[97] K. Makuuchi and S. Cheng, *Radiation Processing of Polymer Materials and Its Industrial Applications*, 1 ed. Hoboken, New Jersey: John Wiley & Sons, Inc., 2012.

[98] L. Darken, "Diffusion of carbon in austenite with a discontinuity in composition," presented at the Trans. Aime, Philadelphia, 1948.

[99] K. Tu, Y. Liu, and M. Li, "Effect of Joule heating and current crowding on electromigration in mobile technology," *Applied Physics Reviews*, vol. 4, p. 011101, 2017.

[100] D. R. Gaskell, *Introduction to the Thermodynamics of Materials*, 3 ed. Washington, D.C.: Taylor & Francis, 1995.

[101] N. F. Britton, *Reaction-diffusion equations and their applications to biology*. Orlando, FL: Academic Press, 1986.

[102] Chemicalbook. (2017). *4,4'-Thiobis(6-tert-butyl-m-cresol)*. Available: http://www.chemicalbook.com/ChemicalProductProperty_EN_CB0722795.htm

[103] NOAA. (2017). *4,4'-THIOBIS(6-TERT-BUTYL-M-CRESOL)*. Available: https://cameochemicals.noaa.gov/chemical/21102

[104] C. Walck, *Hand-Book on Statistical Distributions for Experimentalists*, 3 ed. Stockholm, Sweden: University of Stockholm, 2007.